DESIGN CONSIDERATIONS FOR MONOPILE FOUNDED OFFSHORE WIND TURBINES SUBJECT TO BREAKING WAVES

A Thesis

by

GARRETT REESE OWENS

Submitted to the Office of Graduate Studies of
Texas A&M University
in partial fulfillment of the requirements for the degree of

MASTER OF SCIENCE

Approved by:

Chair of Committee,	John Niedzwecki
Committee Members,	Charles Aubeny
	Joseph Newton
Head of Department,	John Niedzwecki

December 2012

Major Subject: Civil Engineering

ABSTRACT

The majority of offshore wind farms utilize monopile substructures. As these wind farms are typically located in water depths less than 30 meters, the effect of breaking waves on these structures is of great concern to design engineers. This research investigation examines many of the practical considerations and alternative ways of estimating breaking wave forces. A survey of existing European wind farms is used to establish a realistic range of basic design parameters. Based upon this information a parametric study was pursued and a series of realistic design scenarios were evaluated. Comparisons include the sensitivity to the wave force model as well as to analytical and numerical wave theories used to evaluate the wave kinematics. In addition, the effect of different kinematics stretching techniques for linear waves is addressed. Establishing whether the bathymetry will induce spilling or plunging wave breaking is critical. Spilling wave breaking can be addressed using existing wave and wave force theories, however for plunging wave breaking an additional impact force must be introduced. Dimensionless design curves are used to display pertinent trends across the full range of design cases considered. This research study provides insight into the evaluation of the maximum breaking wave forces and overturning moment for both spilling and plunging breaking waves as a function of bottom slope.

ACKNOWLEDGEMENTS

This research study was supported in part by a grant from the Norwegian Center for International Cooperation in Higher Education and the Wofford Cain ’13 Senior Chair in Offshore Technology. The Harold J. “Bill” Haynes ‘46 Fellowship provided additional funding during my graduate studies. This generous financial support made my graduate education possible and for this support I am very grateful.

The financial support of the Norwegian grant to Dr. Ove Gudmestad and Dr. John Niedzwecki allowed me to spend a semester abroad at the University of Stavanger. I especially want to thank Dr. Gudmestad for both his hospitality during my stay in Norway and for his technical insight on a topic that would eventually become my thesis. I would also like to thank my adviser, Dr. Niedzwecki. His guidance throughout my graduate education has been invaluable.

To all my officemates, thanks for the coffee and shared meals. To my parents, thanks for helping and loving me every step along the way. And to Nana, thanks for heading up the editorial board.

NOMENCLATURE

α	Bottom Slope Angle
γ	Angle Relating Cylinder and Wave Crest Orientation
θ	Wave Phase Angle
κ	Breaking Index
λ	Curling Factor
ξ_o	Deep Water Version of Surf Similarity Parameter
ξ_b	Breaking Version of Surf Similarity Parameter
η	Free Surface Wave Elevation
η_B	Free Surface Elevation of the Wave Crest
η_c	Max Elevation of Wave Crest
η_t	Min Elevation of Wave Trough
σ	Wave Frequency
ρ	Density of Water
ϕ	Velocity Potential
ψ	Stream Function
A	Wave Amplitude
C	Wave Celerity
C_D	Drag Coefficient

C_M	Inertia Coefficient
C_s	Slamming Coefficient
Cha	Chakrabarti Stretching
D	Cylinder Diameter
DSF	Dean's Stream Function
F	Total Force for Given Time
F_D'	Total DSF Drag Force For Given Time
F_{HT}	FNV Harmonic Total Force
F_{H1}	FNV First Harmonic Force
F_{H2}	FNV Second Harmonic Force
F_{H3}	FNV Third Harmonic Force
$F_I(t)$	Impact Force For Given Time
GW	Gigawatt
H	Wave Height
H_b	Breaking Wave Height
H_o	Deep Water Wave Height
L	Wavelength
L_o	Deep Water Wavelength
LWT	Linear Wave Theory

M	Total Moment for a Given Time
M_{HT}	FNV Harmonic Total Moment
M_{H1}	FNV First Harmonic Moment
M_{H2}	FNV Second Harmonic Moment
M_{H3}	FNV Third Harmonic Moment
M_{H4}	FNV Fourth Harmonic Moment
MW	Megawatt
MWL	Mean Water Level
RNA	Rotor Nacelle Assembly
S	Bottom Slope
T	Wave Period
V	Wave Crest Impact Velocity
Whe	Wheeler Stretching
a	Cylinder Diameter
$a(S)$	Weggel Factor (Functions of Slope)
$b(S)$	Weggel Factor (Functions of Slope)
d	Water Depth
d_b	Breaking Water Depth
f_D	Drag Force from Morison Equation for given Location and Time
f_I	2D Distributed Impact Force

f_M	Inertia Force from Morison Equation for given Location and Time
f_T	Total Force from Morison Equation for given Location and Time
g	Acceleration Due to Gravity
k	Wave Number
km	Kilometers
m	Meters
s	Vertical Cartesian Coordinate From Seafloor
t	Time
u	Horizontal Wave Particle Velocity
u'	Horizontal Wave Particle Velocity for DSF
$\dot{u}$	Horizontal Wave Particle Acceleration
x	Horizontal Cartesian Coordinate
z	Vertical Cartesian Coordinate From MWL

TABLE OF CONTENTS

LIST OF FIGURES

LIST OF TABLES

1. INTRODUCTION

The offshore wind industry has experienced substantial growth and is expected to continue to grow in the future. The industry is largely based in Europe, where it began over twenty years ago, but developers and governments around the world are looking to tap this plentiful energy source. As of 2011, European countries had 3,300 MW of offshore wind capacity operational, with an additional 5,600 MW under construction, and over 17,000 MW or 17 GW consented to be built (EWEA, 2011). This represents approximately 26 GW of the 40 GW goal established by the European Wind Energy Association for offshore wind capacity in the EU by 2020. Looking to Asia, demonstration and near shore intertidal projects in China have established the country as a serious future player with a goal of 30 GW by 2020.

The development of the offshore wind industry is slower to start in countries like the United States, which has no installed offshore wind farms or demonstration projects as of August 2012. From the Gulf of Mexico to the Great Lakes, there are a number of projects in various stages of planning. The project closest to construction is a 468 MW wind farm known as Cape Wind. Located in the Nantucket Sound off the coast of Massachusetts it is expected to begin construction in 2013.

1.1 Industry Trends

As the offshore wind industry continues to grow and expand into new markets around the world, innovation and advancements in offshore wind specific technologies

will play a larger role in the development of the industry. This advancement in the state of the art results in large part from land based and near shore experiences. The offshore wind turbine design paradigm has been shaped in a couple of ways. First, it has resulted in the development of much larger wind turbines with greater generating capacities. Second, it has resulted in wind turbines being placed in deeper water farther from shore.

Both of these trends are a product of attempting to maximize the power generation from each wind turbine installation. Placing turbines in offshore sites with higher average wind speeds is the primary way of achieving this. Offshore wind farms built in the UK in 2011 had an annual average wind speed of 9.5 m/s, up from an annual average wind speed of 7 to 8 m/s in 2007 and 2008 (Offshore Wind Cost Reduction: Pathways Study, 2012). Larger turbines with faster rotor tip speeds more efficiently capture the energy at these higher wind velocities. The size and noise limitations that typically constrain onshore wind turbines are relaxed for offshore installations. Furthermore, as near shore sites with the best wind speeds are developed, offshore wind farms must be placed in locations farther from land and in deeper water in order to maintain optimal wind conditions.

Investigating the first design trend of larger wind turbines is essential for future discussions. The European Wind Energy Association reports that the generating capacity of turbines installed in Europe in 2011 averaged 3.6 MW, up from an average of 3 MW for turbines installed in 2010 (2012). This increase in size and capacity is also expected to continue into the future. The average turbine capacity of European projects under construction will rise to 3.9 MW, increasing as a result of new 5-6 MW turbine models

(EWEA, 2012). This size aspect translates into heavier nacelles, taller hub heights, and rotors that sweep larger areas. Refer to Table 1 for a general overview of turbine weight and rotor diameters of commonly used offshore wind turbines. Notice the general positive trend of every category with increasing capacity, particularly when comparing the 2 and 3 MW turbines with the 5 and 6 MW examples. One caveat to this observation, a decrease in the total weight of the turbine is evident in the transition from the 2 MW machines to the 3 MW examples. This decrease is because these particular 3 MW examples use direct drive, eliminating the need for a gearbox. So, while technological advances can decrease weight, it holds that larger turbines have larger sweep areas and heavier total weights.

Table 1 Weight of Components in Commonly Used Offshore Wind Turbines

Turbine	Capacity (MW)	Diameter (m)	Rotor (ton)	Nacelle (ton)	Total (ton)
Siemens 2.3-93	2.3	93	60	82	142
Nordex N90	2.5	90	55	91	146
Vestas V90-3	3	90	42	70	112
Siemens 3.0-101	3	101	40	73	113
Siemens 3.6-107	3.6	107	95	125	220
Repower 5 M	5	126	120	300	420
Multibrid M5000	5	116	110	199	309
Repower 6M	6	126	135	325	460

Table Source (Kaiser and Snyder, 2012)

Expanding the discussion of the design trend of wind turbines being placed in deeper water farther from land is also important. Again focusing on Europe, in 2011 the average depth for installed offshore wind farms was 22.8 meters, with an average

distance to shore of 23.4 km (EWEA, 2012). Taking a look at projects under construction in Europe the average depth increases to 25.3 m and the average distance to shore also increases to 33.2 km (EWEA, 2012). This depth and distance trend is apparent in Figure 1, which is taken from a European Wind Energy Association report (2011). The size and placement of the dots corresponding to European projects under construction as well as to consented projects clearly conveys that this increasing depth and distance trend is well established for traditional substructure choices. The increase in depth translates into larger or more complicated substructures while the increase in distance could possibly expose the installations to more extreme marine environments.

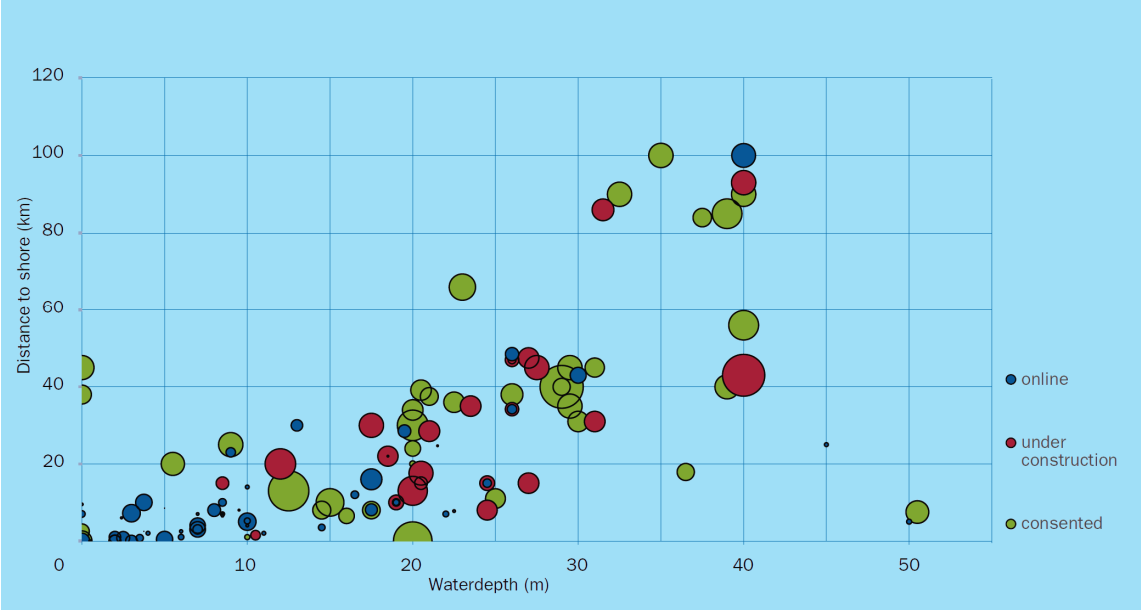

Figure 1 Average Size, Distance, and Water Depth of European Wind Farms

Implied in this discussion of industry trends are the technological factors of substructure and foundation design that control elements of the trend's progress.

Offshore wind turbine siting is characterized using water depth and falls into three main categories; shallow water (0-30m), transitional water (30-60m) and deep water (>60m). Each category has specific substructure and foundation options that are optimal for the given water depth ranges. Common shallow water substructure options are monopiles and gravity base structures. Transitional water options include jackets, tripods, and tripiles. This particular discussion excludes deep water floating options and focuses entirely on grounded shallow and transitional options.

As the industry continues to push the limits of size and location, it is increasingly important to determine the magnitude and location of environmental loading on the substructures. Larger turbines have greater wind loads; similarly, larger substructures have greater wave loads. Taller hub heights and deeper water means the foundation must transmit larger bending moments to the soil. To advance the state of the art of offshore wind turbines the design must account for greater loads on a structure of ever increasing size.

To provide some context of just how far the state of the art has progressed in the relatively short history of the industry, two offshore wind farms are juxtaposed. The first offshore wind farm in the world, Vindeby, was commissioned in Denmark in 1991. Employing gravity base foundations, this shallow water wind farm is located 1.5 to 3 kilometers from shore and in water depths ranging from 2 to 4 meters (Burton, 2011). Each wind turbine is rated at 0.45 MW; with 11 turbines in total, the wind farm has a combined capacity of 5 MW. Twenty years later BARD Offshore 1 is coming online in the German controlled region of the North Sea. It will be fully commissioned in 2013.

Dwarfing earlier turbines in size and capacity, each BARD wind turbine is rated at 5 MW; 80 turbines result in a wind farm with a capacity of 400 MW. Using a tripile foundation design in water depths ranging from 39 to 41 meters, this transitional water wind farm is located 100 kilometers from shore (Burton, 2011). The contrast of these two projects demonstrates the advancement of size and location. Thus, the trend in the industry is to build larger turbines for larger wind farms located farther offshore in deeper water.

1.2 Design Paradigm

While the two previous examples of wind farm foundation types are different as a result of being in different water depth categories, the dominant substructure choice in the industry is a monopile. Refer to Figure 2 for an overview of offshore wind turbine terminology as it pertains to monopile substructures (Tempel, 2006). The term "monopile substructure" is defined as consisting of both the transition piece and foundation monopile. Together the substructure and tower make up the entire support structure. The rotor nacelle assembly (RNA) sits atop the support structure. Approximately 80 percent of all offshore wind turbine installations employ a monopile design according to the National Research Council (2011). As wind farms are placed in deeper water, jackets and tripods are expected to increase in frequency. However, monopiles are still projected to be 50-60% of installed substructures between 2011 and 2020 (Kaiser and Snyder, 2012). Therefore, the focus of the remaining discussion and analysis will be entirely on monopile substructures.

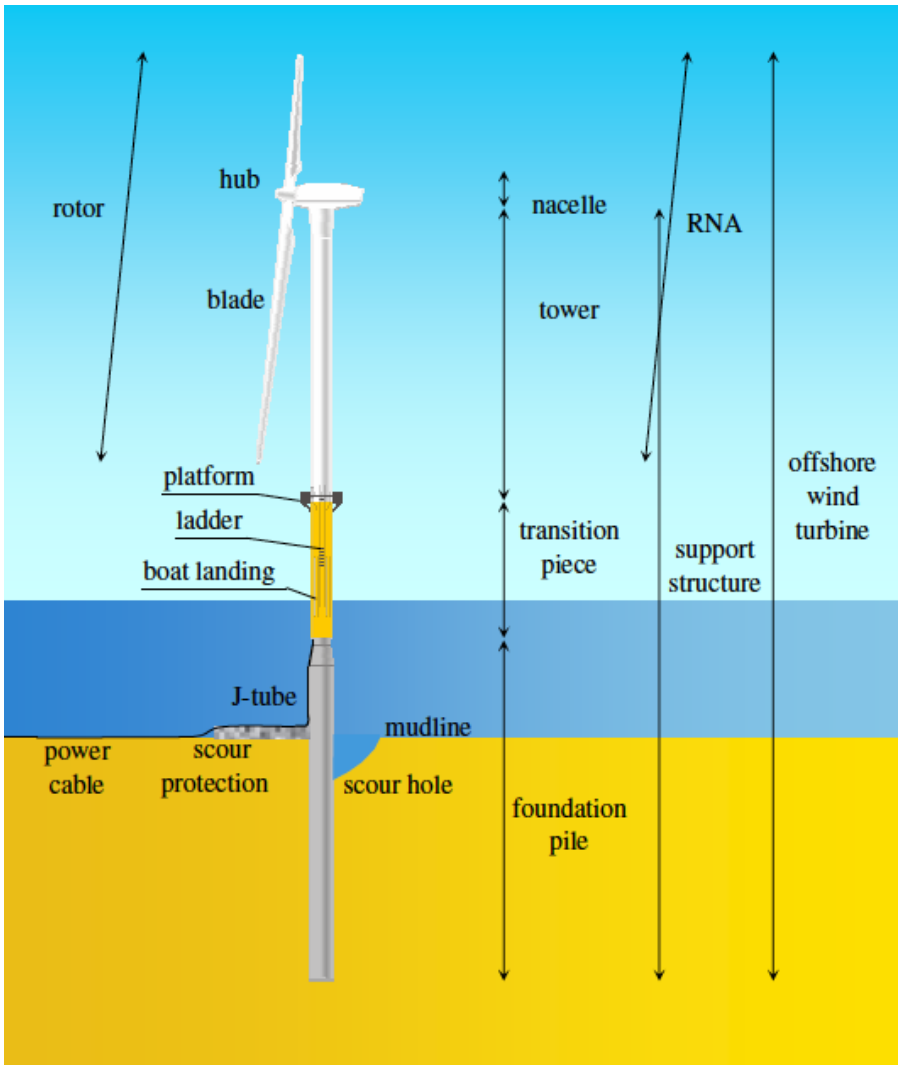

Figure 2 Overview of Offshore Wind Turbine Terminology (Tempel, 2006)

Given the major role the monopile substructure currently plays in the industry, and is expected to play in the future, a more detailed discussion of its components is merited. The monopile consists of a large steel cylinder 4 to 8 meters in diameter with wall thicknesses up to 8 centimeters. The foundation monopile is typically driven into the seafloor and extends from its embedment depth to just above the sea surface. Attached to the top of this large foundation pile is a transition piece, which has a typical

length over 1.5 times the outside diameter of the pile. The transition piece is grouted into place and ensures vertical tolerances are maintained for proper turbine alignment. These two structural elements provide an attachment point for the base of the tower. Refer to Table 2 for a comparison of typical monopile and transition piece properties (LORC, 2012). Unfortunately, due to the nature of statistics reporting by developers the data set is not entirely complete. Regardless, a general sense of the weights, lengths, outside diameters, and embedment depths can be gained from the available data.

Table 2 Typical Monopile and Transition Piece Properties

Wind Farm	Water Depth (m)	Monopile				Transition Piece		
		Length (m)	Weight (ton)	Embed Depth (m)	OD (m)	Length (m)	Weight (ton)	OD (m)
Gunfleet Sands, UK	0-15	50	225-423	27-38	-	23	230	-
London Array 1, UK	0-25	85	650	-	-	30	350	5
Burbo Bank 1, UK	2.0-8.0	52	400	25	5	-	-	-
Rhyl Flats, UK	6.5-12.5	40	193-235	-	-	-	220	5
Baltic 1, DE	16-19	37	215	20	4.3	27	250	4.2-4.6
Sheringham Shoal, UK	17-22	44-61	375-530	23-37	4.2-5.2	22	200	-
Belwind, BE	20-37	50-72	300-550	35	-	25	120	4.3
Greater Gabbard, UK	24-34	60	700	30	-	-	-	-

There are several factors that limit the deployable depth of a monopile substructure to roughly 30 meters. At this depth there are cost and constructability

considerations that make transitional substructures not only more feasible but more economical than the monopile. First, there are material restrictions to the size of steel plates used in construction, thereby limiting the diameter and thickness of piles that can be assembled. This restriction to the cross section limits the maximum moment capacity of the structure and by extension limits the water depth. As water depth increases, moment arms for the wind and wave loads also increase. At a certain depth the moment capacity of the cross section will be reached.

Another restriction, which is often the limiting case, is based in structural dynamics. The bending stiffness of the cross section and the overall length of the support structure are important parameters that affect the dynamic characteristics of the offshore wind turbine. Holding pile diameter constant, the natural frequency of the support structure decreases with increasing water depth (Musial et al., 2010). At different points the natural frequency will resonate with both the frequency of the turning turbine rotors and the frequencies of dynamic excitations resulting from the combined wind and wave loads. Resonance can pose serious issues for the fatigue life of the structure and needs to be considered. Consequently, the structure must be designed to have a certain natural frequency in order to limit the dynamic response. This particular natural frequency is achieved by changing the bending stiffness of the cross section or limiting the length of the support structure. Implied in this discussion are the material restrictions previously mentioned. Considering cost and constructability, a cross section with optimal bending stiffness is chosen. It follows that limiting the length of the support structure is the only

option left to achieve the target natural frequency. Structural dynamic considerations therefore limit the practical deployable depth of monopile substructures.

As the design paradigm is pushed to the limits of deployable depth for monopiles the effect waves have on the entire structure becomes more pronounced. In shallower water the moment arm of the wave load is relatively short compared to the moment arm of the wind load. But, as water depth increases the wave loading begins to dominate. De Vries and Krolis (2007) demonstrated this for the Vestas V90 3MW wind turbine with adequately sized monopile support structures in water depths ranging from 20 to 50 meters. Figure 3 shows the resulting overturning moment as a function of water depth. For a complete discussion of their approach refer to the reference. The range of water depths in this particular example extends beyond the typical range that is common for monopile substructures. For this design load case, even in the range from 20 to 30 meters, hydrodynamic loads dominate the overturning moment.

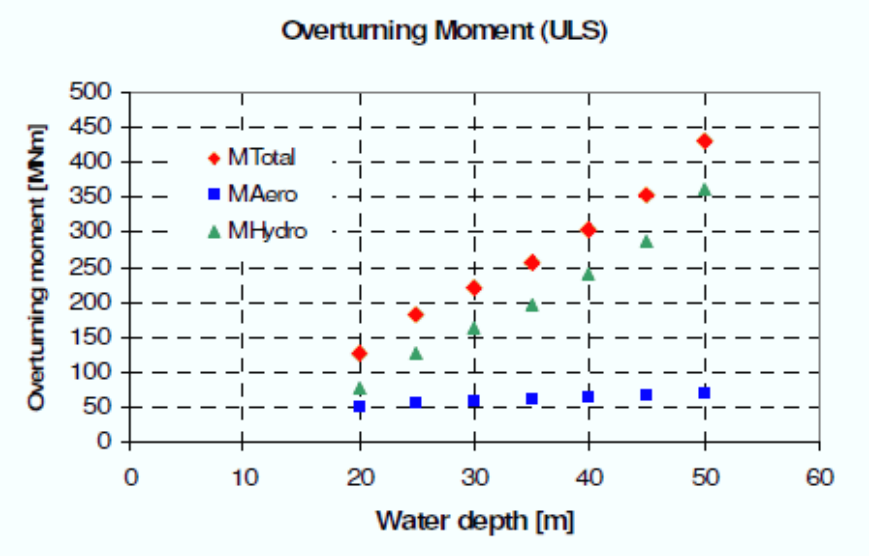

Figure 3 Overturning Moment as a Function of Water Depth (De Vries and Krolis, 2007)

1.3 Research Direction

Given the importance of hydrodynamic loads on monopile substructures of increasing diameters and increasing water depths, an accurate method of determining this loading is critical. For monopiles, hydrodynamic loads result from currents and waves passing by the stationary support structure. Current loads will not be considered for this analysis. In order to narrow the discussion, the term hydrodynamic load will only refer to loads that result from passing waves. Focusing on waves, there are several key characteristics of design waves that require mentioning. Establishing the height of the design wave, the water depth over which it acts, the maximum crest elevation, and the period of the wave (by extension the wave length) gives a complete picture of the design wave. However, large design waves are inherently nonlinear. Nonlinear waves have higher and steeper crests with shallower and longer troughs. The prospect of accurately determining the kinematics up to the wave crest, and ultimately the wave loads, becomes more complicated.

Determining the kinematics of the wave up to the crest is the first step in calculating hydrodynamic loads. The kinematics of waves are determined using wave theories. Two subtypes of wave theories are analytical and numerical. An example of an analytical theory is linear wave theory. An example of a numerical theory is stream function wave theory. These two wave theories will receive more detailed explanations in a later section. For hydrodynamic load calculations the required outputs from these theories are the horizontal particle velocity and acceleration. The next step is applying these two kinematic quantities and other design wave properties to a wave force theory.

There are two different wave force theories that will be investigated. First, the traditional approach was published by Morison et al. (1950). The resulting Morison equation accounts for drag and inertial components of the force, relating to the horizontal velocity squared and horizontal acceleration of the water particles respectively. This approach uses the kinematics calculated from the wave theories previously discussed. Another approach for calculating wave loads on a slender vertical cylinder was developed by Faltinsen et al. (1995). Known as FNV theory, it is set up as a diffraction analysis problem but it uses additional second and third order harmonics to model the force. Instead of using the horizontal kinematics as was the case with the Morison equation, FNV theory uses certain properties of the design wave to model the force.

There are important restrictions to the applications of these wave theories. There are ranges of wave length to cylinder diameter ratios that limit each wave force theory. Given the typical outside diameter of monopiles and the extreme nature of the waves these restrictions are not expected to be an issue. One other important restriction for the use of the wave force theories is that the monopile substructure be considered a completely rigid structure.

The process of calculating wave forces, which is relatively straightforward for rigid structures and smaller design waves, becomes more complicated for extreme breaking waves. The phenomenon of wave breaking occurs when waves reach a limiting wave height. This limiting wave height is a function of water depth and wavelength. There are three types of breaking wave forms: spilling breakers, plunging breakers, and

surging breakers. Spilling breakers occur when water at the crest cascades down the face of the wave. Plunging breakers result when the wave crest overturns and dives into the trough. Surging breakers occur when the wave appears to be undercut by the wash from the previous wave. Figure 4 provides an illustration of the three breaking wave forms and relates them to typical bottom slopes. In shallow water sites waves break with more frequency due to the influence of the bottom and its slope.

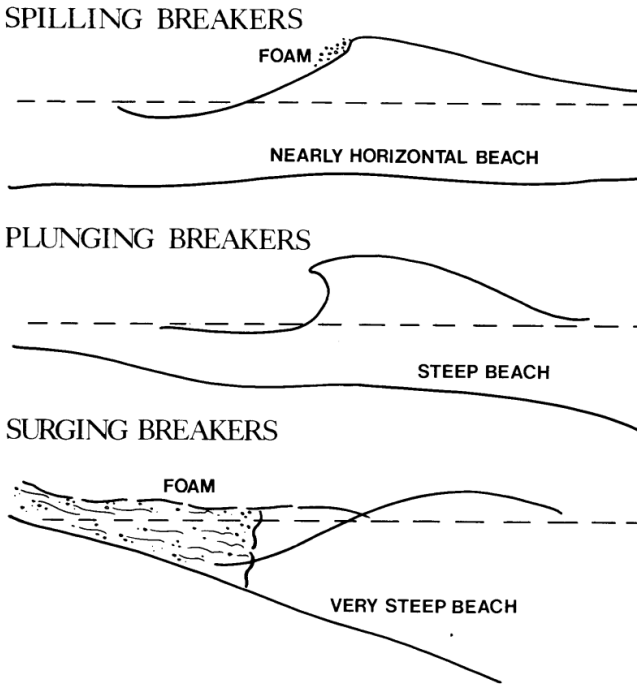

Figure 4 Types of Breaking Waves
Figure source (http://www.oas.org/pgdm/hazmap/cstlersn/stk_nev/kn_rept.htm)

Waves that break onto a monopile can impart a different type of load in addition to the typical hydrodynamic loads previously discussed. This additional load is an impact load and results from the crest of the wave colliding with the stationary

substructure. The impact load from breaking waves is very different from traditional hydrodynamic loads which act from the water surface to seafloor. In comparison, impact loads are concentrated around crest level and are more of an impulsive force in that they act over a shorter period of time. Determining the location and size of this impact load is very important for the design of offshore wind turbine substructures. In terms of types of breaking waves, plunging breakers are of the greatest concern when considering maximum potential for impact loads (Wienke and Oumeraci, 2005). In shallow water sites the load combination of extreme breaking waves can become a design driver for monopile substructures and must be considered (Musial et al., 2010).

Some pertinent trends in the industry have been established and present an interesting design problem. As offshore wind specific turbine technology continues to be developed, the size of the turbines will continue to grow. Larger turbines translate into larger wind loads. The increase in generating capacity is also met with a general increase in the weights of the RNA and tower as well as an increase in hub heights. Additionally, wind farms are being installed farther offshore in greater water depths. All these factors result in larger bending moments being transmitted to the foundation. The monopile substructure, which is expected to continue to be the dominant substructure choice of the industry, needs to be able to account for these ever increasing loads.

Considering these trends, the design paradigm of monopile substructures is constantly advancing. For the design of offshore wind turbines the importance of accurately determining hydrodynamic loads is clear. Waves are much more likely to reach the criteria for breaking in extreme sea states required for ultimate design

scenarios. The hydrodynamic loads of spilling breaking waves are significant in their own right. The extra loading that can result from the impact force of a plunging breaking wave presents another critically important source of loading. The following analysis and discussion will investigate the different methods available for determining wave loads over a range of water depths and breaking wave conditions. A comparison of the kinematics, forces, and resulting moments will highlight similarities and differences between the methods available for the design of breaking waves.

2. THEORY AND ENGINEERING DESIGN

This section aims to more fully develop the theory and resulting engineering design process behind wave load calculations previously introduced. The discussion centers on the hydrodynamic and impact loads that result from breaking waves. The underlying theories of several different methods available are presented and contrasted. An understanding of the limitations and restrictions of determining both wave kinematics and design wave parameters plays an important role in accurate force calculations. This serves as a basis for a discussion about the applicability of each method in the context of designing for breaking wave loads. The engineering design cited here is not the structural design of the monopile substructures in the strictest sense but rather the global loading. It is also not a discussion of choosing appropriate design wave heights and metocean conditions that relate to a particular site. Rather, the focus is on characterizing the nature of breaking wave loads and the methods available for designers to calculate this particular environmental phenomenon.

2.1 Linear Wave Theory Kinematics and Forces

The most basic method for estimating the wave kinematics of ocean waves is an analytical approach known as Airy wave theory, or linear wave theory (LWT). See for example Dean and Dalrymple (1991). For this approach the solution of the Laplace equation is expressed as a function of a velocity potential ϕ. The fluid is assumed to be incompressible and the flow is assumed to have irrotational motion. Linear wave theory

is a first order solution of the more general Stokes wave theory. Thus, the solution is constrained to waves with comparatively small heights relative to their lengths and water depths. Furthermore, the equations for wave kinematics are valid only up to the mean water level (MWL). This has lead engineers to develop stretching techniques to estimate wave crest kinematics required for design load calculations.

The horizontal velocity and the horizontal acceleration are required for force calculations using Morison equation in this study. The horizontal velocity and horizontal acceleration are written respectively as

$$u = \frac{gHk}{2\sigma}\frac{\cosh k(d+z)}{\cosh kd}\cos(\theta) \tag{2.1}$$

$$\dot{u} = \frac{\partial u}{\partial t} = \frac{gHk}{2}\frac{\cosh k(d+z)}{\cosh kd}\sin(\theta) \tag{2.2}$$

where g is acceleration due to gravity, H is the wave height, k is the wave number, σ is the wave frequency, d is the water depth, z is the vertical Cartesian coordinate and height above MWL, and θ is the wave phase angle. Respectively, the wave phase angle, wave number, and wave frequency are defined as

$$\theta = kx - \sigma t \tag{2.3}$$

$$k = \frac{2\pi}{L} \tag{2.4}$$

$$\sigma = \frac{2\pi}{T} \tag{2.5}$$

where t is time in seconds, L is the wave length, T is the wave period, and x is the Cartesian coordinate that refers to the position along the horizontal axis. The surface of the wave varies with time and position accordingly,

$$\eta = \frac{H}{2}\cos(kx - \sigma t) \tag{2.6}$$

where η refers to the free surface elevation of the wave. There is another variable that is used for the vertical axis and is zero at the seafloor. Relating the two variables for the vertical axis is necessary,

$$z = s - d \tag{2.7}$$

where s is the height above the seafloor. Figure 5 provides an illustration relating these wave dimension variables. For the design wave approach the wave height, wave period, and water depth are specified. The wave length for LWT is evaluated using the dispersion equation, expressed here as

$$\sigma^2 = gk \tanh kd \tag{2.8}$$

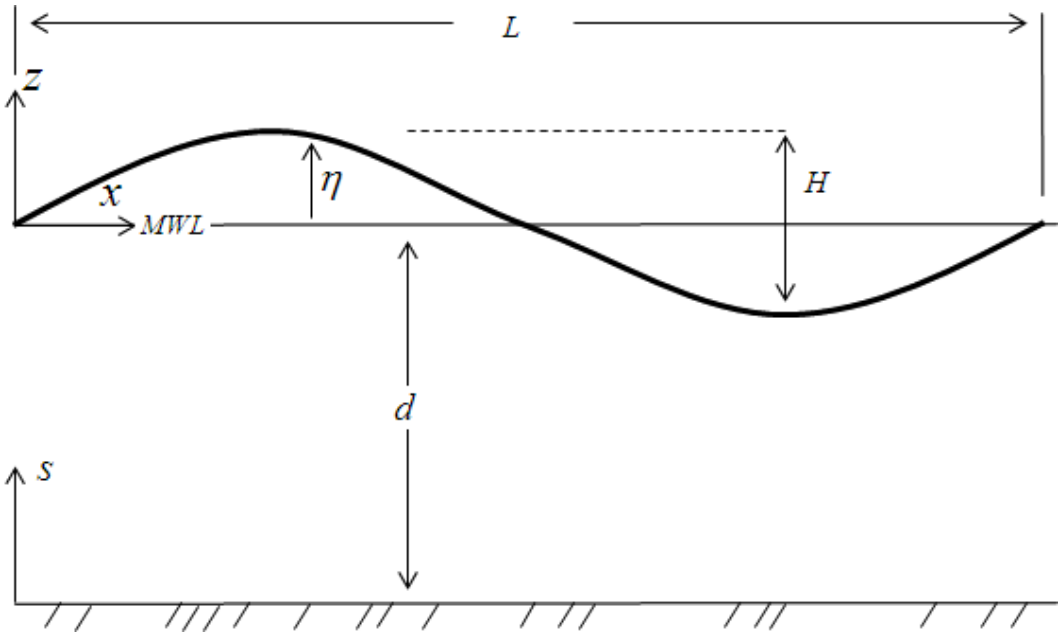

Figure 5 Wave Dimension Schematic

There are several different techniques available to engineers for estimating the wave crest kinematics. These include first-order stretching formulas, linear extrapolation, and second-order methods (Chakrabarti, 2005). Wheeler stretching and Chakrabarti stretching are two common stretching techniques used by ocean engineers. Both Wheeler stretching and Chakrabarti stretching are first order techniques. The kinematics from the seafloor to the wave surface are calculated by stretching the water depth vertically at the crest and shortening it at the trough. The horizontal velocity and horizontal acceleration for Wheeler stretching are

$$u = \frac{gHk}{2\sigma} \frac{\cosh k\left(\frac{s}{1+\eta/d}\right)}{\cosh kd} \cos(\theta) \tag{2.9}$$

$$\dot{u} = \frac{\partial u}{\partial t} = \frac{gHk}{2} \frac{\cosh k\left(\frac{s}{1+\eta/d}\right)}{\cosh kd} \sin(\theta) \tag{2.10}$$

The horizontal velocity and acceleration for Chakrabarti stretching are given as

$$u = \frac{gHk}{2\sigma} \frac{\cosh ks}{\cosh k(d+\eta)} \cos(\theta) \tag{2.11}$$

$$\dot{u} = \frac{\partial u}{\partial t} = \frac{gHk}{2} \frac{\cosh ks}{\cosh k(d+\eta)} \sin(\theta) \tag{2.12}$$

Notice the similarity between the kinematic equations for Wheeler and Chakrabarti stretching and the original unstretched linear wave theory kinematics in equations 2.1 and 2.2. Although modifications change the profile of the kinematic quantities so each is

different, the stretched kinematics should be thought of as versions of the original linear wave theory that are applicable up the free surface.

Using the kinematics from one of the versions of linear wave theory previously discussed, the hydrodynamic forces on the monopile substructure are then calculated. This is accomplished using the Morison equation. The Morison equation is a semi-empirical formulation used to determine horizontal inline forces of unbroken waves on a single vertical cylinder extending from the seafloor to above the free surface (Morison et al., 1950). The resulting force incorporates both a drag component and an inertia component. The force is a function of water depth and wave phase angle (or time) and can be displayed as

$$f_T(s,\theta) = f_D(s,\theta) + f_M(s,\theta) \tag{2.13}$$

where f_T is the total force per unit length for a given location and time, f_D is the drag force contribution, and f_M is the inertia force contribution. The drag component relates to the square of the horizontal velocity among other factors. And the inertial component relates to the acceleration as well as other factors. The two force components are

$$f_D(s,\theta) = \frac{D}{2}\rho C_D \cdot u|u| \tag{2.14}$$

$$f_M(s,\theta) = \frac{\pi D^2}{4}\rho C_M \cdot \dot{u} \tag{2.15}$$

where, ρ is the density of water, D is the cylinder diameter, C_D is the drag coefficient, and C_M is the inertia coefficient. It follows that the total wave force and moment at the seafloor can be expressed as

$$F(\theta) = \int_0^{d+\eta} f_D(s,\theta)ds + \int_0^{d+\eta} f_M(s,\theta)ds \tag{2.16}$$

$$M(\theta) = \int_0^{d+\eta} f_D(s,\theta)sds + \int_0^{d+\eta} f_M(s,\theta)sds \tag{2.17}$$

To determine the location of the total force for a given design wave and phase, the total moment $M(\theta)$ is simply divided by the corresponding total force $F(\theta)$. The result will be the combined moment arm and correspond to a certain height above the seafloor.

There are certain limitations to the use of the Morison equation. It calculates the hydrodynamic loads of a passing wave. It does not determine the impact load of a plunging breaking wave. In order for the Morison equation to hold, the inequality cited in equation 2.18 must be valid. This inequality maintains that the cylinder diameter must be small in comparison to the wavelength.

$$D/L \leq 0.2 \tag{2.18}$$

In summation, linear wave theory, when used to describe a design wave, requires one to specify the wave height, wave period, and water depth. This approach estimates the kinematics and hydrodynamics loads up to the MWL. Linear wave theory can be extended to predict the kinematics from the seafloor up to the crest using stretching techniques. Table 3 provides a complete list of the required design parameters for linear wave theory. All variables and outputs ultimately stem from these seven design parameters.

Table 3 Design Parameters Required For Different Methods

	T	d	H	A	D	a	C_D	C_M	η
LWT	x	x	x		x		x	x	x
DSF	x	x	x		x		x	x	
FNV	x	x		x		x			

2.2 Stream Function Theory Kinematics and Forces

Another approach for determining wave kinematics, and thus wave forces, is a numerical wave theory known as Dean's stream function (Dean, 1965). The theory is interchangeably referred to as stream function theory or Dean's Stream Function (DSF). See for example Dean and Dalrymple (1991). For this approach the solution of the Laplace equation is expressed using a stream function ψ . Instead of an analytical solution like LWT, stream function theory arrives at a solution using a numerical perturbation procedure.

A streamline in a flow is a line with a constant stream function; perpendicular to these streamlines are lines of constant velocity potential. For an incompressible, irrotational, and two-dimensional flow, the velocity potential and stream function exist and both are related through the velocity components (Dean and Dalrymple, 1991). These relationships are known as the Cauchy-Riemann conditions, specifically

$$\frac{\partial \phi}{\partial x} = \frac{\partial \psi}{\partial z}$$
$$\frac{\partial \phi}{\partial z} = -\frac{\partial \psi}{\partial x} \tag{2.19}$$

As outlined by Dean (1974) there are several advantages to stream function theory. Some of the more pertinent advantages are presented here. For a complete

discussion refer to the reference. First, the free wave parameters can be chosen so that the best fit of the dynamic free surface boundary condition is achieved. Consequently, stream function theory achieves greater analytical validity than LWT. Also, the stream function solution is better at reproducing nonlinear waveforms. It is not restricted to the simple sinusoidal free surface waveform of linear wave theory. With stream function theory the troughs can be longer, crests can be steeper, and the wave height does not have to be symmetric about the MWL. This nonlinear feature of stream function theory fits well with the extreme nature of breaking waves.

The application of stream function theory is not as straightforward as linear wave theory. One approach requires the numerical iteration process of solving for the stream function to be completed for each wave investigated. For expediency this numerical iteration is completed using a computer. Or, the process is simplified by running the numerical iteration at certain predetermined points and tabulating the results for future use. Each point relates to a specific relative depth and wave steepness. The solutions from these points are organized into tables of dimensionless parameters. Dean (1974) provides tables using forty points spread out over ten different cases taken at four different ratios of breaking. A figure from Dean (1974) used to establish the basis of the forty points is provided in Figure 6.

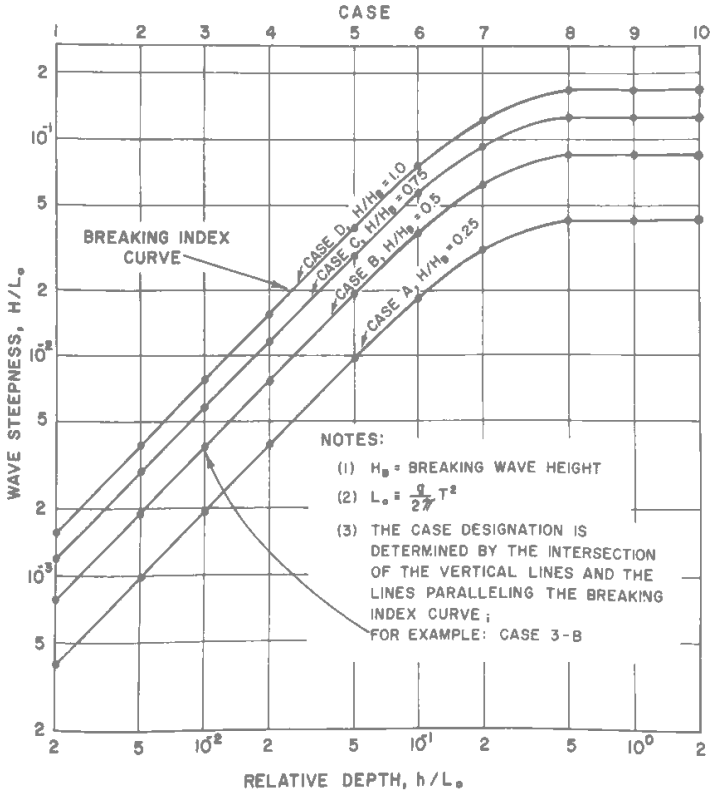

Figure 6 Wave Characteristics Selected for Evaluation in Original Stream Function Tables

Relative depth is defined as d / L. For Figure 6 the wavelength takes the form of deep water wavelength L_o. Wave steepness is defined as H / L. Again in this instance the wavelength used is the deep water wavelength. These two parameters are non-dimensional and are useful in characterizing certain types of wave forms. The formulation for deep water wavelength comes from the deep water approximation using linear wave theory. It is expressed as

$$L_o = \frac{g}{2\pi} T^2 \tag{2.20}$$

The discussion of relative depth introduces an important concept of categorizing water waves. Three different classifications of water waves exist: deep, intermediate, and shallow. A wave can be considered a deep water wave if the relative depth $d/L > 1/2$. A wave can be considered a shallow water wave if the relative depth $d/L < 1/20$. An intermediate wave has relative depths between deep water and shallow water such that the following inequality holds, $1/20 < d/L < 1/2$. For deep water and shallow water waves different approximations exist that allow simplifications to certain calculations. The categories also give the designer an idea of the nature of the wave in relation to the depth. The distinction between the three categories of water waves will be important in later discussions of breaking waves.

In Figure 6 each of the ten cases refers to one of the ten vertical lines of the graph. Each ratio of breaking refers to one of four subsets, A, B, C, and D. Note the breaking ratio is defined as H/H_b, where H_b is the wave height at breaking. The upper most line of interconnected points relating to $H/H_b = 1.00$ represents the breaking index curve for stream function theory. At this limiting ratio waves will break. Refer to section 2.4 for a complete discussion of the breaking index. From this figure it is clear that relative depth and wave steepness are interrelated and describe waves of a specific breaking ratio.

The tables of dimensionless parameters that result from these forty individual cases allow for a wide variety of design variables to be calculated. This discussion will focus on the pertinent values required for determining hydrodynamic loads on a

monopile substructure. There are tables specifically for horizontal velocity, horizontal acceleration, drag and inertia components of the force and moment, as well as the water surface displacement. As presented by Dean (1974), the relevant stream function variables along with their dimensionless forms are provided in Table 4. For a complete discussion of how to use the stream function tables, including the interpolation scheme between tabulated points, refer to Dean (1974).

While a strict quantitative comparison of stream function theory and linear wave theory for breaking waves will be completed in a later section, a qualitative evaluation is possible now. The dimensionless forms of the stream function variables are very similar to those cited in linear wave theory. In fact, the tabulated values for the force and moment equations for stream function theory use the Morison equation. As one example, the expression for the drag force component for the stream function tables cited by Dean (1974) is shown in equation 2.21. Apart from the steam function specific horizontal velocity this is the same construct as the linear wave theory drag force component cited in equation 2.16. This is not particularly surprising given the prominent role the Morison equation plays in determining wave forces on cylinders using kinematic quantities. It is particularly convenient to have the integration completed ahead of time and tabulated for later use.

$$F_D'(\theta, y) = \frac{C_D \rho D}{2} \int_0^{d+\eta(\theta)} u' \left| u' \right| dy \tag{2.21}$$

Table 4 Relevant Stream Function Variables

Stream Function Variable	Dimensionless Form
Horizontal Velocity, $u'(\theta,s)$	$\left[\frac{1}{H/T}\right]u'$
Horizontal Acceleration, $\frac{Du'}{Dt}$	$\left[\frac{1}{H/T^2}\right]\frac{Du'}{Dt}$
Drag Force Component, $F'_D(\theta,s)$	$\left[\frac{2}{C_D\rho D(H/T)^2 d}\right]F'_D$
Inertia Force Component, $F'_I(\theta,s)$	$\left[\frac{4}{C_M\rho\pi D^2(H/T^2)d}\right]F'_I$
Drag Moment Component, $M'_D(\theta,s)$	$\left[\frac{2}{C_D\rho D(H/T)^2 d^2}\right]M'_D$
Inertia Moment Component, $M'_I(\theta,s)$	$\left[\frac{4}{C_M\rho\pi D^2(H/T^2)d^2}\right]M'_I$
Water Surface Displacement, $\eta'(\theta)$	$\left[\frac{1}{H}\right]\eta'$

This comparison illustrates the fact that stream function theory does not calculate hydrodynamic loads any different than the process outlined for linear wave theory. Although the kinematics are of a higher order and more accurately solve the boundary value problem, forces are still calculated using the Morison equation. It is an important distinction however that stream function theory solves for kinematics up into the crest without using additional stretching techniques. Furthermore, stream function theory can better approximate the nonlinear waveforms of extreme waves. While the drag and inertia loads that result from stream function theory kinematics may be more accurate, ultimately the impact load resulting from a plunging breaking wave is still not accounted for.

One interesting similarity between stream function theory and linear wave theory is their requirement of much of the same design parameters. Determining which of the stream function theory tables to use requires knowledge of water depth, wave height, and wave period (which is used to determine deep water wavelength). Once the variable values are known, they must be re-dimensionalized. This again requires the three main design wave parameters in addition to the secondary parameters needed for force and moment calculations. As was the case with LWT, in order to use stream function theory H , d , D, and T must be known when calculating the kinematics and forces on a monopile substructure. Refer to Table 3 for a complete description of the required design parameters for stream function theory. Interestingly, the free surface elevation is not required as an input because the nonlinear wave profile is an output of stream function theory.

2.3 FNV Theory

A more recent wave force formulation that can be used to determine hydrodynamic loads is FNV theory (Faltinsen et al., 1995). O.M Faltinsen, J.N. Newman, and T. Vinje developed the theory to determine nonlinear wave loads on slender vertical cylinders from a diffraction/radiation analysis standpoint. Traditionally, diffraction theory is used when a structure is large, compared to wavelength. The current discussion will be limited to cylindrical structures. When the ratio of diameter to wavelength is greater than 0.2 the prediction based on the Morison equation becomes

suspect. Near and beyond this limit the wave field undergoes significant modification due to the presence of the structure.

The FNV theoretical formulation divides the problem into an outer domain and an inner domain. Conventional linear diffraction analysis confines itself to this outer domain far from the cylinder. The perturbation analysis that is traditionally used to solve the boundary value problem requires an assumption that the wave amplitude is asymptotically small when compared to other length scales, this includes wavelength, cylinder radius, and water depth (Faltinsen et al., 1995). The wave amplitude term requires the wave to take a simple sinusoidal form,

$$A = \frac{H}{2} \tag{2.22}$$

where A is wave amplitude and

$$a = \frac{D}{2} \tag{2.23}$$

where, a is the cylinder radius. In general, the diffraction regime is explicitly stated such that ka=O(1), where k is the wave number and O(1) refers to an order of 1. So the cylinder radius must be comparable to the wavelength. Using the long wavelength regime, FNV theory simplifies this restriction by assuming ka << 1. Simply stated, the wavelength must be significantly less than the cylinder radius.

With this assumption of the long wavelength regime comes an important extension and an added complication. One extension is that the wave amplitude and the cylinder radius are now assumed to be of the same order, such that $A/a = O(1)$. Allowing the wave amplitude to be the same order as the cylinder radius is an essential

feature of FNV theory. One complication that comes from this is that in the inner domain significant nonlinear effects exist when wave amplitude and cylinder radius are of the same order. In solving for these higher order effects, FNV theory allows diffraction/radiation analysis to be applied to waves and cylinders where $A/a \approx 1$.

The first, second, and third-order force components are proportional to A, A^2, and A^3 respectively. The total force is composed of distributed loads and point forces and ka and kA are both assumed small and of order ε. The analysis includes second order forces proportional to $A^2a^2 = O(\varepsilon^4)$ and third-order forces proportional to $A^3a = O(\varepsilon^4)$. For the distributed forces the integrated total loads are proportional to $A^2a^2 = O(\varepsilon^4)$ and $A^3a^2 = O(\varepsilon^5)$. Any terms resulting from higher orders of ε are neglected for the force calculations. For a complete discussion of the derivation of the forces refer to Faltinsen et al. (1995).

The particular form of the force and moment equations cited here are from Klepsvik (1995). The total force is organized into harmonics. The expressions for the total force and each of the contributing forces follow,

$$F_{HT} = F_{H1} + F_{H2} + F_{H3} \tag{2.24}$$

$$F_{H1} = \left[2\pi\rho g A a^2 (1 - e^{-kd}) + \pi\rho g k^2 a^2 A^3\right] \cos\sigma t \tag{2.25}$$

$$F_{H2} = \left[\frac{1}{4}\pi\rho g k a^2 A^2 (1 - e^{-kd}) + \pi\rho g k a^2 A^2\right] \sin 2\sigma t \tag{2.26}$$

$$F_{H3} = -2\pi\rho g k^2 a^2 A^3 \cos 3\sigma t \tag{2.27}$$

where F_{HT} is the total force from FNV theory, F_{H1} is the first force harmonic, F_{H2} is the second force harmonic, and F_{H3} is the third force harmonic. The forces change with time and the passing of the wave and can be expressed in terms of the wave phase angle θ. The total moment follows from the force harmonics. The moment is taken about the seafloor and the z vertical coordinate system is used, i.e. $z = -d$. The equations for the total moment at the seafloor and contributing harmonics follow,

$$M_{HT} = M_{H1} + M_{H2} + M_{H3} + M_{H4} \tag{2.28}$$

$$M_{H1} = \left[2\pi\rho g a^2 A(d - \frac{1}{k} + e^{-kd}) + \frac{1}{2}\pi\rho g k a^2 A^3 + d\pi\rho g k^2 a^2 A^3 \right] \cos\sigma t \tag{2.29}$$

$$M_{H2} = \left[\frac{1}{2}\pi\rho g k a^2 A(d - \frac{1}{2k} + \frac{1}{2k} e^{-2kd}) + d\pi\rho g k a^2 A^2 + \frac{3}{2}\pi\rho g k^2 a^2 A^4 \right] \sin 2\sigma t \tag{2.30}$$

$$M_{H3} = -\left[\frac{1}{2}\pi\rho g k a^2 A^3 + 2d\pi\rho g k^2 a^2 A^3 \right] \cos 3\sigma t \tag{2.31}$$

$$M_{H4} = -\pi\rho g k^2 a^2 A^4 \sin 4\sigma t \tag{2.32}$$

where M_{HT} is the total moment, M_{H1} is the first moment harmonic, M_{H2} is the second moment harmonic, M_{H3} is the third moment harmonic, M_{H4} is the fourth moment harmonic.

FNV theory is fundamentally different from the previous two methods discussed. Linear wave theory and stream function theory calculate the wave kinematics then use the Morison equation to determine the loading. For FNV theory the wave kinematics are not required to calculate the forces; the wave forces are directly calculated from four basic inputs. Upon initial inspection the design wave parameters required for FNV

theory are again variations of H, T, d, and D. The relation of wave number k to parameters such as water depth and wave frequency can be evaluated using the dispersion relation, equation 2.8. For FNV theory, wave number does not necessarily have to come from the linear dispersion relation. If the wavelength of the design wave can be determined another way, then this value can be used. The required design wave parameters and other inputs are displayed in Table 3.

All three theories discussed use variations of the same four core inputs. This is readily apparent in Table 3. The site must be characterized using water depth. The structure must also be considered using either cylinder diameter or radius. Additionally, the design wave requires the main inputs of wave height or amplitude, wave period, and water depth. Conveniently, FNV theory does not require additional drag and inertia coefficients. For FNV theory the resulting output is only applicable for a certain range of cylinder diameters and design waves. Also, like the Morison equation, FNV theory does not account for the impact load of plunging breakers.

2.4 Wave Breaking

Waves break when they reach a limiting wave height and become unstable. This instability is manifested in the crest and results in a collapsed wave form. As briefly explained in the introduction, certain types of breaking waves impart an additional source of loading that goes beyond the loads encompassed in typical hydrodynamic force calculations. So, being able to predict the initiation of breaking as well as the type

of breaking wave is important. Once these factors of breaking waves are determined the possible impact force can be calculated and added to the traditional hydrodynamic load.

The first step in this process is predicting the initiation of breaking given wave parameters and site characteristics. The wave's limiting height, or the maximum height a wave can have before breaking occurs, is a function of water depth and wave length. For deep water waves the wavelength comes into play in determining maximum wave steepness. As cited in the Shore Protection Manual (SPM) of the United States Army Corps of Engineers (1984) this quantity was first formulated using theoretical considerations by J.H. Michell in 1893. The limiting wave steepness is defined as

$$\frac{H_o}{L_o} = 0.142 \approx \frac{1}{7} \tag{2.33}$$

where H_o is the deep water wave height and L_o is deep water wavelength. This limitation results from wave particle velocity in the crest equaling wave celerity. If the particle velocity in the crest exceeds the wave celerity then the wave becomes unstable and breaks. In simple terms, for deep water the maximum wave height that can be generated is one seventh of the wavelength.

The concept of wave celerity is an important one in the context of breaking waves. As a waveform propagates through water the water particles that make up the wave do not undergo a net translation in the direction of the wave. The speed at which this wave form propagates is termed wave celerity C where

$$C = \frac{L}{T} \tag{2.34}$$

For waves in shallow water the depth of the water controls the limiting wave height. The first criterion for shallow water wave breaking was proffered by J. McCowan in 1894 (Dean and Dalrymple, 1991). This criterion states that a wave breaks when it equals a certain fraction of the water depth

$$\kappa = \frac{H_b}{d_b} \tag{2.35}$$

where κ is the wave breaking index, H_b is the breaking wave height, and d_b is the water depth at breaking. The McCowan criterion sets $\kappa = 0.78$. The McCowan formation assumes a solitary wave form, which means the wave exists entirely above the MWL and does not have a trough. Similar to the deep water initiation of breaking, when the horizontal particle velocity in the crest becomes greater than wave celerity the wave becomes unstable and breaks.

The breaking index curve established by the stream function is apparent in Figure 6. The instantaneous slope of the line relating to $H/H_b = 1.00$ is the breaking index for the corresponding relative depth and wave steepness. This comes directly out of the formulation of stream function theory. Not every wave kinematic theory is capable of determining if a wave will break given the input parameters. Consequently, accurately determining at what point the wave will break is important. The breaking index does not always take the form of a constant number as is the case with the McCowan criterion. Being able to have a breaking index change given certain input parameters is a necessary refinement.

The combination of wave steepness and water depth and their interrelated nature in shallow water is important to consider. Miche (1951) developed a model that expands on the geometrical consideration of wave steepness for deep water and transforms it for shallow water. It describes a sinusoidal wave form propagating out of deep water onto a plane and parallel beach,

$$H_b = 0.142L \tanh kd_b \tag{2.36}$$

The deep water asymptote of this equation equals the limiting wave steepness established by Michell. In shallow water the Miche formulation approaches a breaking index where $\kappa = 0.88$. The breaking index for Miche in shallow water is larger than the McCowan criterion. In shallow water this means that for a certain breaking water depth the required incident wave height that will result in breaking will be smaller for McCowan than Miche.

A variety of factors can play a role in the initiation of breaking. One factor that affects the initiation of breaking is bottom slope. Using laboratory results Weggel (1972) developed a model for the breaking index that uses the constant bottom slope of a plane and parallel beach,

$$\kappa = b(S) - a(S)\frac{H_b}{gT^2} \tag{2.37}$$

$$a(S) = 43.75(1 - e^{-19S}) \tag{2.38}$$

$$b(S) = \frac{1.56}{(1 + e^{-19.5S})} \tag{2.39}$$

where S is the bottom slope, $a(S)$ and $b(S)$ are factors that are functions of slope. Beyond bottom slope, other factors such as wave-wave interaction, wind-wave interaction, as well as the influence of current can affect the initiation of breaking. The guiding design documents of the European offshore wind industry use a version of the equation presented by Weggel; this includes the International Electrotechnical Commission's IEC 61400-3 and Germanischer Lloyd's "Guideline for the Certification of Offshore Wind Turbines".

Figure 7 shows the applicability of certain wave kinematic theories over a range of breaking indices as presented in the IEC 61400-3 standard (International Electrotechnical Commission, 2009). The ordinate of the graph uses H/gT^2 which is a dimensionless parameter that describes the wave conditions. The abscissa of the graph uses d/gT^2 and describes a range of water depths and related types of waves. This figure demonstrates elements of the previous discussions on breaking waves. Concerning the breaking wave limit, it is clear that in deep water the limiting wave steepness of Michell governs. But, in moving to shallow water this particular formulation uses the McCowan criterion for determining the breaking limit.

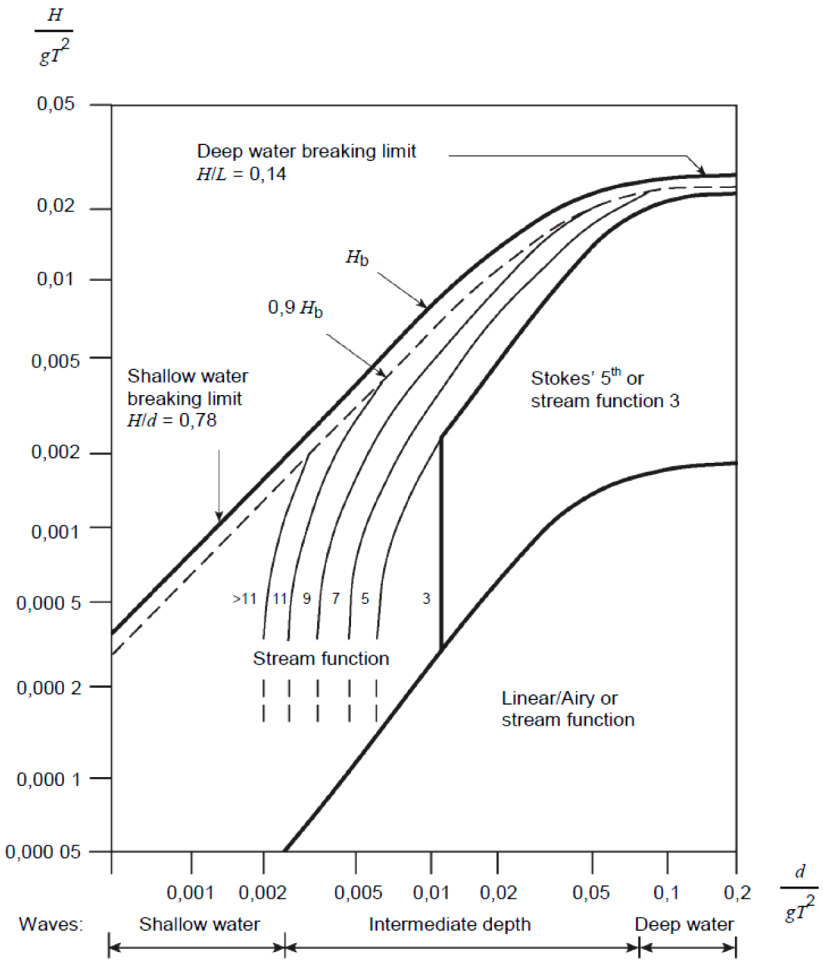

Figure 7 Wave Theory Selection Diagram

Being able to distinguish between spilling and plunging breaking waves given slope and wave conditions is important. Surging beakers are not a factor for offshore wind turbine monopiles given their near shore and bottom slope requirements. Consequently, the discussion will focus on spilling and plunging breakers. A factor known as the surf similarity parameter establishes a mathematical relationship for this distinction (Battjes, 1974) . The surf similarity parameter can take two forms

$$\xi_o = \frac{S}{\sqrt{H_o / L_o}} \tag{2.40}$$

$$\xi_b = \frac{S}{\sqrt{H_b / L_o}} \tag{2.41}$$

where ξ_o is the deep water surf similarity parameter, ξ_b is the breaking surf similarity parameter, and H_o is the deep water wave height. The bottom slope can be expressed as

$$S = \tan\alpha \tag{2.42}$$

where α is the bottom slope. In Table 5 the range of values for the surf similarity parameter corresponding to the different types of breaking waves are presented.

Table 5 Surf Similarity Parameter

Spilling	**Plunging**	**Surging**
$\xi_o < 0.5$	$0.5 < \xi_o < 3.3$	$\xi_o > 3.3$
$\xi_b < 0.4$	$0.4 < \xi_b < 2.0$	$\xi_b > 2.0$

The surf similarity parameter relates the slope with the square root of the wave steepness. So when this ratio is relatively small the breaking wave takes the least extreme form of spilling. But, as bottom slope increases relative to the square root of the wave steepness then the process of breaking leads to more extreme transformations of the waveform. Although the transition between spilling and plunging is gradual in the actual physical sense, the surf similarity parameter provides the designer a construct by

which to judge wave types. Being able on classify a wave as plunging or spilling is important for determining the complete nature of breaking wave loads.

The formulations of LWT and DSF and their application in the Morison equation as well as the formulation of FNV theory do not account for potential sources of loading that are present in types of breaking waves. As soon as a wave breaks, the free surface boundary conditions used in all of the wave force theory formulations no longer apply. The assumption of irrotational flow cannot be justified because the flow of breaking waves must be considered rotational (Lemos, 1992). While the wave force theories are still able to capture the hydrodynamic loads for the majority of the wave, the drastic change of the waveform in the vicinity of the crest introduces a potential source of impact loading. In terms of engineering design, it is necessary to determine the point at which this additional source of loading should be included as well as its magnitude and location.

Using the surf similarity parameter, the transition from spilling to plunging waves indicates the point of additional impact loading. Spilling breakers do not impart a considerable impact load when they break on a substructure. European offshore wind turbine design codes, such as the IEC 61400-3, suggest the use of a high order stream function theory to approximate the load from a spilling breaker. From this prescription it is clear that the wave forces resulting from a spilling breaker are sufficiently approximated by nonlinear wave forms using the methods discussed. From an engineering design perspective no additional force term is needed to calculate the spilling breaking wave force.

When a breaking wave is considered plunging the hydrodynamic force must get an additional term for impact force. This impulsive force results from a mass of water localized in the crest impinging into the structure. This is in stark contrast to the traditional hydrodynamic loads on monopile substructures, which extend from the seafloor to the crest and are ever present during the passing of a wave. The problem of determining the breaking wave force and resulting moment for plunging waves is not approached in a completely different way. The Morison equation and other prevailing methods are adapted to account for the new element of loading. The impact load is simply added to the total load from either the Morison equation or FNV theory. This approach provides a known starting point from which to base the analysis required for design.

Quantifying this large impulsive force is not a trivial task. The traditional approach cited in the SPM for determining the breaking wave force on a cylindrical pile adjusted the drag coefficient C_D and ultimately the drag force in the Morison equation by multiplying by a factor of 2.5 (1984). This method provides a very rough estimate of the expected impact load with no mention of the time history. A method developed by Goda et al. (1966) provides a mathematical formulation for the impact force and its relation to time on slender piles due to breaking waves

$$F_I(t) = \lambda \eta_B \pi \rho a C^2 \left(1 - \frac{C}{a} t\right) \tag{2.43}$$

where $F_I(t)$ is the force of impact as a function of time, λ is the curling factor, η_B is the wave crest elevation above the mean water level, C is the wave celerity, and a is the

cylinder radius. The curling factor λ describes the shape of the breaking wave. Goda's formulation uses the wave celerity as the maximum water particle velocity in the crest, which is similar to the procedure outlined in the SPM (1984). But unlike the procedure in the SPM, Goda's impact force attempts to model the time dependent nature of the force. Refer to Figure 8 for a description of the variables used in impact load calculations. The combination of λ and η_b describes the height of the impact area.

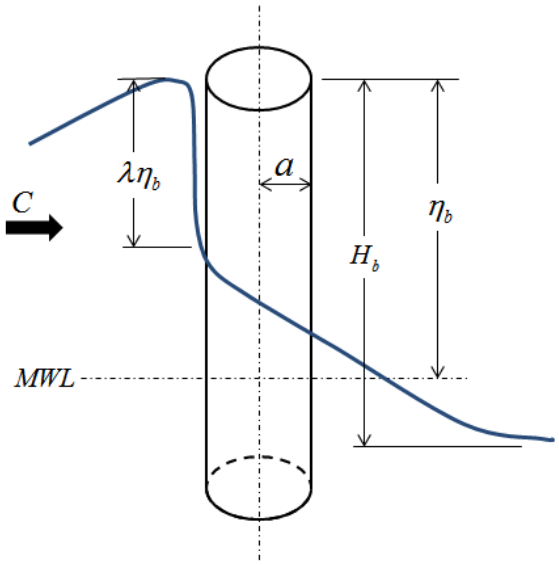

Figure 8 Definition of Impact Variables (Adapted from Wienke and Oumeraci, 2005)

This impact area is assumed to be vertical and moves with a velocity equal to the wave celerity C. The impact force is assumed to be equally distributed within the impact area such that

$$F_I(t) = \int_{\eta-\lambda\eta_b}^{\eta} f_I(t)dy \tag{2.44}$$

$$f_I(t) = \pi \rho a C^2 \left(1 - \frac{C}{a} t\right) \tag{2.45}$$

where $f_I(t)$ is the 2D distributed impact force. Given that the force is assumed to be equally distributed within the impact area the integral is trivial. One important conclusion is that the maximum impact force occurs when the impinging water first makes contact with the cylinder, or when t=0.

The formulation from Goda et al. (1966) has antecedent forms which vary depending on certain assumptions. As outlined by Wienke and Oumeraci (2005), the maximum force from Goda in equation 2.48 is the same as the force cited by the impact theory of von Karman dating to 1929. A different formulation from Wagner in 1932 results in the maximum impact force being two times larger than that of von Karman. Wagner's theory accounts for the pile up effect of the free surface of the wave against the vertical cylinder. Accounting for this physical phenomenon reduces the duration of the impact thereby increasing the maximum force of impact. The general equation for the impact force follows

$$f_I = C_s \rho a V^2 \tag{2.46}$$

where C_s is the slamming coefficient and V is the velocity of the water impacting the cylinder. Another term for V is the impact velocity. The slamming coefficient for von Karman's theory is $C_s = \pi$, while Wagner's slamming coefficient is $C_s = 2\pi$.

A recent formulation by Wienke and Oumeraci (2005) expands on the proceeding impact force theories. It attempts to more accurately model the time history of the impact force given the maximum value. Determining the time history of the force

is important for structural dynamic considerations. Using large scale experiments to verify the approach, a theoretical 2D model determines the impact duration as well as the normal impact force on cylinders of different orientations to the wave crest. The equations hold for cylinders of different yaw angles, extending to 45^o past vertical in either direction of the advancing wave. Using the total force measurements from the experiment the theoretical 3D model for the impact force is also verified.

For Wienke and Oumeraci the 2D result was integrated using the same approach cited in equation 2.49. The resulting total impact force equation is separated into two different functions that span the total duration of impact. The force is presented as a stepwise function,

$$F_I = \lambda \eta_b \rho a V^2 \cos^2\gamma \left(2\pi - 2\sqrt{\frac{V\cos\gamma}{a}t} \cdot \tanh^{-1}\sqrt{1-\frac{1}{4}\frac{V\cos\gamma}{a}t} \right)$$
$$for \quad 0 \le t \le \frac{1}{8}\frac{a}{V\cos\gamma} \tag{2.47}$$

$$F_I = \lambda \eta_b \rho a V^2 \cos^2\gamma \cdot$$
$$\left(\pi\sqrt{\frac{1}{6}\frac{1}{\frac{V\cos\gamma}{a}t'}} - \sqrt[4]{\frac{8}{3}\frac{V\cos\gamma}{a}t'} \cdot \tanh^{-1}\sqrt{1-\frac{V\cos\gamma}{a}t'\sqrt{6\frac{V\cos\gamma}{a}t'}} \right) \tag{2.48}$$
$$for \quad \frac{3}{32}\frac{a}{V\cos\gamma} \le t' \le \frac{12}{32}\frac{a}{V\cos\gamma}$$
$$with \quad t' = t - \frac{1}{32}\frac{a}{V\cos\gamma}$$

where a is the cylinder radius and γ is the angle between the direction of the motion of the mass of water and the perpendicular to the cylinder's axis. For a vertical cylinder this relation of cylinder orientation and water direction is simplified to $\cos\gamma = 1$. For a breaking wave curling over and impacting a vertical cylinder or for inclined cylinders the term becomes $\cos\gamma < 1$. The total duration of the impact is displayed in equation 2.54. The total duration of impact spans from initial contact to the time of complete immersion of half the cylinder.

$$T_I = \frac{13}{32}\frac{a}{V\cos\gamma} \tag{2.49}$$

Looking at the two equations describing the impact force for the Wienke and Oumeraci formulation several interesting conclusions are evident. The resulting 2D impact force is the same magnitude as the Wagner model correlating to a slamming coefficient $C_s = 2\pi$ and the maximum force occurs when t=0. The integration from the 2D case to the 3D representation of the force is usually accomplished by assuming a certain force distribution along the length of the cylinder. Goda et al. (1966) assumes that the force has a rectangular distribution along the entire impact area that results from the assumption that the breaker front was vertical and moved with a velocity equal to the wave celerity. Wienke and Oumeraci claim that an assumption of the force shape is not required. The observed spreading of water from the initial point of contact shows that the impact takes place simultaneously at each level of the cylinder. This description of the impact spreading from an initial contact point is in agreement with the experimental

results. Consequently, the 2D impact force is multiplied by $\lambda\eta_b$ in the course of the integration to calculate the total 3D impact force.

The results from the investigations of Wienke and Oumeraci have other interesting conclusions. They showed experimentally that the wave celerity and maximum horizontal particle velocity are equal for plunging breakers. This confirms the approaches of both Goda et al. and the SPM of setting the impact velocity V equal to the wave celerity C. But, this model refines the force evolution and time duration of the force and results in a shorter, more accurate force time history. As far as determining the location of the resulting impact force, Wienke and Oumeraci suggest using the rectangular impact distribution. This follows directly from confirming that the impact spreads simultaneously along the front line of the cylinder. While it is a rough simplification, it results in a conservative estimate for the calculations of the overturning moment.

Wave breaking is a complicated phenomenon that depends on a number of different factors. Consequently, the process of determining breaking wave loads cannot be described using a single equation or approach. The two main types of breaking waves that affect offshore wind turbine monopile substructures must be treated differently. Combining the impact load with the traditional hydrodynamic loads is critical for a complete engineering design of plunging breakers. Being able to accurately calculate the impact moment is also significant. This distinction between the breaking wave types and the difference in the magnitude of the resulting loads is even more important when a given design site has conditions favorable to both plunging and spilling breaking waves.

Drawing a quantitative comparison of every aspect of this process identifies potential obstacles, necessary complications, and possible simplifications to the engineering design of monopile substructures.

3. SELECTION OF DESIGN CASES

Establishing a basis for the quantitative comparison of the different aspects associated with breaking waves is a necessary next step. Limiting the discussion to a selected range of design cases allows for distinct comparisons to be drawn. Varying parameters such as water depth, wave period, wave height, monopile diameter, bottom slope, and apparent fixity ensures that the comparisons drawn encompass a range of selected cases. Existing developments in Europe and planned wind farms in the United States ground the comparisons in real examples. Applying these examples as the basis, a complete discussion of the rationale behind these choices is required.

3.1 Water Depth and Design Wave Characterization

Looking to the deployable range of monopile substructures previously cited, there are definite limits to the design cases that need to be considered. Starting with water depth proves to be a convenient way of paring down the wide range of design cases available for investigation. Since monopiles are considered a shallow water option in the offshore wind industry the upper limit of a 30 meter water depth is chosen. Looking to existing European examples of monopile substructures, the 30 meter limit captures the deeper range of water depths in which a monopile substructure might be utilized.

Choosing which water depths under 30 meters to consider also requires inputs from existing examples. Looking to the United States, the proposed wind farm Cape

Wind provides a realistic range of water depths for the purposes of the comparison. The proposal for Cape Wind utilizes monopile substructures in water depths ranging from 2 meters through 18 meters. This range represents the tidal range of the site as well as the natural bathymetric variation over the entire area of the wind farm. Site and storm characteristics such as tidal range and storm surge must be considered when determining a design water depth for a particular site. For the purposes of this analysis providing a range of water depths with incremental steps will provide the detail necessary to draw meaningful comparisons. In summary, the upper limit established in the European industry and the incremental range of shallower water of Cape Wind provides the basis for the water depths chosen. The water depths chosen for analysis are 3, 6, 10, 15, and 30 meters. For matters of simple comparison this corresponds to water depths ranging from roughly 10, 20, 33, 50, and 100 feet.

With the water depths established, the range of wave periods and wave heights follow. The prevailing wave climate of a particular site is tied to the water depth of the area surrounding the design site, the prevailing wind conditions, and the location of the site in relation to the area over which the wind is acting. Therefore, each particular site will have distinct wind and wave design values. This analysis is not concerned with a particular site. Rather, for purposes of comparison a wide range of wave periods will be investigated. Using a range of wave periods and wave heights will allow for a variety of breaking wave types to be investigated. Each combination of water depth and wave period results in a different breaking wave height.

The types of waves of interest are known as short period gravity waves. Examples of short waves include wind waves and swell. Short waves are typically considered to have periods of less than 20 seconds. Ocean waves that result from a storm can have dominate periods between 5 and 15 seconds. For the analysis of breaking waves a range of periods between 4 and 20 seconds is chosen. This spread will provide a generous range of wave periods from which to draw comparisons.

The resulting analysis does not include a discussion of the likelihood of encountering the particular combinations of wave period, water depth, and wave height. For a discussion of likelihood to be pertinent, a particular site would have to be chosen and the prevailing wind and wave climate determined. Instead, grounding the discussion in realistic water depths and with a range of wave periods allows the analysis to exist solely as a comparison of the methods. In the end, this approach will allow for a more general assessment of the engineering design of breaking waves.

Implied in this discussion of breaking waves is the time-dependent deterministic approach used for extreme loading conditions. The deterministic method uses a characteristic design wave which corresponds to a particular wave height, wave period, and singular wavelength. This approach stands in stark contrast to the stochastic approach typically employed for nominal condition loadings such as fatigue and dynamic structural response (Sarpkaya and Isaacson, 1981). The stochastic approach operates in the frequency domain and requires the use of wave spectra, the force-transfer function, and the resulting force-response spectra. The distinction between the deterministic approach and the stochastic approach is meant to clearly define the

approach being used here. Due to the extreme nature of breaking waves, the deterministic approach is used to define monochromatic design waves. The design cases for this analysis are generated using the range of water depths and wave periods and consist of a number of distinct design waves.

3.2 Cylinder Diameter and Apparent Fixity

Cylinder diameter and apparent fixity are important parameters which affect the magnitude of forces and moments that result from breaking waves. Choosing a range of cylinder diameters on which to base the analysis also follows from existing examples of offshore wind turbine monopile substructures. Cited in the introduction, the range of monopile diameters varies depending on a site's design conditions. For the purposes of this analysis, cylinder diameters of 3.5, 5, and 6.5 meters were chosen. These diameters will be used for the large scale comparisons across the entire range of design water depths. There are times when other diameters are used for secondary calculations and comparisons. These other diameters will still fall within the general range of diameters cited here. For a quick comparison, these values correspond to roughly 12.5, 16.5, and 21 feet. These design diameters provide a sufficient range of realistic diameters.

Using a constant diameter cylinder to model monopile substructures represents a simplification from the actual design. By their very nature the monopile foundation pile and transition piece are different diameters. The transition piece is larger and caps the foundation pile. In the context of breaking waves the transition piece will be the structure on which the crest of the breaking wave will act. Assuming the transition piece

diameter extends the entire length of the pile is a conservative approximation. For this reason the diameter of the transition piece should be taken as the diameter used in the force calculations.

Introducing the concept of apparent fixity is important for an accurate estimation of the effective length of the monopile. Knowing the effective length of the monopile is important for determining the bending moments and dynamic response. The concept of apparent fixity uses cylinder diameter as a means of including the pile-soil interaction without the use of an additional soil model. The moment equations previously cited assume that the monopile is fixed at the seafloor, so the effective length of the pile is simply the water depth. In this example the level of apparent fixity would be zero.

In actuality the pile is not perfectly fixed right at the seafloor. The horizontal stiffness of the soil requires a certain depth before the pile can be assumed to be fixed. The depth at which the pile is fixed is known as the apparent fixity level. It is possible to apply different approximations of apparent fixity depending on the soil type of the particular site. The guidelines on apparent fixity assume that for general calculations, in the absence of soil data, an apparent fixity depth of 6 times the cylinder diameter be used (Hallam et al., 1978). For the purposes of this analysis, this guideline on apparent fixity will be used. By adding an apparent fixity depth of 6D, the effective length of the pile increases. A larger effective length results in larger bending moments in the monopile substructure.

4. NUMERICAL SIMULATION AND RESULTS

The majority of this section makes use of dimensionless parameters in the organization of results. Dimensionless parameters and factors allow for a wide range of information to be conveyed in a concise manner. Regardless of the unit system used to determine the information being displayed, dimensionless parameters allow for broader conclusions to be drawn from the results. A common dimensionless parameter used to categorize and display results is d/gT^2 . Cited in section 2.4, it is commonly used as a means of displaying a range of water depths and wave conditions that correlate to the water wave categories. The ranges of this parameter follow;

$$\begin{aligned} 0.0025 &< \frac{d}{gT^2} \quad (Shallow) \\ 0.08 &> \frac{d}{gT^2} \quad (Deep) \end{aligned} \tag{4.1}$$

where intermediate water waves fall between these two boundary values.

Another dimensionless parameter that is extensively used in the results section is the ratio of cylinder diameter to wavelength. This ratio was introduced in section 2.1. When $D/L < 0.2$ then the Morison equation is considered applicable. At larger values the diffraction effects become important and the Morison equation is no longer able to adequately model the wave force. In the results section this dimensionless parameter will provide a backdrop for comparing FNV theory with the other methods of determining wave forces.

4.1 Stream Function Program Verification

The stream function portion of the analysis was completed using a version of the interpolation scheme mentioned in section 2.2. Given inputs of wave height, wave period, and water depth, the MATLAB program is designed to determine the kinematics of the particular wave form. The inputs are used to determine the location of the wave form relative to the computed points. Instead of interpolating the tabulated kinematic results in Dean (1974), the results utilize the dimensionless stream function coefficients to calculate the kinematics. The relative order of the solution is determined using an interpolation scheme of the orders of the solutions of the closest points. Determining this order limits the number of stream function coefficients to include in the solution. With the order of the solution known, the dimensionless stream function coefficients of the surrounding points are used in another interpolation. The kinematics are then calculated using the interpolated dimensionless stream function coefficients along with the modified order of the solution. For a complete discussion of using the dimensionless stream function coefficients to calculate the kinematics refer to Dean (1974).

As a means of testing the interpolation regime used in this particular stream function program, the original figure cited in Dean (1974) was reproduced. The figure being reproduced is Figure 6 and can be found in section 2.2. The stream function program was tested by choosing a range of water depths and wave periods relating to a particular relative depth. Then, wave heights were cycled through and chosen when they reached within 10^{-3} of the breaking index line of interest. This level of accuracy was achieved through the use of very small incremental steps in all three parameters: water

depth, waver period, and wave height. The results are displayed in Figure 9. From the comparison of the two figures it is clear that the interpolation scheme of the stream function program accurately reproduces the original stream function breaking index curves.

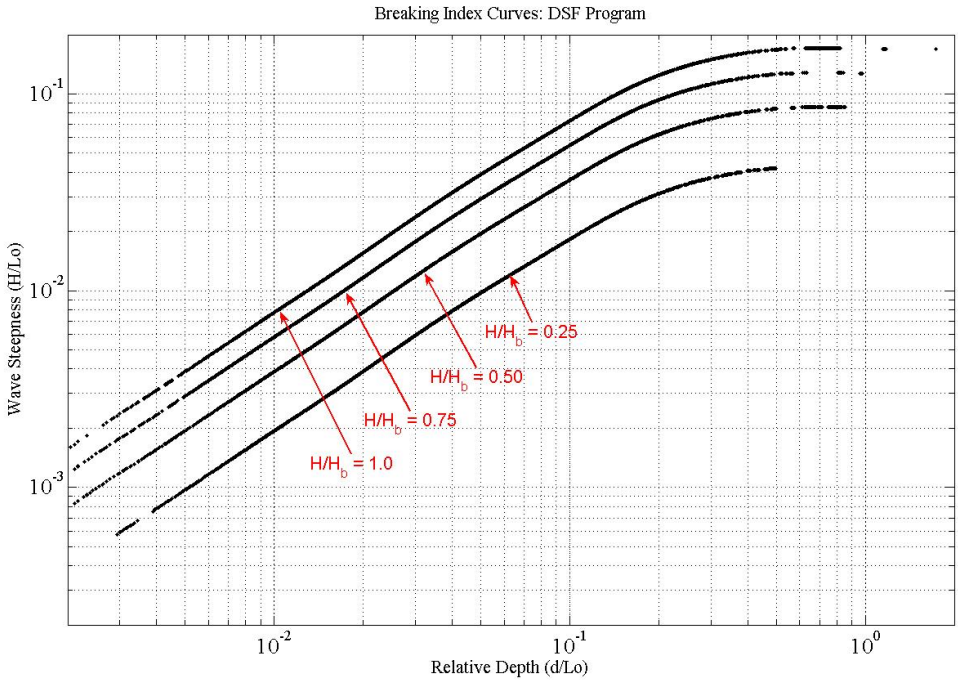

Figure 9 Stream Function Program Breaking Index Curve Comparison

Another test of the stream function program uses the tabulated results in Dean (1974) as a benchmark. Five points on the breaking index curve, for which tabulated results are known, are used as the standard. These points are displayed in Table 6. Looking at Figure 10 it is clear that the program is able to successfully reproduce the exact values of wavelength divided by deep water wavelength (L/L_o). Furthermore, this

figure shows that the program is able to interpolate between the known tabulated values and reproduce a smooth line between the points. This comparison is completed using a depth of 6 meters. A depth of 6 meters is the only investigated depth that spans this particular range of d/gT^2 while maintaining periods between 4 and 20 seconds. Figure 10 and Figure 9 illustrate the validity of the stream function program when considering wave characteristic values such as wave height and wave length.

Table 6 DSF Comparison Points (d=6m)

Tabulated Points	d/L_o	d/gT^2	d=6m	
			H_b (m)	T (s)
3D	0.01	0.0016	4.640	19.613
4D	0.02	0.0032	4.675	13.869
5D	0.05	0.008	4.680	8.771
6D	0.1	0.0159	4.400	6.202
7D	0.2	0.0318	3.730	4.386

The interpolation of the dimensionless stream function coefficients at the predetermined points shows that the program is able to reproduce the kinematic values of the tables. Again, the dimensionless stream function coefficients are used to calculate the kinematics. Each tabulated point has a certain number of these coefficients depending on the order of the solution. The program determination of kinematics at the exact points is accurate. Table 7 uses dimensionless horizontal velocity at point 7D to illustrate the level of similarity between the tabulated results and the program's interpolation of the information. The table presents a horizontal range of theta values and a vertical range of dimensionless depth values. The percent error takes the difference

between the values and divides it by the tabulated result. The program is clearly able to interpolate the solution to a reasonable degree at or directly around the known points.

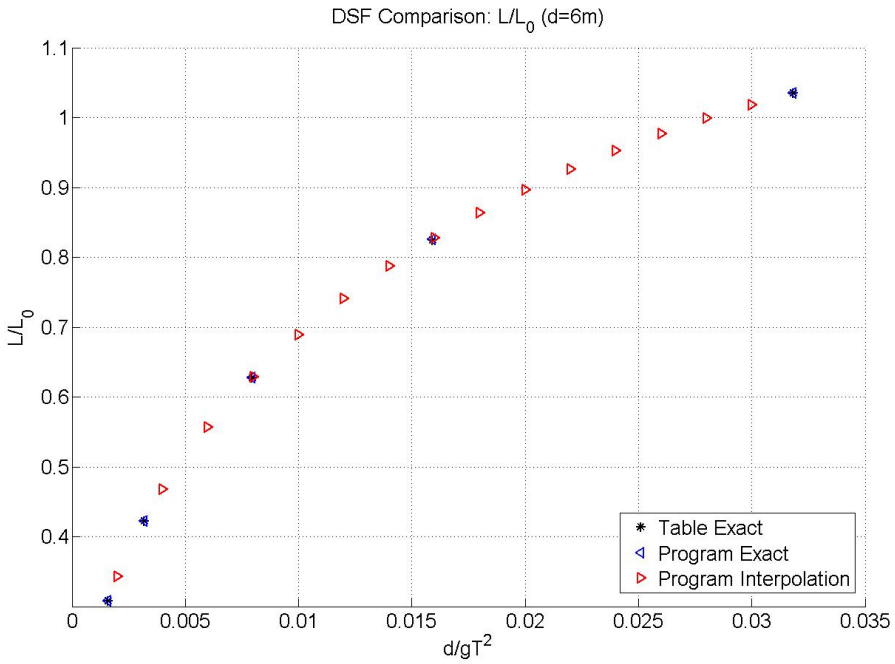

Figure 10 DSF Comparison of Tables and Program Using L/L_o

The interpolation of the dimensionless stream function coefficients between the tabulated points on the breaking index curve is less promising. Figure 11 shows the inaccuracies of the interpolation of the dimensionless stream function coefficients using a comparison of the resulting maximum forces. Looking at the figure it is clear that the five exact program solutions at the tabulated points have a smooth declining trend with increasing d/gT^2. The interpolation of the regions between these points differs considerably halfway between points.

Table 7 DSF Table and Program Comparison: Dimensionless Horizontal Velocity (Point 7D)

	Theta (degrees)	0		20		75		180	
		Table	Program	Table	Program	Table	Program	Table	Program
S/Depth	Surface	**7.62**	**7.60**	**3.98**	**3.98**	**0.00**	**0.01**	**-1.61**	**-1.61**
	% Error	*0.25*		*-0.16*		*-35.80*		*-0.04*	
	1.4	**6.67**	**6.66**	~	~	~	~	~	~
	% Error	*0.20*							
	1.2	**4.39**	**4.39**	**3.59**	**3.59**	~	~	~	~
	% Error	*-0.04*		*-0.09*					
	1.0	**3.16**	**3.16**	**2.73**	**2.74**	~	~	~	~
	% Error	*-0.17*		*-0.16*					
	0.8	**2.40**	**2.40**	**2.13**	**2.14**	**0.12**	**0.12**	**-1.58**	**-1.58**
	% Error	*-0.24*		*-0.23*		*-0.04*		*-0.23*	
	0.6	**1.91**	**1.91**	**1.73**	**1.73**	**0.18**	**0.18**	**-1.40**	**-1.40**
	% Error	*-0.26*		*-0.30*		*0.16*		*-0.21*	
	0.4	**1.61**	**1.61**	**1.47**	**1.47**	**0.21**	**0.21**	**-1.27**	**-1.27**
	% Error	*0.02*		*-0.04*		*-0.09*		*-0.09*	
	0.2	**1.44**	**1.44**	**1.33**	**1.33**	**0.22**	**0.22**	**-1.19**	**-1.19**
	% Error	*-0.07*		*-0.05*		*-0.05*		*-0.14*	
	0.0	**1.39**	**1.39**	**1.28**	**1.28**	**0.23**	**0.23**	**-1.16**	**-1.16**
	% Error	*-0.07*		*-0.11*		*-0.07*		*-0.15*	

As d/gT^2 increases, the values diverge from one point then converge on the next. The level of convergence and divergence increases for deeper water waves. This increasing inaccuracy has an effect on important design values such as maximum force. While the interpolation may be inaccurate to a certain level, this inaccuracy is amplified as parameters such as cylinder diameter are increased. At the point of breaking, the interpolation of the dimensionless stream function coefficients using the stream function

program proves to be an inaccurate method of determining non-tabulated stream function coefficients.

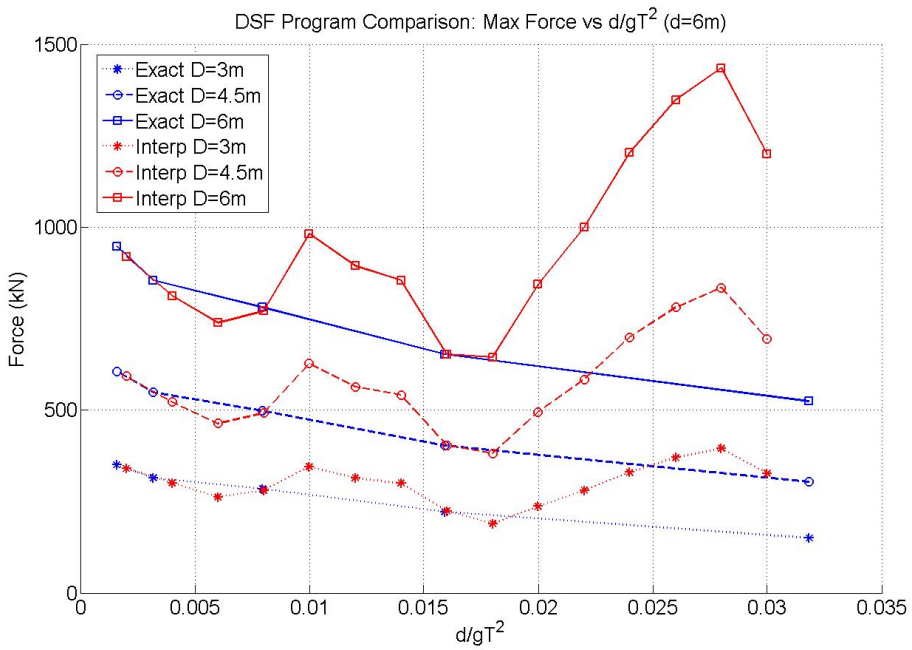

Figure 11 DSF Coefficient Interpolation Comparison using Maximum Force

In summation, the stream function program has limited areas of application. The program is able to reproduce the full range of breaking wave characteristics such as wave lengths, surface profiles, and breaking wave heights. It also accurately reproduces the solution around the tabulated points. Design values such as the kinematics and the resulting forces can be determined directly at these locations. The stream function program does not accurately interpolate the dimensionless stream function coefficients between points on the breaking index curve $H/H_b = 1.0$. If the breaking wave of interest

lies between tabulated points, the stream function program kinematics should not be used.

4.2 Breaking Wave Height Determination and Comparison

Determining the breaking wave heights that result from each of the methods outlined in section 2.4 is key. Comparing the resulting breaking wave heights allows for differences between each of the breaking wave models to be determined. This comparison is not meant as a discussion of the validity or accuracy of each particular method. Rather, the comparison is meant to clearly establish the differences and similarities of the different approaches available to the design engineer. Investigating the full range of shallow, intermediate, and deep water waves is the first step before the analysis is focused on the range of water depths and wave periods of interest.

Each model has varying degrees of difficulty in determining the breaking wave height. The following three are straight forward and require little discussion. The simplistic nature of the McCowan criterion makes this process trivial. A water depth is chosen for investigation and the breaking wave height follows from the multiplication of the McCowan breaking index $\kappa = 0.78$ with the water depth. For this method there is no dependence on other factors. In contrast, the Miche formula requires an additional step but is still relatively simplistic. Once the water depth is chosen, a wavelength is then required to calculate the breaking wave height. In this analysis the wavelength was calculated using the wave period and linear dispersion relation. For the Weggel formula, the process of determining the breaking wave height requires more computation.

Looking at equation 2.38 it is clear that the breaking wave height occupies both sides of the equation. Using an iterative process, the correct breaking wave height was determined. This formula also requires wave period as an input. Given the additional factor of bottom slope, this greatly increases the number of breaking wave heights possible for a given water depth and wave period.

Determining the breaking wave heights that result from Dean's stream function is more involved than the first three models. In section 2.2, a discussion of the breaking index that is evident in Figure 6 demonstrated the capability of the stream function formulation to determine when a wave will reach the point of breaking. Using the outputs from the stream function program verification, the breaking index curve of $H/H_b = 1.0$ was reproduced and graphed using H/T^2 on the ordinate and d/gT^2 on the abscissa. The resulting line made up of individual points at the point of breaking is displayed in Figure 12. The range of the independent non-dimensional variable chosen for investigation is well within the shallow, intermediate, and deep water wave categories.

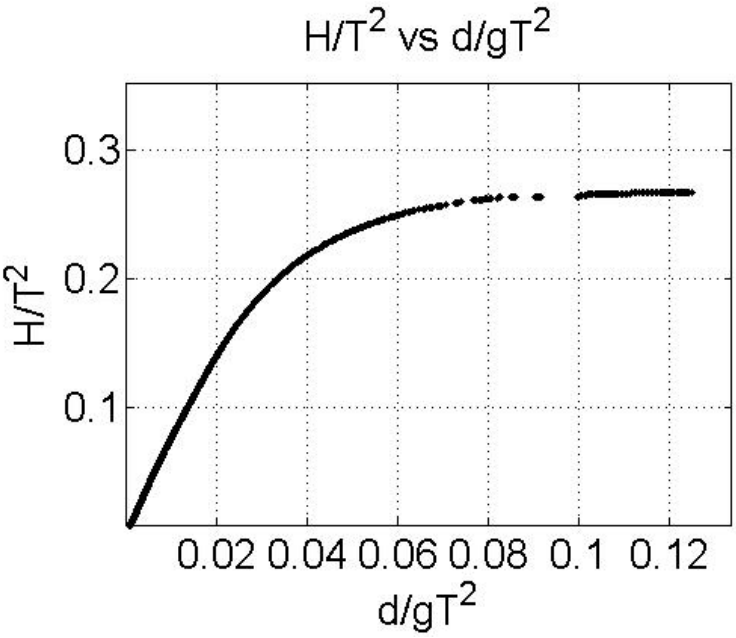

Figure 12 Stream Function Breaking Index (H/T^2 vs. d/gT^2)

With the breaking index curve determined using the stream function program, a line is then fit to the curve. Using the statistical program "R", the equation for the curve was determined using polynomial regression. Table 8 outlines the parameters for comparison in choosing the model. Ultimately, a 6th order model was chosen. Maximizing the goodness of fit and minimizing the information criterions (AIC, BIC) suggested the use of a 6th order polynomial over the other options. The AIC and BIC demonstrate that relative to the 5th order, the added parameters of a 6th order polynomial are justified given the increased goodness of fit. Along the same lines, this added complexity of a 7th order polynomial is not warranted. Table 9 presents the equation of the breaking index curve and the coefficients for the 6th order polynomial of best fit. Note that for the equation in Table 9, y is H/T^2 and x is d/gT^2.

Table 8 Polynomial Regression of Stream Function Breaking Index Overview

Polynomial Order	**2**	**3**	**4**	**5**	**6**	**7**
Residual Standard Error	7.514E-03	1.327E-03	1.319E-03	7.294E-04	4.674E-04	4.674E-04
R-squared	0.9885	0.9996	0.9996	0.9999	1.0000	1.0000
AIC	-25990	-38960	-39010	-43440	-46770	-46770
BIC	-25960	-38930	-38972	-43400	-46720	-46720

Determining the breaking wave height for stream function theory comes from the equation of the breaking index curve from the polynomial regression. The equation for the breaking wave height from stream function theory can be written as

$$H_b = T^2 \cdot \sum_{j=0}^{6} \alpha_j \left(\frac{d}{gT^2} \right)^j \tag{4.2}$$

where the terms encompassed in α_j are found in Table 9. The model was fit for d/gT^2 values between $7.5x10^{-4}$ and 0.125. The percent difference between the breaking wave height from regression and the breaking wave height from the stream function program is displayed in Figure 13. The resulting breaking wave height from equation 4.2 has greater difference for shallow water waves, but oscillates about the actual value for intermediate and deep water waves. With this equation any breaking wave height can be determined using different water depths and a range of applicable wave periods.

Table 9 Polynomial Equation of 6th Order and Coefficients

$y = \sum_{j=0}^{6} \alpha_j (x)^j$	
$\alpha_0 =$	-1.93E-04
$\alpha_1 =$	7.75E+00
$\alpha_2 =$	7.33E+00
$\alpha_3 =$	-3.24E+03
$\alpha_4 =$	5.40E+04
$\alpha_5 =$	-3.65E+05
$\alpha_6 =$	9.13E+05

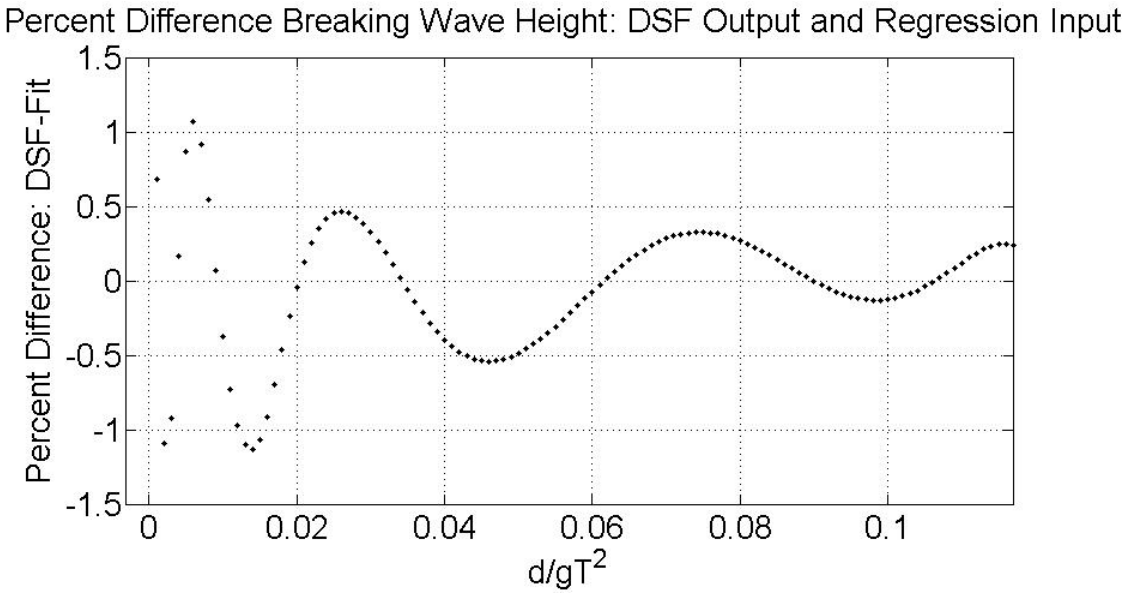

Figure 13 Percent Difference of Breaking Wave Heights from DSF program and Regression

With the breaking wave heights for each model determined, the comparison of results follow. Figure 14 shows each model's breaking index curve in relation to the axes

H/T^2 and d/gT^2 used in the regression analysis. Note that for intermediate to deep water waves the stream function approach is nearly the same as the Miche model using the wave length that comes out of stream function theory. Another thing to note is that for a flat bottom condition $(\alpha = 0)$ the Weggel breaking model is the same as the McCowan criterion. Figure 15 shows a shallow to intermediate water detail of the breaking index curves. For deep water waves the McCowan criterion diverges considerably. This is to be expected considering its shallow water formulation. For shallow to intermediate water waves the McCowan criterion converges with the other models.

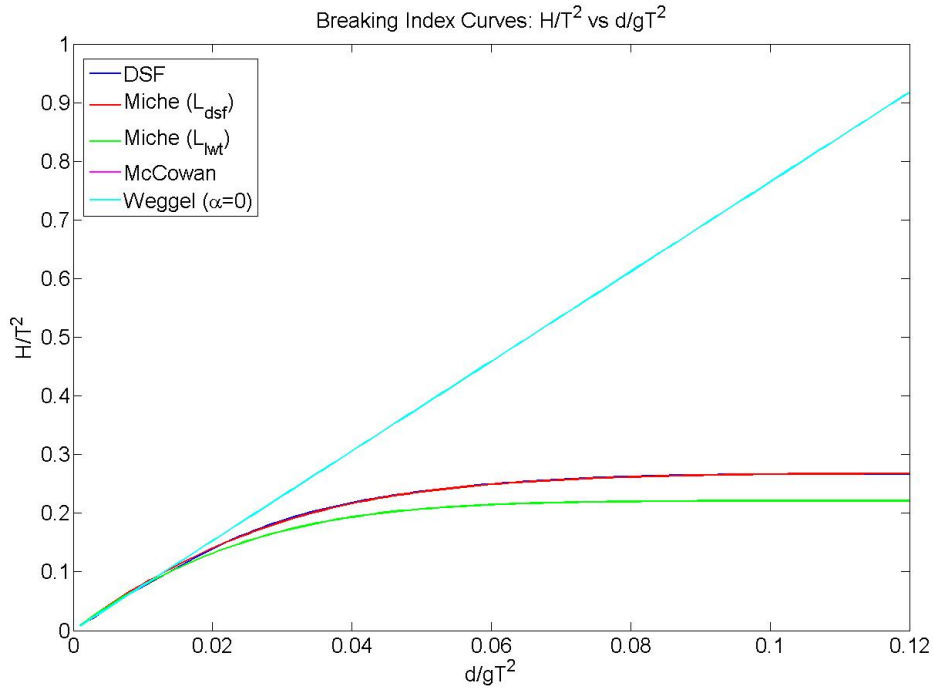

Figure 14 Breaking Index Curve Comparison

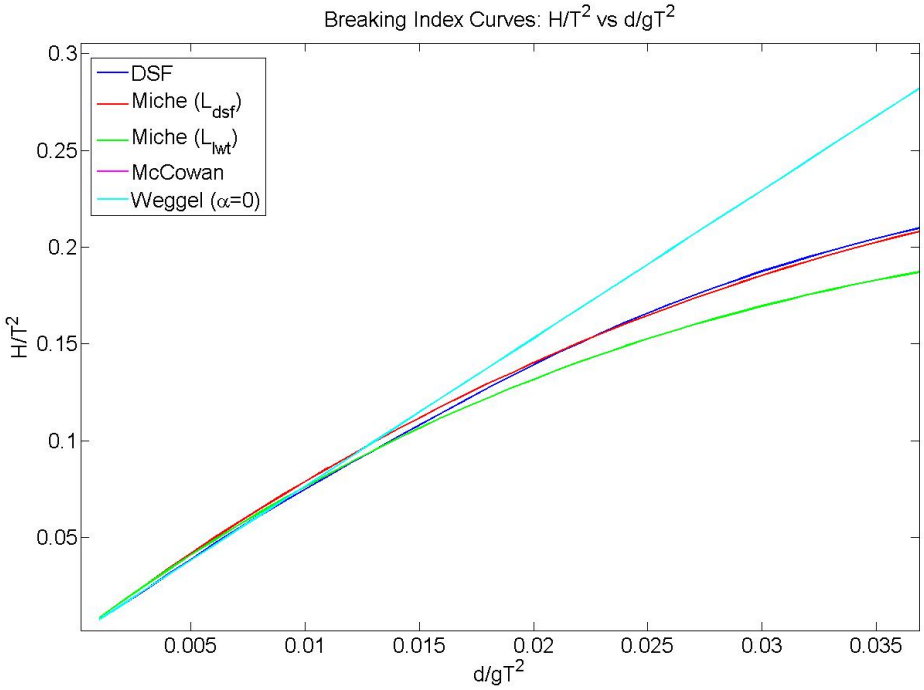

Figure 15 Breaking Index Curve Comparison: Shallow to Intermediate Detail

The role bottom slope plays in determining the breaking wave height only enters into the Weggel model. Figure 16 shows the comparison of breaking index curves over a range of bottom slopes. For intermediate to deep water waves, the greater the slope the closer the Weggel index curve approaches the stream function curve. Figure 17 shows a shallow to intermediate detail of the same changing slopes. The relation present for deeper water waves is flipped for shallow to intermediate water waves. Weggel's model diverges from the DSF curve in shallow water for increasing bottom slopes.

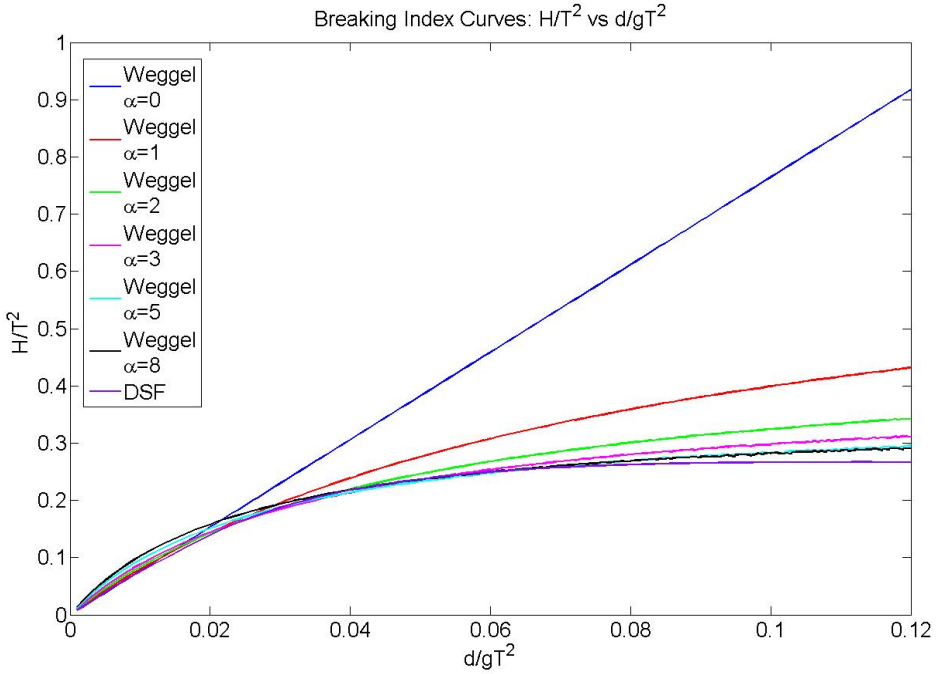

Figure 16 Breaking Index Curve Comparison for Changing Bottom Slope

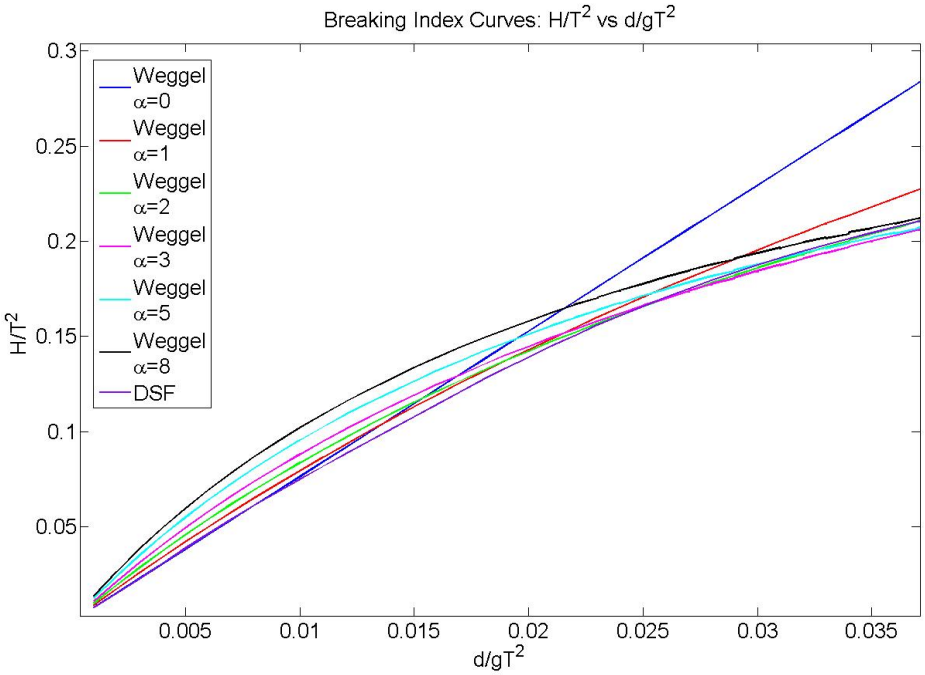

Figure 17 Breaking Index Curve for Changing Bottom Slope: Shallow to Intermediate Detail

Commenting on the differences between breaking index curves can only take the comparison of breaking wave heights so far. The stream function breaking wave heights were taken as a baseline used for comparison. Figure 18 shows the percent difference of the stream function breaking wave height in relation to the other breaking wave height models. A negative percent difference means that the stream function breaking wave height is less than the model being compared to. For positive percent differences the opposite is true. Figure 19 shows the percent difference of the stream function breaking wave height when compared to a range of bottom slopes using Weggel's model. For shallow to intermediate water the marked effect that the bottom slope plays in changing the wave height of the Weggel model is clear. It should be noted that DSF does not take the bottom slope into account when determining the breaking wave height.

The interesting thing about using percent difference is that the trend is the same for all water depths and wave periods investigated. For example, at a particular value of d/gT^2 the percent difference between methods is the same for a depth or 3m or a depth of 30m. In order to transfer from percent difference of breaking wave height to actual breaking wave heights the following simple formula can be used

$$H_{b\_other} = H_{b\_dsf}\left[\frac{1-\left(\%/200\right)}{1+\left(\%/200\right)}\right] \tag{4.3}$$

where H_{b_other} is the breaking wave height in question, H_{b_dsf} is the breaking wave height from the stream function, and % is the percent difference (including sign) of the point in question.

The discussion of breaking wave heights and establishing a range of design cases for investigation is crucial for future steps. The range of design cases was selected using the criteria established in section 3. Using the design water depths of 3, 6, 10, 15, and 30 meters, and a range of wave periods between 4 and 20 seconds, the breaking wave heights were determined using the stream function breaking wave height equation. The resulting cases were organized around d/gT^2 values between 0.002 and 0.03 at uniform intervals. The design cases used for the majority of the analysis are presented in Table 10. The resulting 64 points represent waves just inside the shallow limit of 0.0025 to waves only partially intermediate.

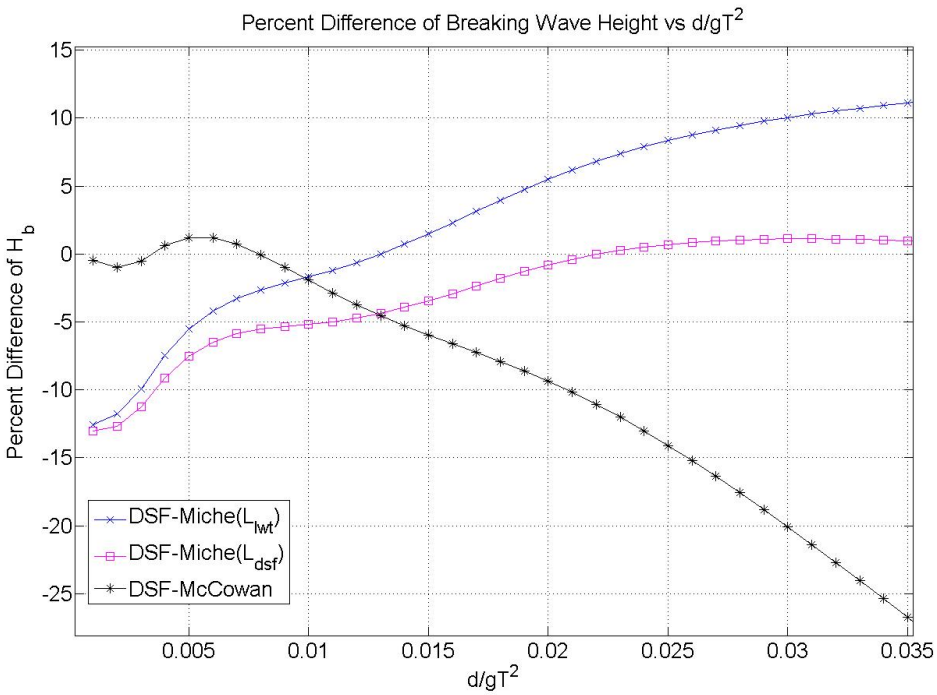

Figure 18 Percent Difference Breaking Wave Height: DSF-Other Detail

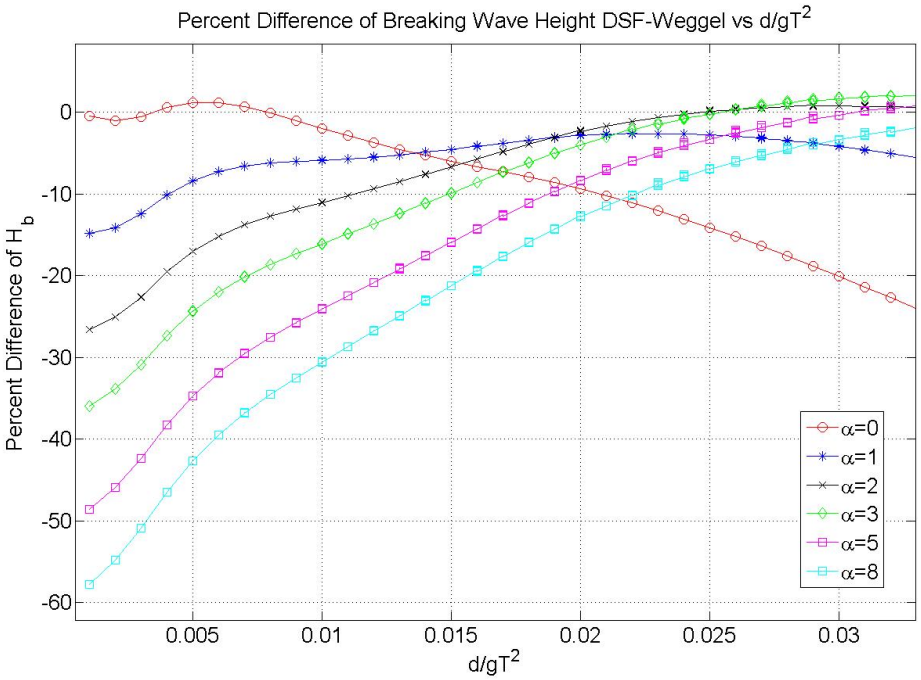

Figure 19 Percent Difference of Breaking Wave Height: DSF-Weggel Detail

Table 10 Design Cases Chosen for Analysis

	d=3m		d=6m		d=10m		d=15m		d=30m	
d/gT^2	H_b (m)	T (s)	H_b (m)	T (s)	H_b (m)	T (s)	H_b (m)	T (s)	H_b (m)	T (s)
0.002	2.34	12.37	4.68	17.50	~	~	~	~	~	~
0.004	2.35	8.75	4.70	12.37	7.83	15.97	11.75	19.56	~	~
0.006	2.34	7.14	4.68	10.10	7.81	13.04	11.71	15.97	~	~
0.008	2.33	6.19	4.65	8.75	7.75	11.29	11.63	13.83	23.26	19.56
0.01	2.30	5.53	4.61	7.82	7.68	10.10	11.52	12.37	23.04	17.50
0.012	2.28	5.05	4.55	7.14	7.59	9.22	11.38	11.29	22.77	15.97
0.014	2.25	4.68	4.49	6.61	7.48	8.54	11.23	10.46	22.45	14.79
0.016	2.21	4.37	4.42	6.19	7.37	7.99	11.05	9.78	22.10	13.83
0.018	2.17	4.12	4.34	5.83	7.24	7.53	10.86	9.22	21.72	13.04
0.02	~	~	4.26	5.53	7.11	7.14	10.66	8.75	21.32	12.37
0.022	~	~	4.18	5.28	6.96	6.81	10.45	8.34	20.89	11.80
0.024	~	~	4.09	5.05	6.82	6.52	10.23	7.99	20.45	11.29
0.026	~	~	4.00	4.85	6.67	6.26	10.00	7.67	20.00	10.85
0.028	~	~	3.91	4.68	6.51	6.04	9.77	7.39	19.54	10.46
0.03	~	~	3.81	4.52	6.36	5.83	9.53	7.14	19.07	10.10

4.3 Type of Breaking Wave Determination

Knowing the type of breaking wave is important for future force and moment calculations. The additional impact load of plunging breakers needs to be considered. Using the surf similarity parameter cited in section 2.4, the type of breaking wave is displayed in Figure 20 for the range of water depths and wave periods under investigation. It is clear that for slopes ranging from 0 to 2 degrees the wave types are entirely spilling. With a slope of 8 degrees the wave type is entirely plunging. For the slopes that have both plunging and spilling cases, typically the shallower waves are more prone to plunging type breaking.

Knowing how the surf similarity parameter acts in relation to breaking wave height is important. Figure 20 uses the breaking wave height from the stream function. Looking at equation 2.42, the surf similarity parameter will decrease with increasing breaking wave height. If the height of a breaking wave is determined using the Weggel model, then the wave will have a smaller surf similarity parameter. Refer again to Figure 19 for a comparison of DSF and Weggel breaking wave heights. This means that using larger breaking wave heights results in waves less prone to plunging type breaking. For the design engineer, using a larger breaking wave height will result in a design case theoretically less susceptible to additional impact loads. For this reason, the breaking wave height determined with the stream function returns a more conservative estimate of a wave's transition from spilling to plunging when compared to Weggel's model.

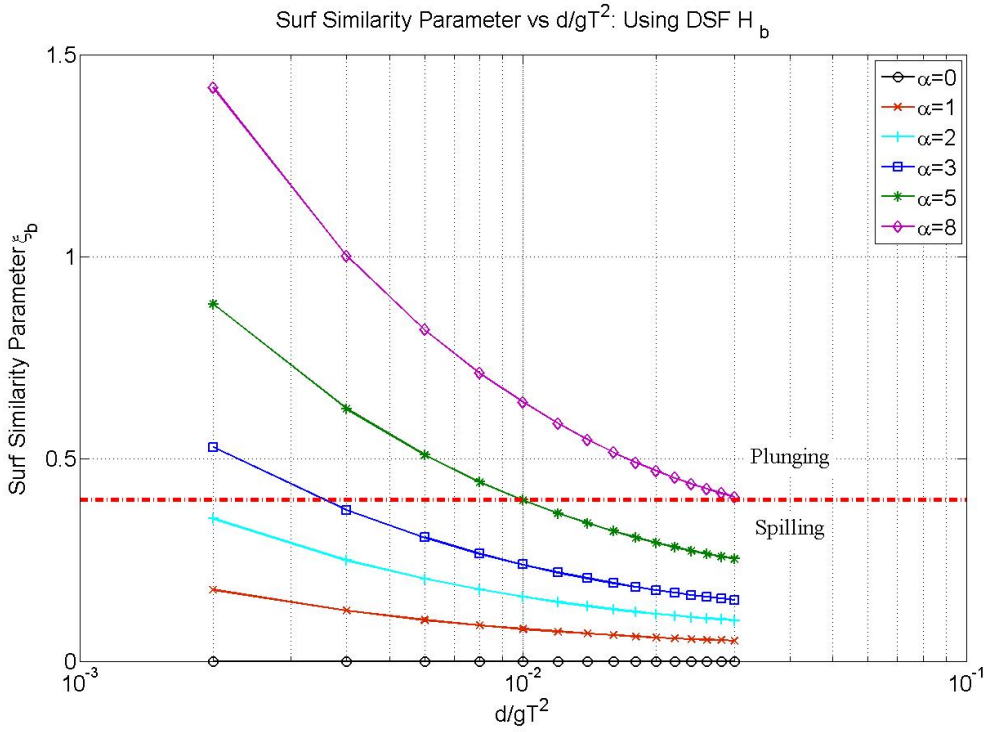

Figure 20 Surf Similarity Parameter for Design Conditions

4.4 Breaking Wave Free Surface Profiles

Determining the free surface profiles of the different wave theories allows for important comparisons to be drawn. The surface profiles that come out of the stream function will be presented first. Figure 21 represents the shallow water example of the design cases. In comparison, Figure 22 represents the most intermediate water wave investigated. Table 11 shows the range of surface crest elevations η_c and surface trough elevations η_t when non-dimensionalized with the breaking wave height. For every water depth investigated this ratio holds. The table also includes the order of solution required for each value of d/gT^2 . Notice that shallower waves have higher crest elevations. The

shallower waves also have steeper crest and longer troughs. Due to their more nonlinear nature, shallow water waves require stream function solutions of higher orders.

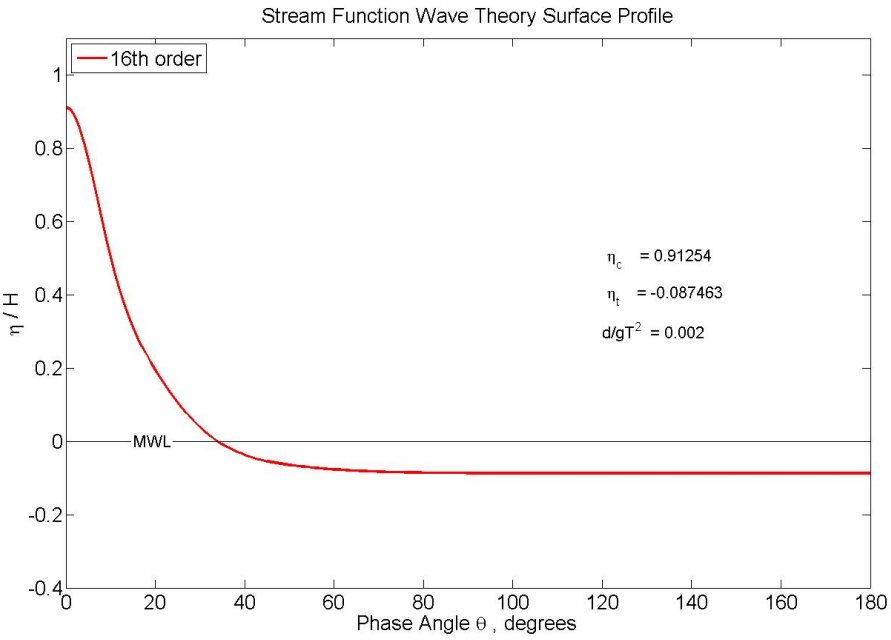

Figure 21 Stream Function Free Surface Profile for $d/gT^2 = 0.002$

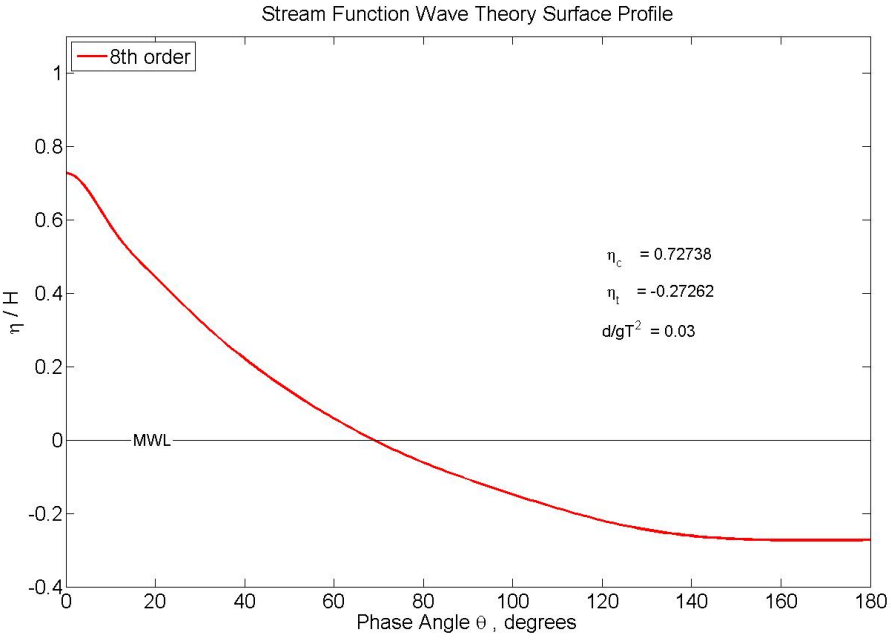

Figure 22 Stream Function Free Surface Profile for $d/gT^2 = 0.03$

Table 11 Stream Function Output Profile Parameters

d/gT^2	η_c/H	η_t/H	Order
0.002	0.913	-0.087	16
0.004	0.878	-0.122	9
0.006	0.855	-0.145	9
0.008	0.837	-0.163	9
0.01	0.823	-0.177	9
0.012	0.809	-0.191	8
0.014	0.796	-0.204	8
0.016	0.784	-0.216	7
0.018	0.772	-0.228	7
0.02	0.762	-0.238	8
0.022	0.753	-0.247	8
0.024	0.745	-0.255	8
0.026	0.738	-0.262	8
0.028	0.732	-0.268	8
0.03	0.727	-0.273	8

The surface profiles that result from linear wave theory are considerably different than the stream function profiles. Following the linear formulation, the profiles are simple cosine curves. The crest and trough elevations are divided equally for each wave height. A side by side comparison of both types of surface profiles is also particularly instructive. Take for example a water depth of 6 meters. Figure 23 demonstrates the difference between both approaches over the full range of wave periods considered. The resulting wave envelopes are compared against a dimensional vertical axis that extends from the seafloor up. The envelopes contain the full range of breaking wave heights possible for this design water depth. While the heights are the same for the linear and stream function theories for each particular instance of d/gT^2 , they take vastly different

forms. The stream function profiles are highly nonlinear, with longer, shallower troughs and higher, steeper crests.

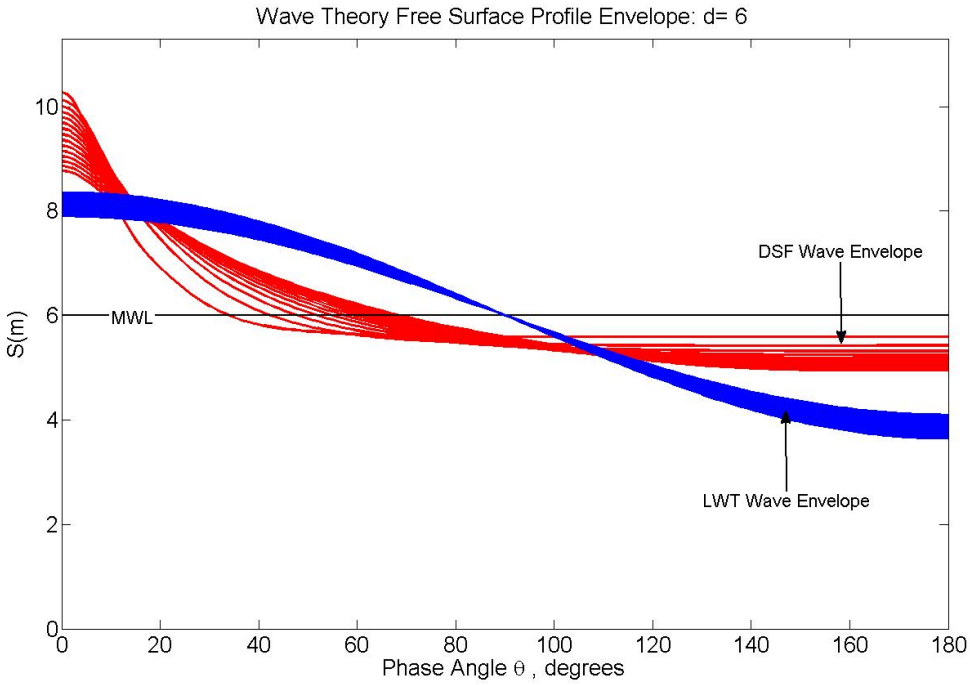

Figure 23 Free Surface Wave Envelope for d=6m

4.5 Breaking Wave Kinematics Comparison

Examining contour plots of the kinematics provides a convenient visual basis for a comparison across the range of water waves considered. The number of possible points available for comparison is limited since stream function kinematics are of interest. The extremes of the shallow and intermediate water waves encompassed in Table 6 are used in this comparison. Again, a water depth of 6 meters is used since it is the only water depth which spans the range of d/gT^2 while maintaining wave periods between 4 and 20 seconds.

Starting with horizontal velocity, Figure 24 and Figure 25 show the shallow water kinematics for Dean's stream function and Wheeler stretching respectively. Both exhibit maximum velocity at a theta of zero degrees. Also, looking at the profiles they are clearly shallow water waves since the velocities within the contours are maintained to the seafloor. The major difference between these two kinematic theories lies in the higher crest of stream function profile. Accounting for the nonlinear nature of the wave results in a considerable concentration of large velocities in the crest. Note that all figures for the kinematics subsection have the same scale of y-axes to ensure convenient comparisons.

Moving to the most intermediate water wave investigated, Figure 26 and Figure 27 shows the horizontal velocity for DSF and Wheeler. The difference between shallow and intermediate waves is considerable. Unlike before, both DSF and Wheeler have a marked decay in horizontal velocity moving from the crest to the seafloor. Knowing the velocity at the seafloor is important for a number of design considerations, most notably determining susceptibility of the pile to scour. Intermediate waves also return smaller non-dimensional velocity values. This fact coupled with a lower ratio of wave period to wave height, indicative of deeper water waves, results in lower actual velocities. For a given design water depth, shallow water waves result in greater overall horizontal velocities with a considerable concentration in the crest when nonlinear wave forms are considered.

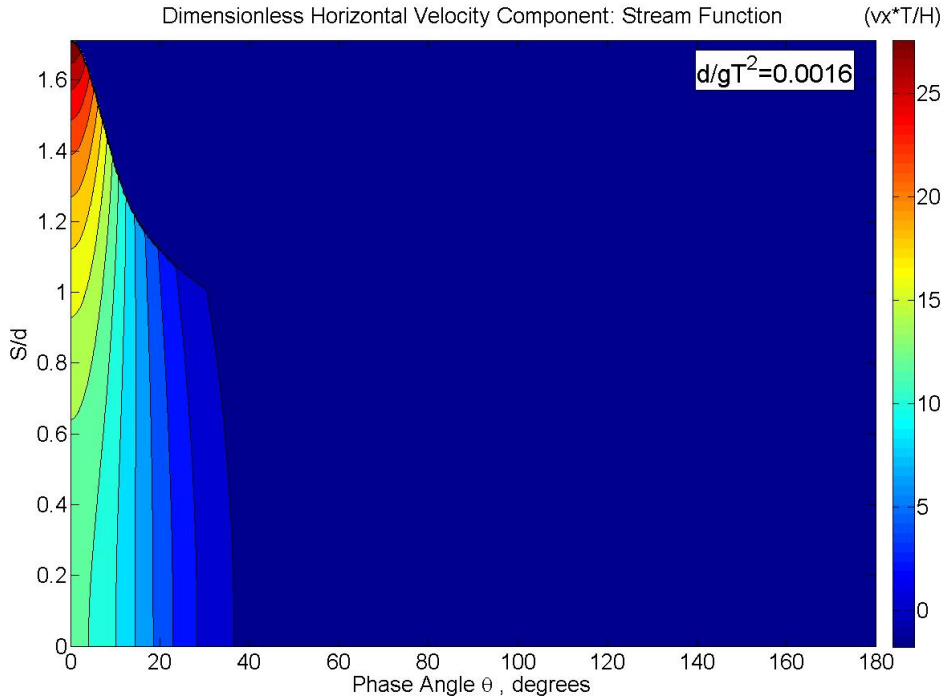

Figure 24 Stream Function Dimensionless Horizontal Velocity: Shallow (d=6m)

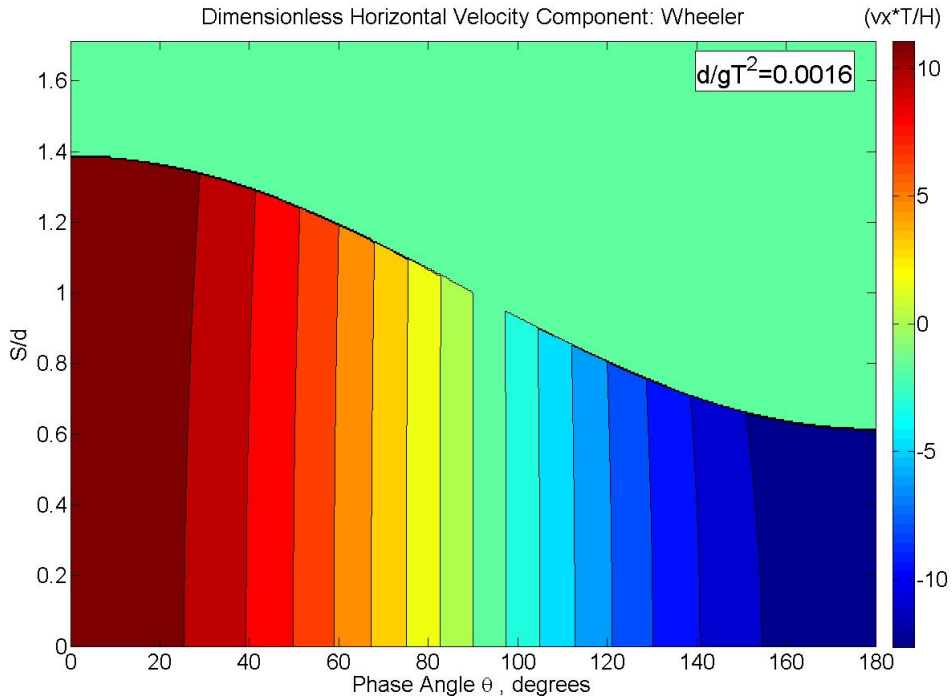

Figure 25 Wheeler Dimensionless Horizontal Velocity: Shallow (d=6m)

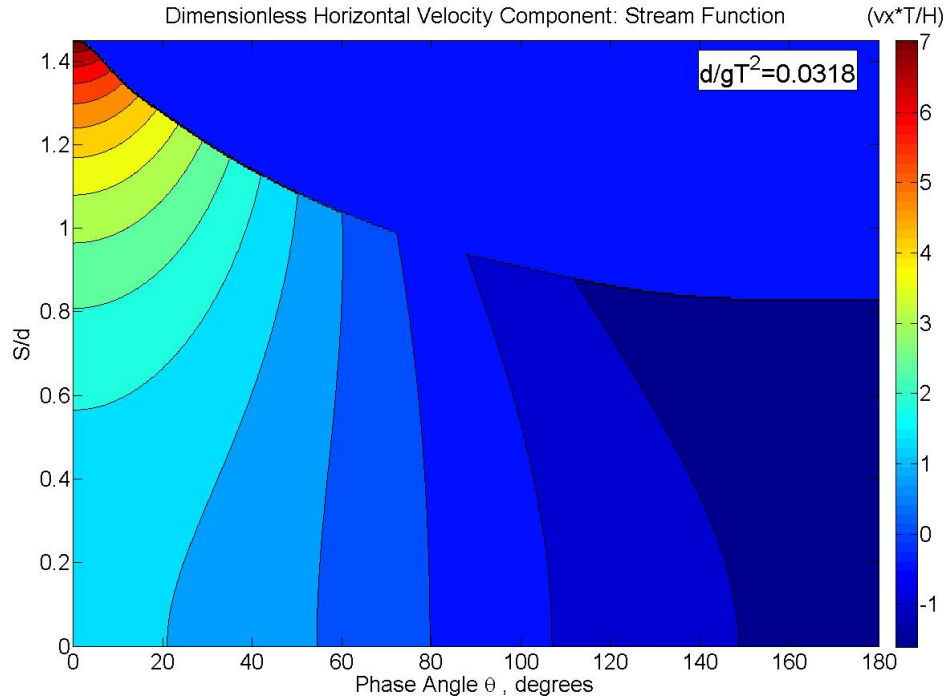

Figure 26 Stream Function Dimensionless Horizontal Velocity: Intermediate (d=6m)

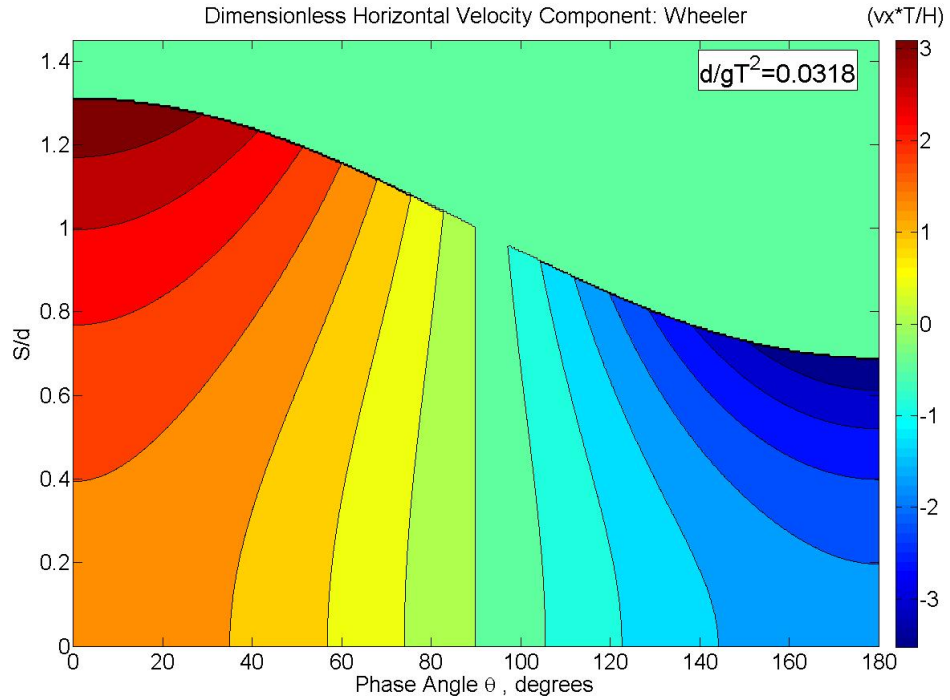

Figure 27 Wheeler Dimensionless Horizontal Velocity: Intermediate (d=6m)

Horizontal velocity is part of the full picture. Horizontal acceleration must also be considered. Figure 28 and Figure 29 display the contour plots of the dimensionless horizontal acceleration for the shallow water example. The difference between DSF and Wheeler in this case is drastic. The acceleration for Wheeler is centered on a theta value of 90 degrees. The contours are also maintained to the seafloor. The plot for DSF shows a shift in the concentration of the acceleration values. A shift to lower values of theta means that the maximum acceleration occurs earlier in the passing of the wave. Also, there is a shift to higher accelerations closer to the free surface. Both DSF and Wheeler have significant accelerations from the free surface to the seafloor.

Looking to intermediate waves, Figure 30 and Figure 31 display the results for DSF and Wheeler respectively. The same general trends present in shallow water are also present here. For Wheeler, the acceleration is centered at a theta value of 90 degrees. The intermediate DSF example also has a shifted maximum to lower theta values, but to a lesser extent than in the shallow water DSF example. Additionally, unlike the shallow examples there is a noticeable decaying trend in the profiles moving from the free surface to the seafloor. While DSF returns a larger overall maximum horizontal acceleration, the values are heavily concentrated near the free surface. Wheeler returns a slightly smaller value, but this large value is not as concentrated and does not decay as quickly as the DSF example. As an illustration of this fact, the acceleration value is higher at the seafloor for Wheeler than DSF. For a given design water depth, the horizontal accelerations are higher for shallow water waves. When

nonlinear wave forms are considered the maximum acceleration is shifted to lower values of theta and heavily concentrated near the free surface.

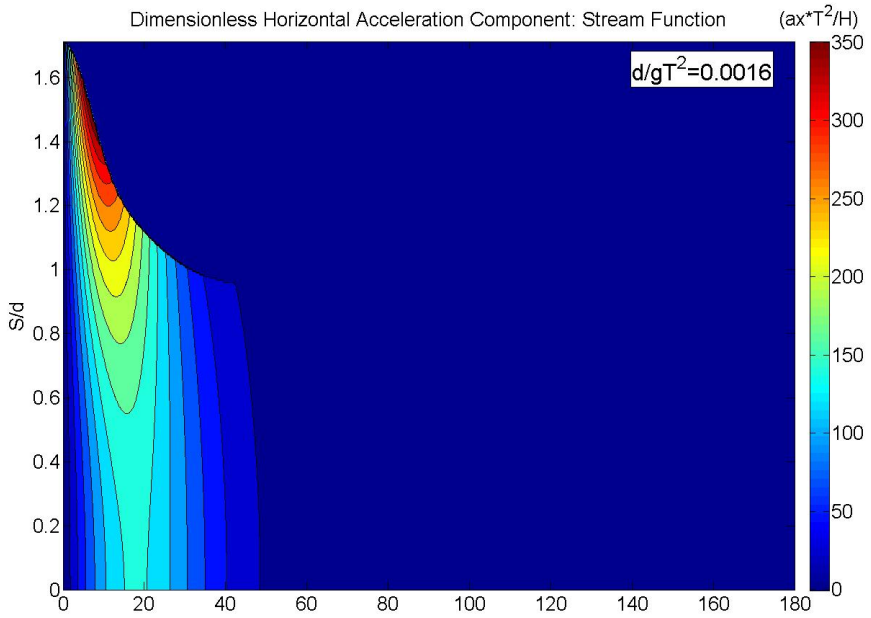

Figure 28 Stream Function Dimensionless Horizontal Acceleration: Shallow (d=6m)

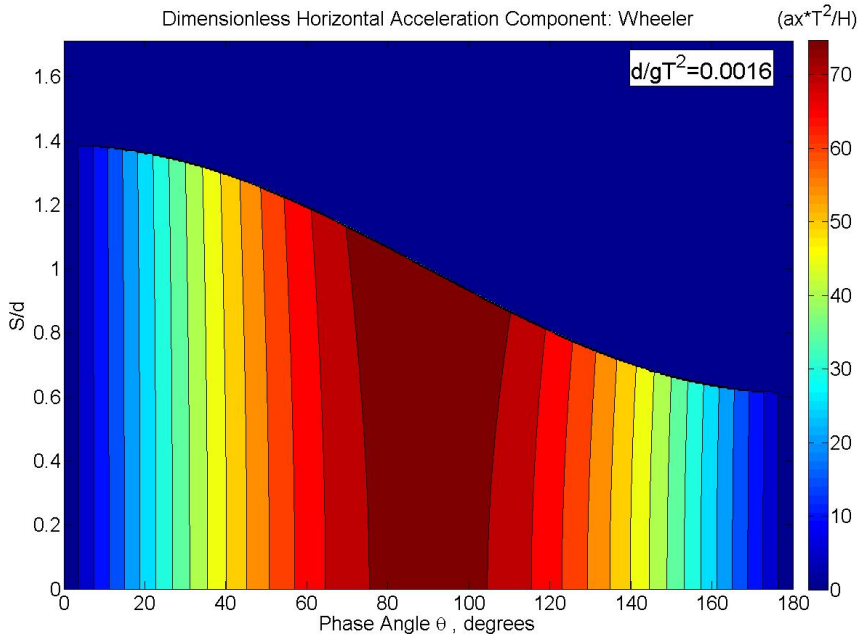

Figure 29 Wheeler Dimensionless Horizontal Acceleration: Shallow (d=6m)

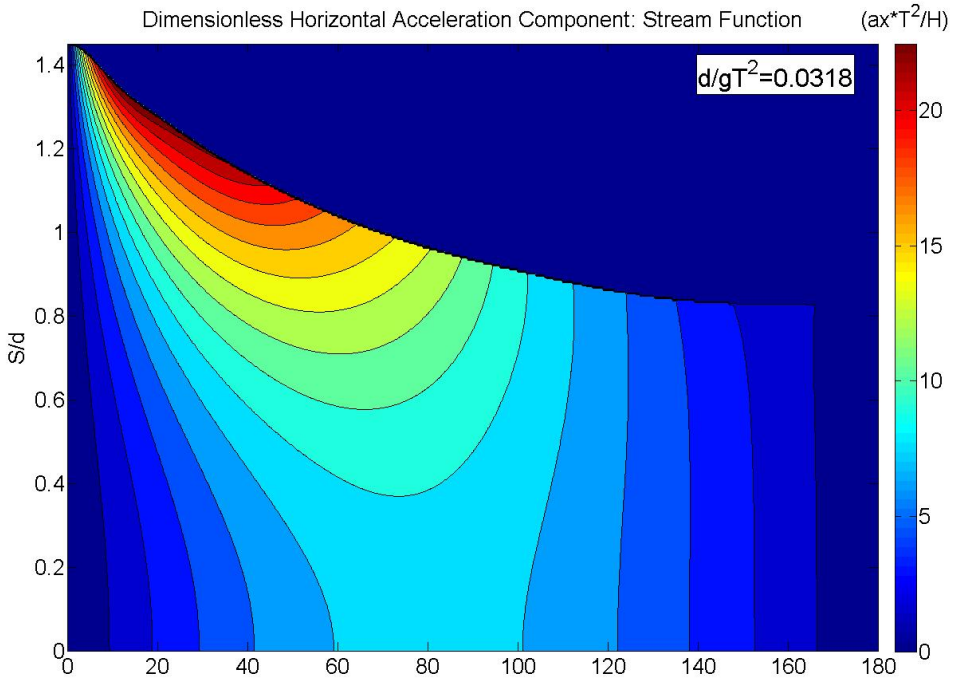

Figure 30 Stream Function Dimensionless Horizontal Acceleration: Intermediate (d=6m)

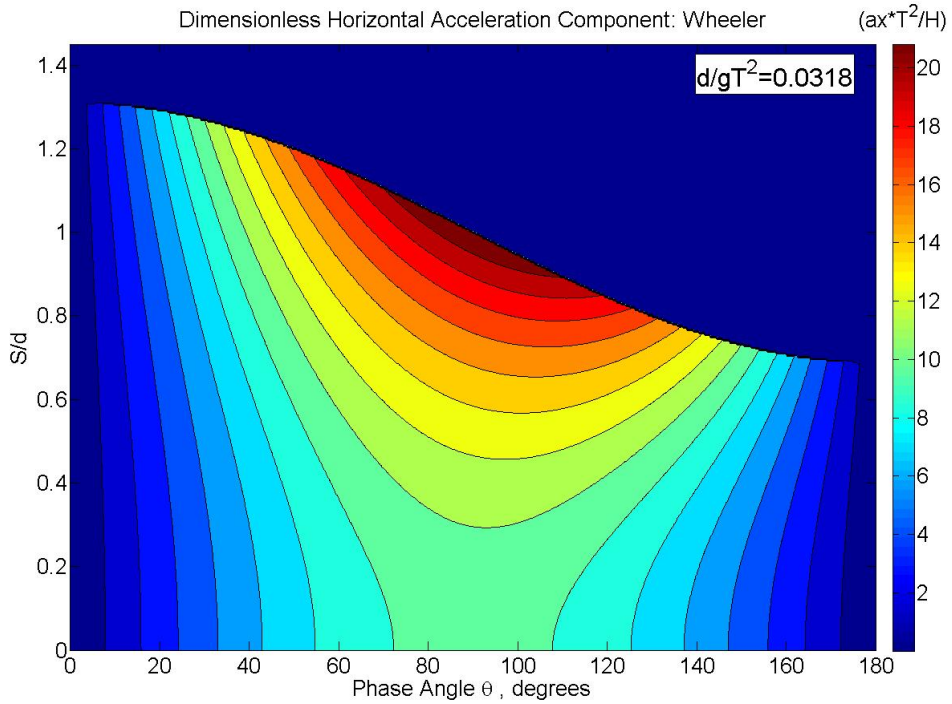

Figure 31 Wheeler Dimensionless Horizontal Acceleration: Intermediate (d=6m)

4.6 Hydrodynamic Force Comparison

The discussion of hydrodynamic force calculations will take a number of forms. In order to provide the greatest potential for comparison, a variety of plots will be used. This is as much a general comparison as it is a demonstration of the process. The final comparisons will utilize a version of a scatter plot in an attempt to present the information in the best way possible. It should be noted that the drag and inertia coefficients used for the Morison equation are those cited by API 2A-WSD. These general coefficients are kept constant throughout the analysis, as they would be in a general design. The values used are for rough cylinders and are $C_D = 1.05$ and $C_M = 1.2$. Also, the water density value used is for seawater, 1025 kg/m^3.

First, a comparison of the force evolution with theta is necessary. This is a general comparison between methods as well as a validation of the programming approach. Figure 32 and Figure 33 show the force profiles of the shallow water example for DSF and Wheeler respectively. The force profiles cited are the fully integrated forces found in equation 2.16. The shallow and intermediate examples are the same used in the previous discussion of kinematics. A diameter of 4.5 meters was used and is held constant for the discussion of force profiles. The drag and inertial components for DSF are much larger, which is to be expected from the kinematics. The maximums for these two components of DSF occur in the same general range as well. This results in a larger combined total force at roughly 4 degrees theta. For the Wheeler method, the drag and inertial components reach maximum values at different times. Consequently, the resulting total force is of a lesser value and occurs later at a theta value of 23 degrees.

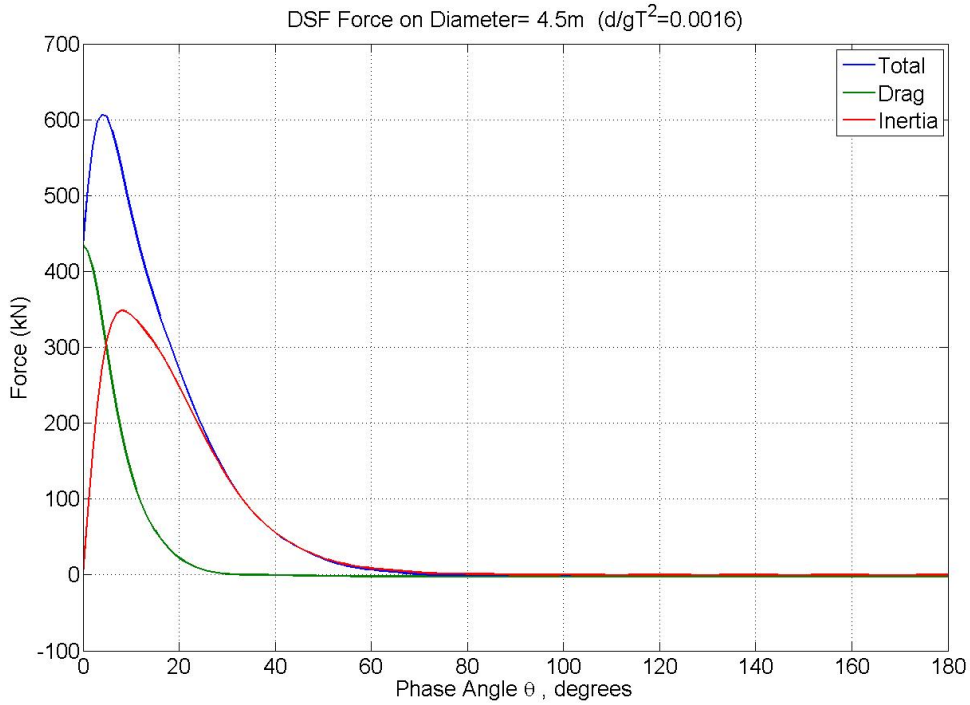

Figure 32 DSF Force Profiles: Shallow Water (D=4.5)

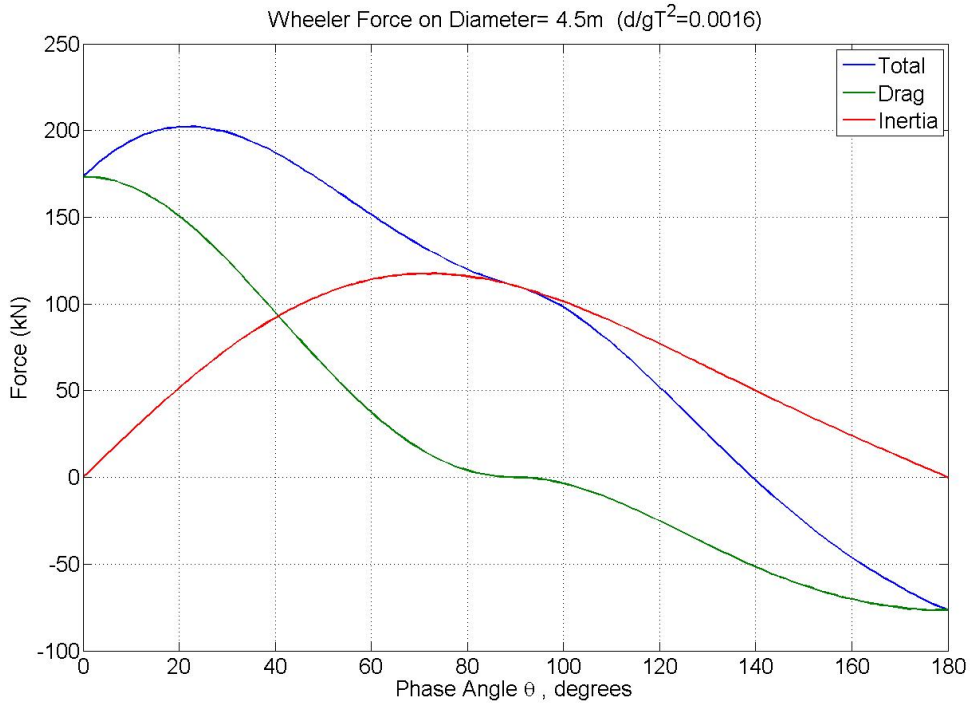

Figure 33 Wheeler Force Profiles: Shallow Water (D=4.5)

The comparison of the intermediate examples provides an interesting result. Figure 34 and Figure 35 display the force profiles for DSF and Wheeler respectively. The drag component for DSF is roughly twice as large as the Wheeler example. But, the total force is dominated by the inertial component in this example. This fact is evidenced by the shift of the max force location to larger theta values for both approaches. The maximum for Wheeler occurs at 69 degrees, while DSF occurs at 26 degrees. The Wheeler method returns a larger inertial force component. It should be remembered that while the maximum acceleration was larger for DSF, it was more concentrated and decayed faster than Wheeler. It is necessary to mention that the Morison equation is applicable in all the examples cited thus far. Stated explicitly, $D/L < 0.2$ holds for this particular set of design parameters. Checking this ratio will be important for later investigations over the full range of design parameters.

A comparison of the force evolution with theta is also necessary for FNV theory. Up until this point FNV theory has not entered into the results discussion. Figure 36 and Figure 37 show the FNV free surface and force profiles for the shallow water and intermediate examples respectively. The subplots of the free surface profiles were displayed in both examples to illustrate the fact that FNV theory uses a linear wave profile. This is somewhat required given its use of wave amplitude as an input parameter. These subplots also show that the range of the wave investigated is the same as the previous methods where the crest is at 0 degrees and the trough is at 180 degrees.

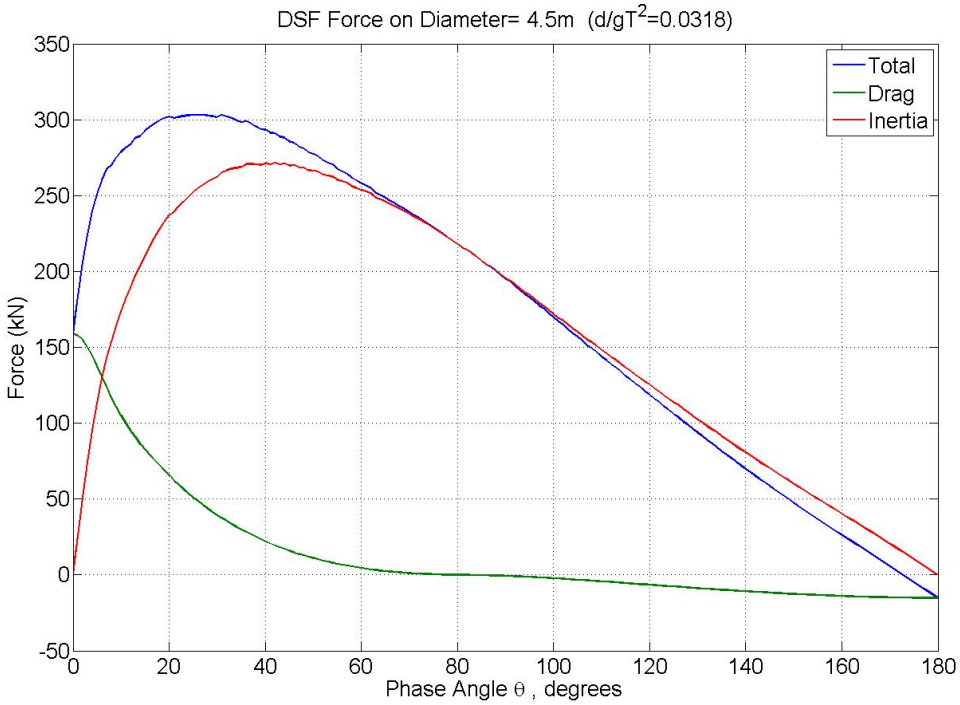

Figure 34 DSF Force Profiles: Intermediate (D=4.5m)

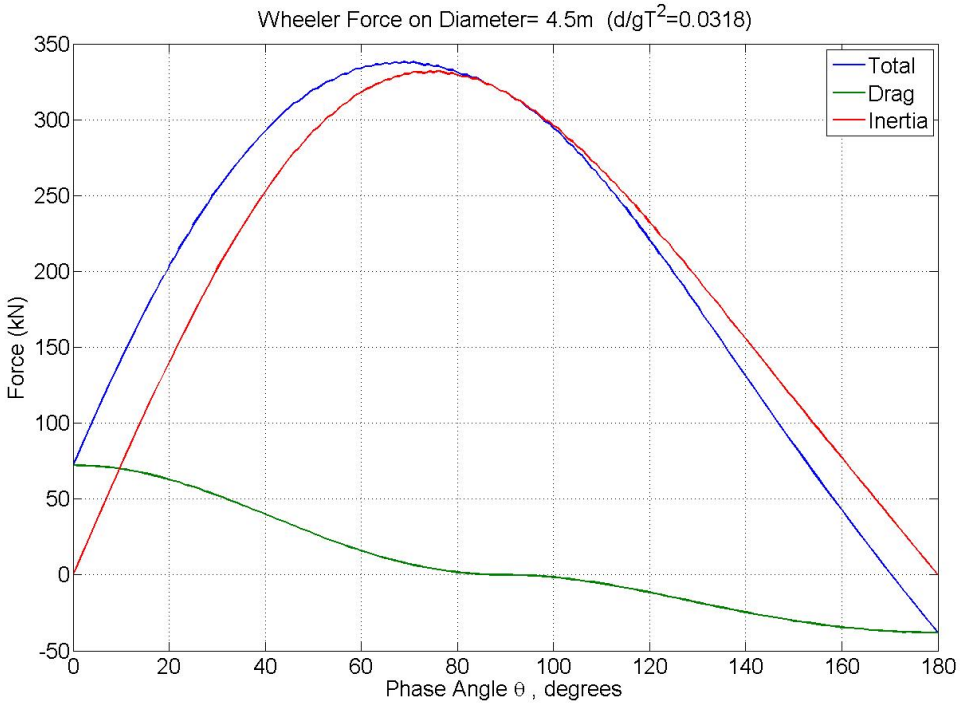

Figure 35 Wheeler Force Profiles: Intermediate (D=4.5m)

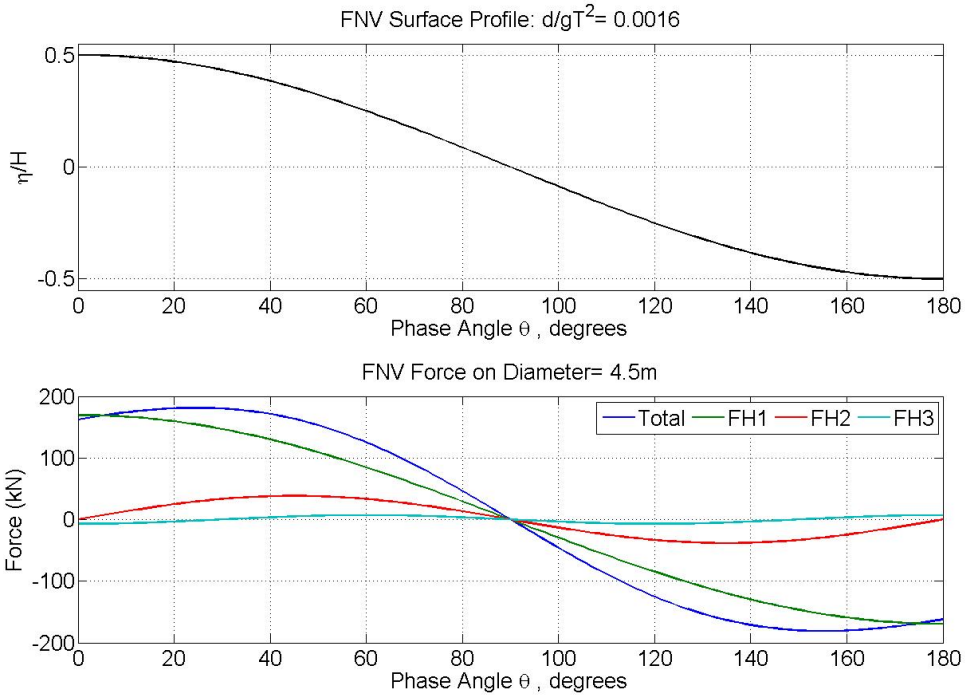

Figure 36 FNV Free Surface and Force Profile: Shallow Water (D=4.5m)

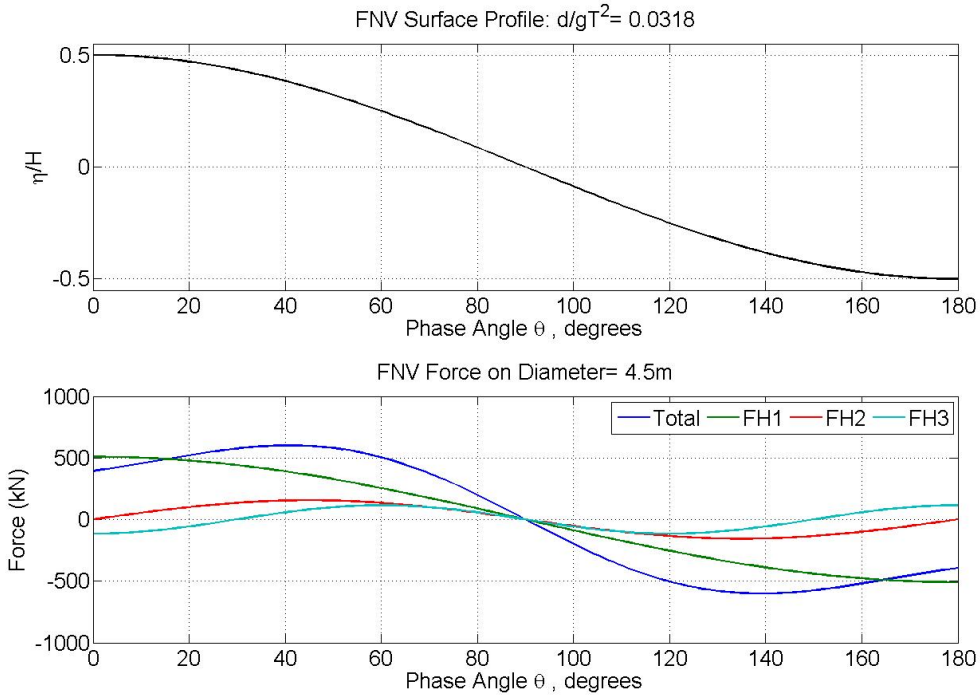

Figure 37 FNV Free Surface and Force Profile: Intermediate Water (D=4.5m)

Comparing the force profiles of the two figures provides additional insight. Note that the max FNV force for this design case in shallow water is less than both DSF and Wheeler. It does occur at roughly the same theta as the Wheeler, 25 degrees. After the initial positive maximum, the FNV force profile reaches considerable negative values after passing a zero value at 90 degrees. The magnitude of negative force values is considerably different from all other methods investigated. For the intermediate wave, FNV theory returns larger force values than both DSF and Wheeler. The maximum location is at 41 degrees, between DSF and Wheeler values. FNV theory has a specific range of wave parameters for which it was derived. These limitations will be explored more fully in analysis to come.

With the basis for establishing maximum forces developed, a comparison between methods is the next step. Unfortunately, due to the difficulties of the stream function program's interpolation between points for the dimensionless stream function coefficients, the comparison for DSF is limited to the 5 points found in Table 6. These 5 points represent the maximum number of comparison points possible within a design depth of 6 meters for the stream function program. There would be even fewer for other depths. Compared to the refined nature of the design cases in Table 10, these 5 points do not provide an accurate representation of the evolution of the breaking waves between the shallow and intermediate limits. For this reason, the comparison of the stream function results will be limited. When exclusively considering a water depth of 6 meters, the 5 points will be plotted alongside the other methods using the more refined design cases.

Before moving to the full comparisons across all design depths an example at a depth of 6 meters is used to establish several important aspects. Figure 38 plots the max force ratio against d/gT^2 and includes all the methods considered at every design diameter. The max force ratio uses the max force of the unstretched linear theory (LWT) as a constant denominator. The different ratios result when the max forces of different methods are swapped out in the numerator. This concept of max force ratio is used in later plots. The denominator and numerators are apt to change so care must be taken to clearly note what is being compared. Also, this figure is one instance where the 5 DSF points are able to be included in the comparison.

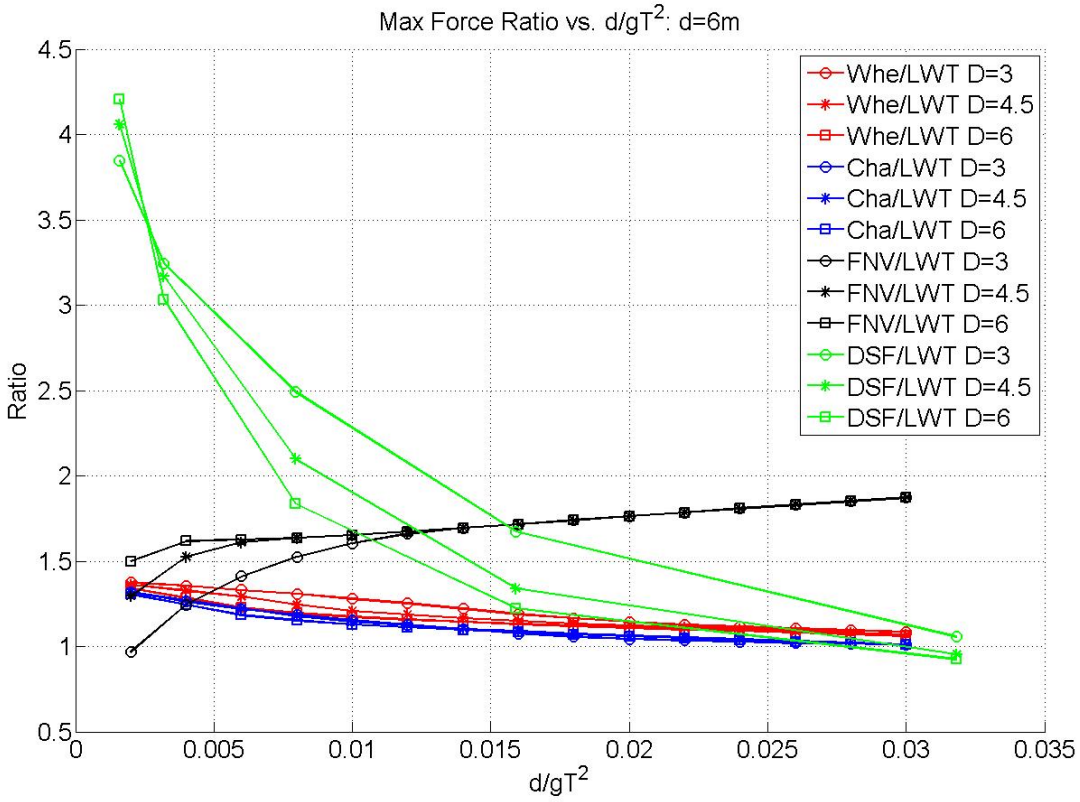

Figure 38 Max Force Ratio vs d/gT^2: Comparison at d=6m

In general, this figure illustrates a number of important facts. In shallow water DSF returns much larger values than any other method. This difference decreases as waves become more intermediate. It is relevant to make a connection to past discussions of DSF kinematics and force profiles. In shallow water, Wheeler and Chakrabarti stretching return slightly larger max force values than LWT. This difference decreases as more intermediate waves are considered. Wheeler returns consistently larger values than Chakrabarti. Looking at the FNV portion, it is clear that for this design water depth it returns very similar results in intermediate water across the range of diameter values. For shallower waters there is a clear divergence from this strong trend present in intermediate waters. Moving from large values of d/gT^2 to smaller values, this divergence occurs first for a diameter of 3 meters and then for 4.5 meters. A more in depth investigation of this divergence for FNV forces will be next.

As outlined in section 2.3, FNV theory was developed with certain assumptions about the ratios between wavelength, wave amplitude, and cylinder radius. The general guidelines of $a/A \approx 1$ and ka << 1 are not clearly defined when the theory is applied to actual numbers. Looking to Figure 38 again, the lines relating to FNV theory diverge at different points. FNV theory for shallower water waves with smaller diameters return smaller max force ratios. Once the lines of varying diameters converge, the difference between diameters no longer exists. Figure 41 shows a similar plot, except it is for FNV theory applied across all design depths. The design diameters of 3.5, 5, and 6.5 meters will now be used. The nature of the divergence is clear in this figure. Deeper design depths diverge at larger values of d/gT^2 . Over this range of cases the design depth of

30 meters never reaches this convergence line. Stated another way, the 30 meter depth breaking wave design cases never converge on what seems to be an upper limit of the max force ratio for a particular value of d/gT^2 . Also, for every design depth the smaller diameters diverge first. Or, the smaller diameters converge last, depending on the viewpoint used.

Determining the point of divergence of each design case will provide a greater understanding of what exactly this divergence means in the larger context of FNV applicability. Determining the exact point of divergence for each case is open to interpretation. Some points are very close to what could be considered the line. Increasing the level of fit required for a point to be considered part of the line decreases the number of points included. Figure 39 is used to qualitatively determine which points to include. Figure 40 uses a scatter plot to display the max force ratios on H_b/D vs. D/L . The boxed points are the points which were chosen as the start of the divergence. This range of points can be considered the boundary between divergent points and points that are part of the line. These boxed points are then averaged to determine a D/L value of 0.054. A more defined quantitative test of the point of divergence could be applied to take the judgment out of this step. With greater refinement between points this more quantitative test might prove more useful. Given the design cases used, the qualitative approach was deemed sufficient.

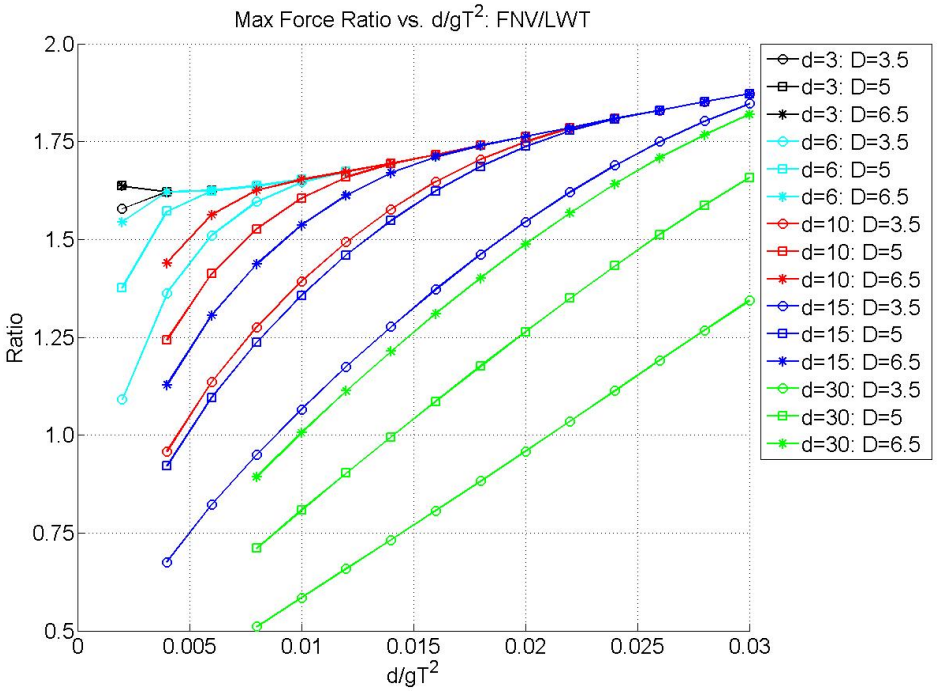

Figure 39 Max Force Ratio vs d/gT2: FNV

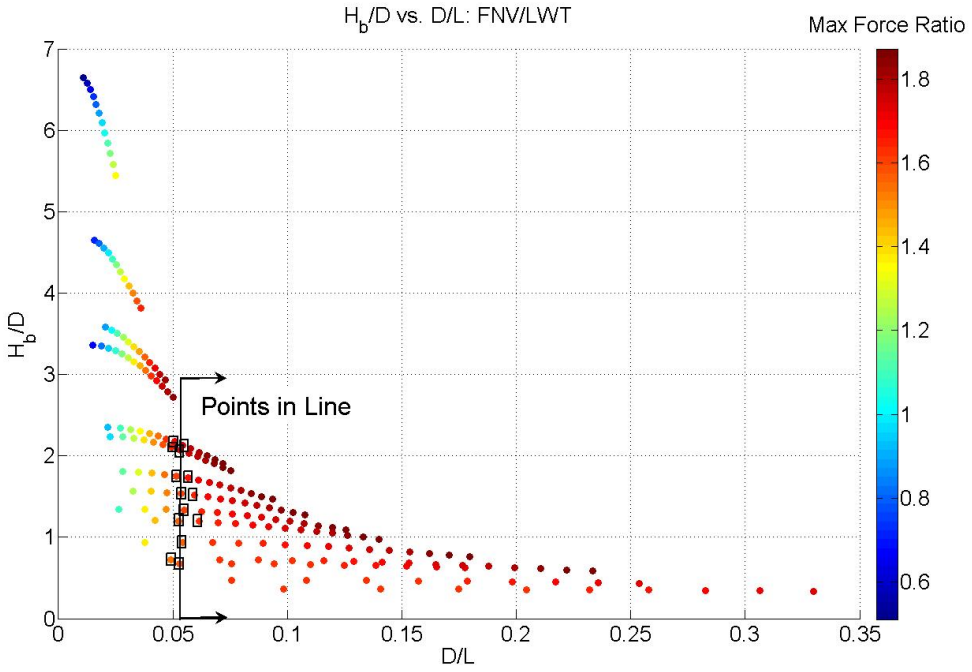

Figure 40 Max Force Ratio Scatter Plot: FNV

A discussion of what exactly this convergence means is necessary. The line in Figure 41 relates to the calculated ka value of 0.054. This line should be thought of as the general region where the points converge/diverge. Simply multiplying this D/L value by pi results in an interesting connection. The point of convergence equals a ka value of around 0.17. Remember, FNV theory requires ka<< 1. For the shallower design water depth of 3 meters, the points on the line have ka values as high as 1.04. Values of ka as high as that are clearly outside the range of the assumptions required by FNV theory. Another requirement of the theory states that $A/a = O(1)$. The y-axis of Figure 40 is this ratio exactly. Figure 41 presents the information in Figure 40 in a manner specific to FNV. The data takes the same form; essentially the axes are relabeled and rescaled. Figure 41 makes the discussion of FNV applicability more straightforward.

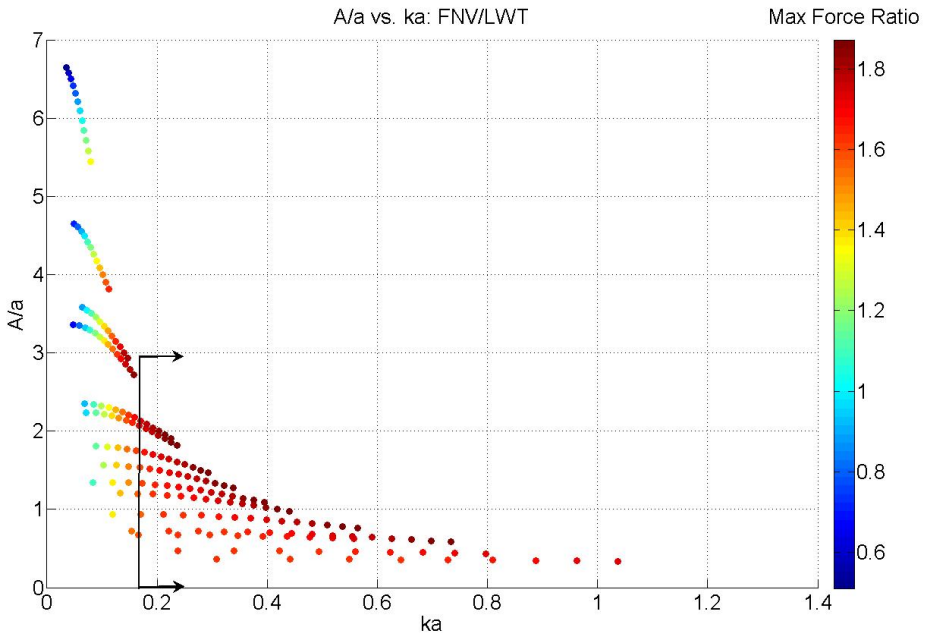

Figure 41 Max Force Ratio Scatter Plot: FNV (A/a vs. ka)

In the end, a definitive conclusion of the general region of FNV applicability is not readily apparent. It has been demonstrated that FNV theory provides results which tend to the same line for all design depths beginning at a D/L ratio between 0.05 and 0.06. The start of this consistency begins at a ka which could be considered to meet the conditions established in the theoretical formulation of FNV. The problem arises with the design cases which fall on this line and also seem to exceed the assumptions of the theoretical formulation. Figure 41 shows an example of this. All three diameters of the 3 meter design case have instances where the ka value approaches or exceeds a value of 1.

Issues also arise when considering the restriction to the ratio of wave amplitude and cylinder radius. The line of convergence is present for A/a values equal to 1. This correlates to design depths around 6 meters as well as for other depths at specific diameters. This line of convergence means that FNV theory consistently returns max force ratio values with the same trend across a wide range of design depths. The beginning of this consistent trend will differ depending on if the design depths range of d/gT^2 includes the line of convergence. The line of convergence is also present for A/a exceeding a value of 2.

The line of convergence does not indicate a region where FNV theory is strictly applicable. On the contrary, values below $D/L = 0.054$ are theoretically better suited for FNV theory. The line of convergence signifies the existence of a consistent positive trend for increasing d/gT^2. Being able to show that the max force ratio increases when waves become more intermediate in regions where FNV is applicable is important. It

makes the case for using FNV theory in more questionable regions easier. In summation, FNV theory provides steadily increasing max force values in comparison to LWT for more intermediate waves with smaller H_b/D.

The use of the type of plot first exhibited with Figure 40 requires some explanation. Knowing exactly which design cases refer to which points will be necessary for future discussions using these scatter plots. Figure 42 provides an explanatory figure to clearly show where the cases fall in the scatter plots. This figure uses D/L for the x axis. When plotting certain information it is better to graph the information using d/gT^2 as the x axis. An explanatory figure for this type of scatter plot is provided in Figure 43. These two explanatory figures should be thought of as kinds of maps when looking at future scatter plots. They provide a straight forward reference for relating design cases to scatter points. It is important to remember what is changing when progressing across a line of singular water depth and diameter in these scatter plots. The independent variable that is changing in this case is wave period. But, in future scatter plots relating to Figure 42 it is manifested as wave length. This information relates directly to the design cases laid out in Table 10.

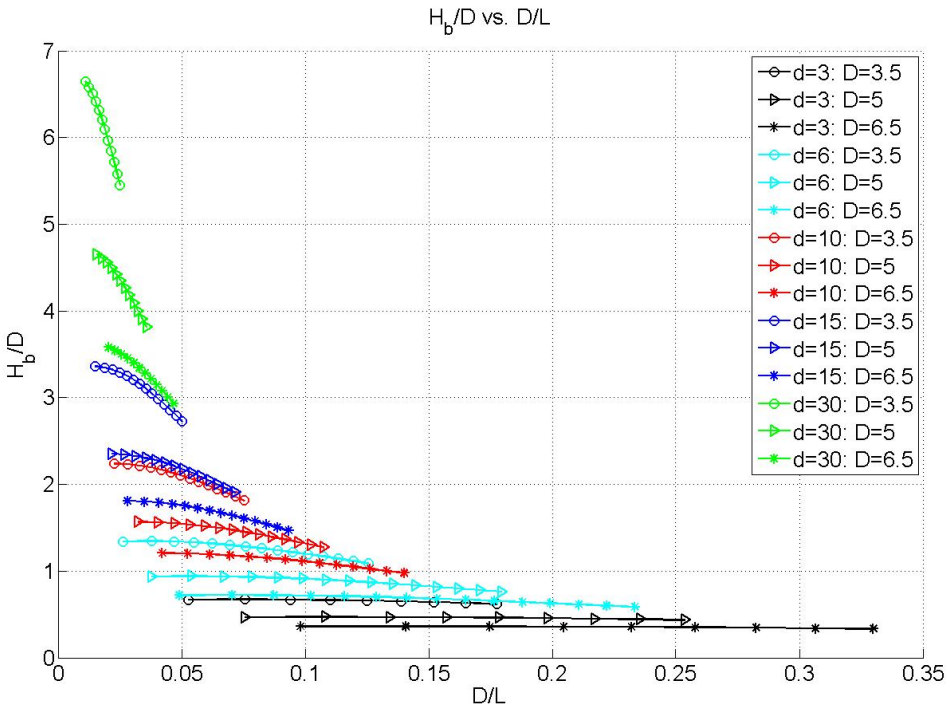

Figure 42 Scatter Plot Explanation: H_b/D vs. D/L

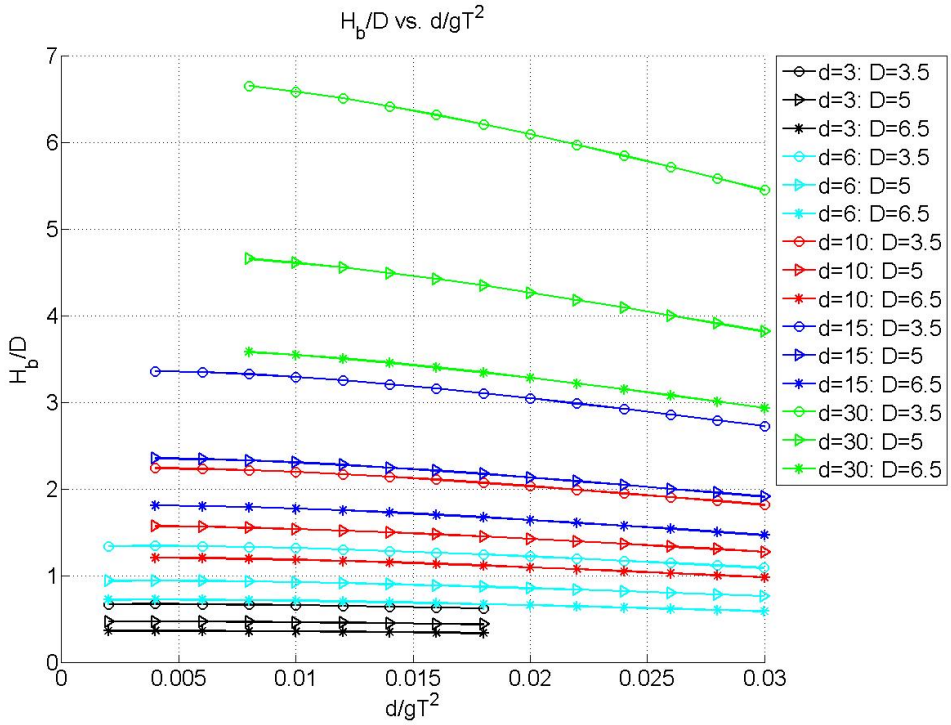

Figure 43 Scatter Plot Explanation: H_b/D vs. d/gT^2

Note that there are three areas with varying degrees of overlap between cases. The design cases relating to a depth of 10 meters overlap with certain diameters of both 15 and 6 meters. This is a result of the closeness of the ratios between breaking wave heights and diameters chosen for investigation. This overlap could have been avoided by choosing a smaller range of diameters or design depths that were further apart. When considering things like max force ratios, this overlap will not be a problem since the ratios will be close to the same for both cases. If anything, the overlap provides a good check for the reliability of drawing conclusions over a wide range of design variables from plots of this nature. The overlap does pose a problem when values are dimensional. For instance, if the FNV force was plotted with a scatter plot there will be inconsistencies at the overlap since the dimensional forces are not the same across different diameters and water depths. That being said, a scatter plot of all the design cases for dimensional values does provide a general sense of the progression from shallow to intermediate waves and from large diameters to small diameters.

The discussion can now focus on comparisons across the whole range of design cases. The difference between Wheeler stretching and unstretched linear wave theory will be presented first. Figure 44 is the scatter plot of the max force ratio using d/gT^2. This figure clearly shows that as the design wave becomes shallower (decreasing d/gT^2) the Wheeler method returns larger maximum forces than LWT. This trend is consistent for all design water depth. Holding the value of d/gT^2 constant also shows that for larger ratios of H_b/D Wheeler returns larger maximum forces than LWT. To

explain it another way, use an intermediate water wave at d=30 meters as an example. Now, holding diameter constant results in a larger breaking wave height for increasing ratios of H_b/D. In the case of larger breaking wave heights, the plot shows that Wheeler will return larger maximum forces than LWT. Approaching the problem from the other angle provides additional insight. Using the same example, holding the breaking wave height constant results in a smaller diameter for increasing ratios of H_b/D. For the case of smaller diameters, the plot shows that Wheeler method returns larger maximum forces than LWT. Stated inversely, the difference between max forces for Wheeler and LWT is less when considering larger diameter monopiles.

The comparison of Chakrabarti stretching to LWT also provides some interesting insights. Figure 45 shows the scatter plot for max force ratio between Chakrabarti and LWT. As with the previous Wheeler comparison, the general trend of shallower waves returning larger max force ratios is also present. This trend holds true for all design water depths and diameters. But unlike Wheeler stretching, holding a constant d/gT^2 and increasing H_b/D does not result in larger max force ratios. In most instances the max force ratio appears to be held constant. In fact, looking specifically at a water depth of 3 meters it appears to decrease. So, for Chakrabarti there is little if any change in the max force ratio when d/gT^2 is held constant and diameter is increased. For intermediate waves there is very little difference between the max force of Chakrabarti and LWT over all the design water depths and diameters. The max force ratio gradually increases almost uniformly across all H_b/D ratios as the water waves become shallower.

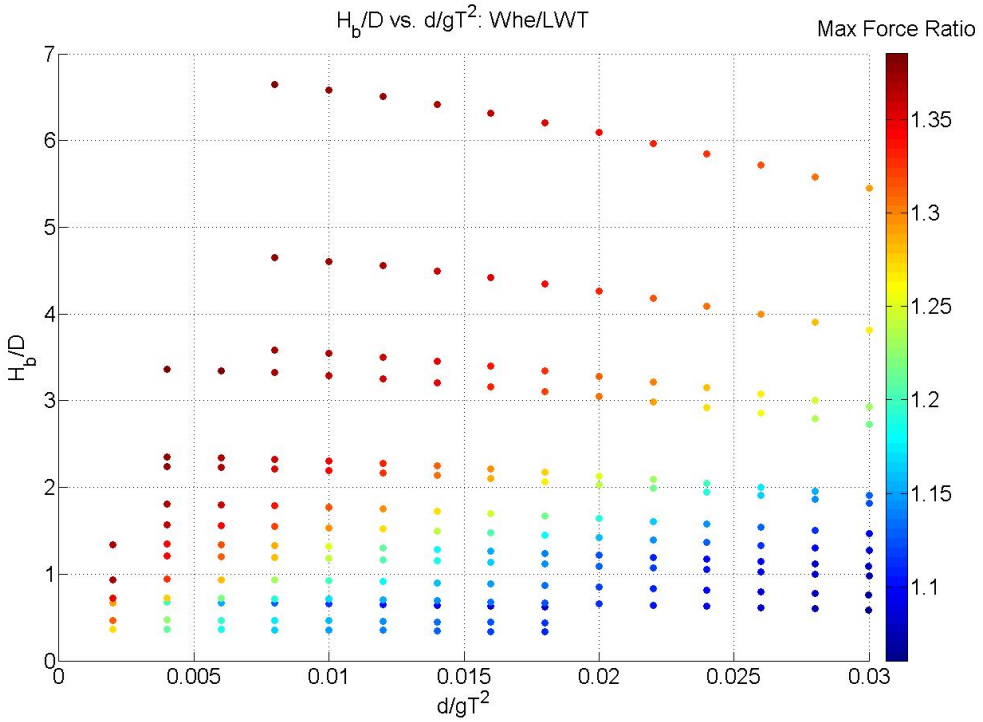

Figure 44 Max Force Ratio Scatter Plot (d/gT^2): Whe/LWT

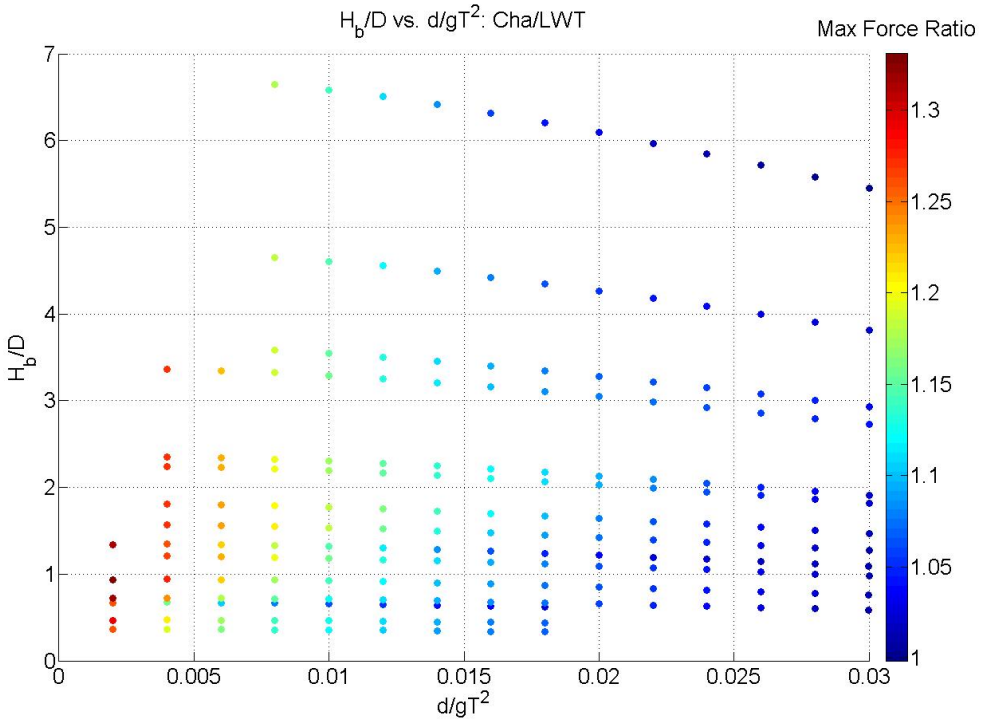

Figure 45 Max Force Ratio Scatter Plot (d/gT^2): Cha/LWT

The comparison between Wheeler and Chakrabarti stretching is necessary to establish the differences between the max force output of these two methods without comparing them to LWT. Figure 46 shows the scatter plot of the max force ratio where Wheeler is the numerator and Chakrabarti is the denominator. For the shallower water depths of 3 and 6 meters there is very little difference between the two methods. This holds over the entire range of d/gT^2. Moving to deeper water depths Wheeler starts to return larger max force values than Chakrabarti. So, Wheeler consistently returns max force values equal to or larger than Chakrabarti for all design cases considered. The difference between the two methods is particularly noticeable for more intermediate water waves in deeper design water depths.

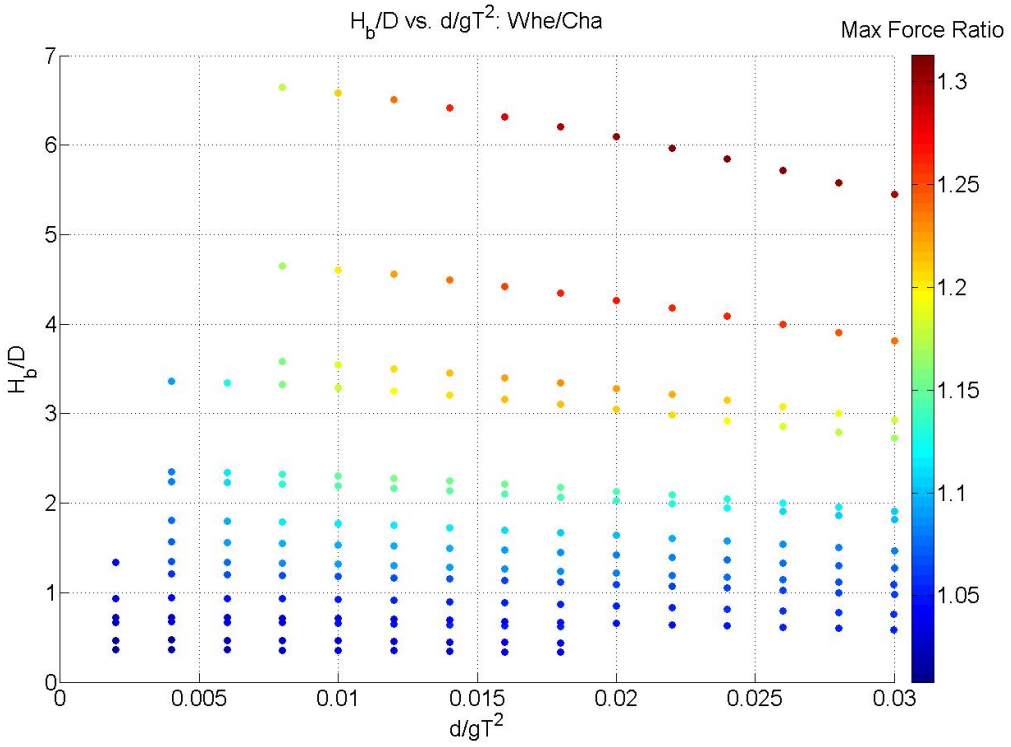

Figure 46 Max Force Ratio Scatter Plot (d/gT2): Whe/Cha

The max force scatter plot of FNV and LWT was previously presented; a more in depth discussion concerning the applicability of FNV and the other methods is merited at this time. Figure 47 is a max force scatter plot comparing FNV with Wheeler stretching. Wheeler stretching was chosen for this comparison because it is the closest to FNV theory for linear methods. A line with arrows indicating the region of convergence is contrasted with a similar demarcation indicating the region of the Morison equation validity. In the region of FNV convergence it is clear that FNV theory returns larger max force ratios. Outside of this region the results have a greater range of values. For a design water depth of 30 meters the max force values of Wheeler are almost entirely larger than FNV. As waves become more intermediate the max force ratio increases. For shallow water waves outside of the applicable region for FNV theory, especially in deeper water depths, Wheeler returns larger max force values than FNV theory.

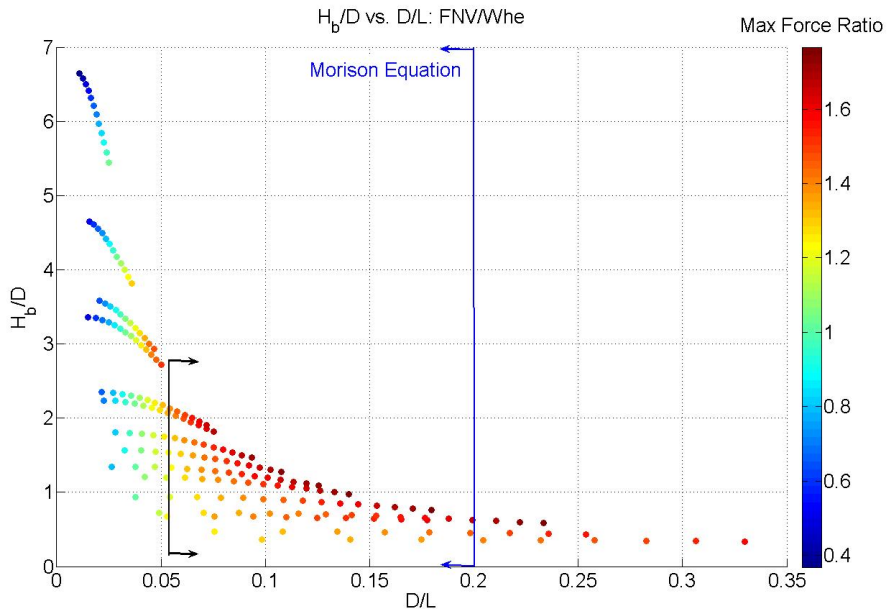

Figure 47 Max Force Ratio Scatter Plot (d/gT2): FNV/Whe

There are a number of aspects at play in this comparison. First, the applicability of the Morison equation is important. Even if the Wheeler method returned larger max force values up to $D/L = 0.2$, diffraction effects would have to be considered once this point was reached. Another important aspect to consider is the applicable range of Wheeler as well as other linear wave kinematics. The discussion surrounding the kinematics contour plots and the differences between DSF and Wheeler kinematics is pertinent here. So as not to get into a discussion of which approach is correct, the comparison between FNV and Wheeler takes precedence. In the region where FNV theory provides consistent results and is deemed to be applicable, it consistently returns larger max force values that all the other linear theories considered.

In an attempt to include stream function theory into the discussion, a comparison against all the methods will be conducted. Remember that the stream function program analysis is restricted to the points found in Table 6. Given the limited number of points available for investigation the resulting scatter plots are patchy and prove ineffective for comparison. Consequently, a simpler plot was used so that the general trend line between points could at least be approximated. Figure 48 shows the plot of the max force ratios versus D/L for all the methods being considered. The diameters used in this comparison are the ones outlined in section 3. Annotations have been added to the plot to aid in determining the regions of method applicability. The colors for each relate to the same lines added to Figure 47.

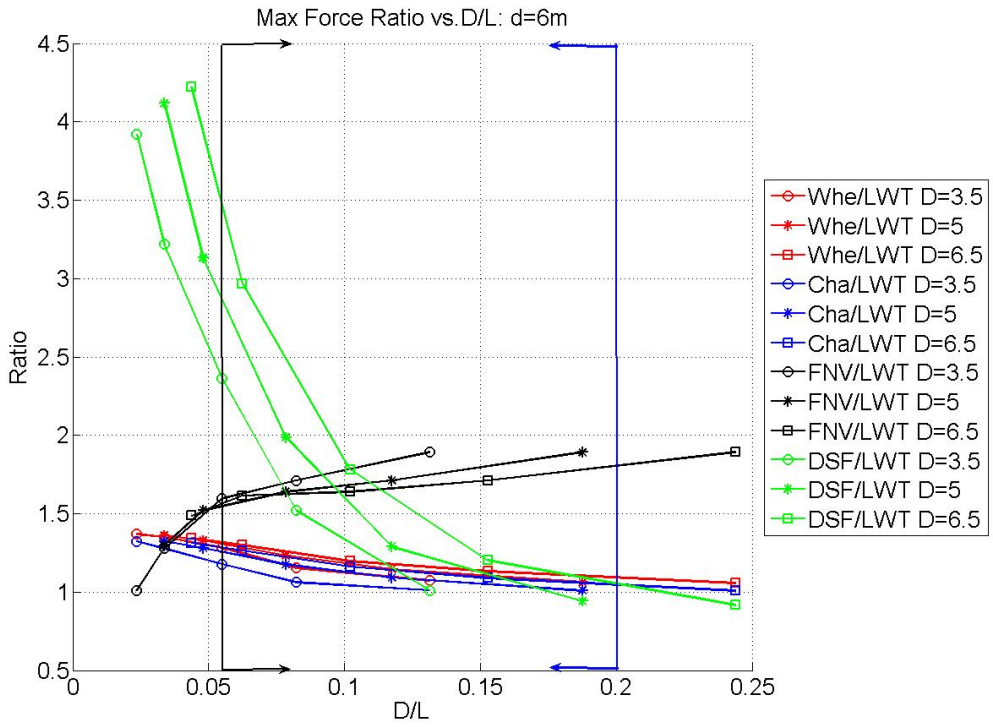

Figure 48 Max Force Ratio vs D/L: (d=6m) All Methods

There are several important conclusions which can be drawn from this figure. First, DSF returns significantly larger max force ratios than the other methods for shallow water waves at a depth of 6 meters. As the relative depth increases the max force ratio of DSF decreases. Stream function theory reaches max force ratios of similar magnitude to Chakrabarti and Wheeler stretching at more intermediate water waves. Also, there are portions of FNV consistency where DSF returns larger max force ratios. This stands in stark contrast to both stretching methods which were consistently smaller than FNV over this range of D/L. DSF ratios are larger than FNV ratios over a larger range of D/L when diameter is increased. In general terms, DSF returns considerably larger max force ratios for shallow water waves. While DSF returns larger max force

ratios than FNV for a small range of relative depths, the point where FNV ratios exceed those of DSF is well below the Morison equation applicability limit of $D/L = 0.2$.

So far the discussion has revolved around the ratio between methods. Using the scatter plots to investigate the dimensional qualities of each method is also useful. Figure 49, Figure 50, and Figure 51 display the scatter plots of the dimensional max force for the Wheeler method at 3, 15, and 30 meters respectively. Three figures were required in order to provide the necessary resolution in the point colors. Apart from giving a general sense of the difference in scale of max force values between the three water depths, other conclusions can be drawn from a comparison. Looking at the scatter plot for a depth of 3 meter water, it is clear that shallower water waves result in smaller max force values for a given diameter. Also, it goes without saying that larger diameters return larger max force values.

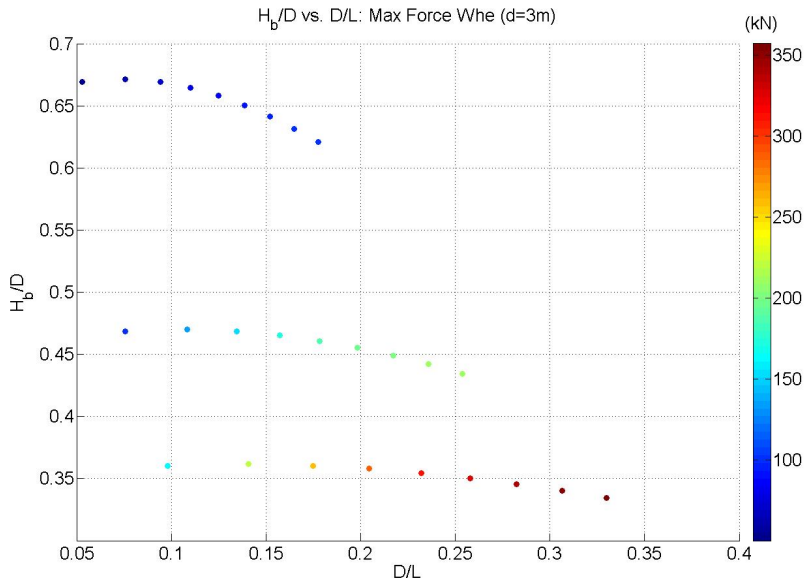

Figure 49 Dimensional Max Force Scatter Plot: Whe (d=3m)

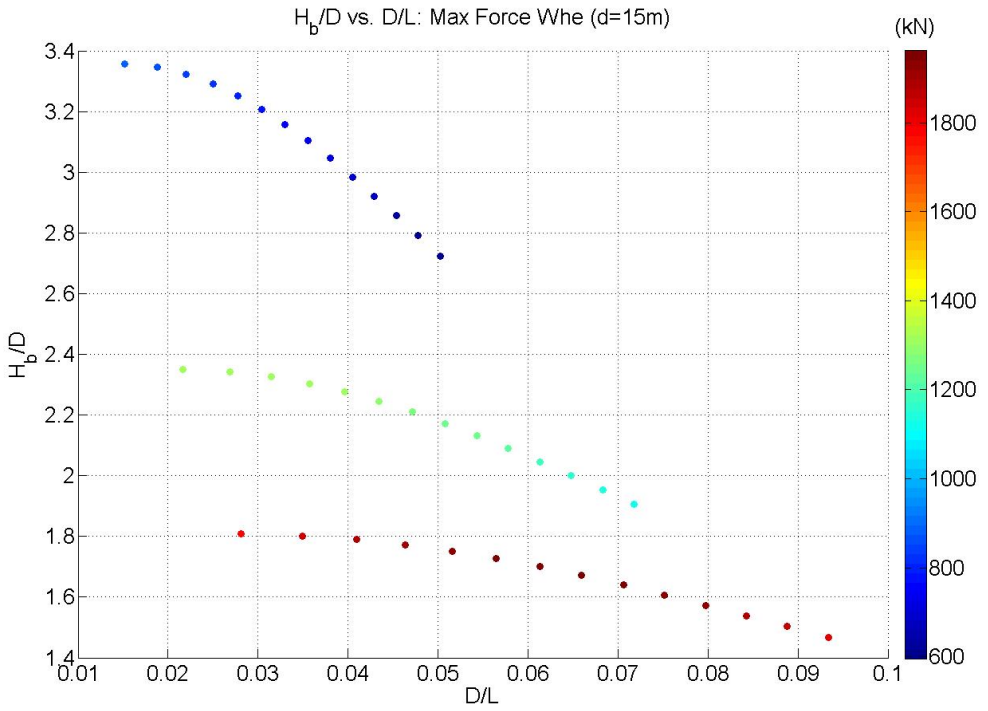

Figure 50 Dimensional Max Force Scatter Plot: Whe (d=15m)

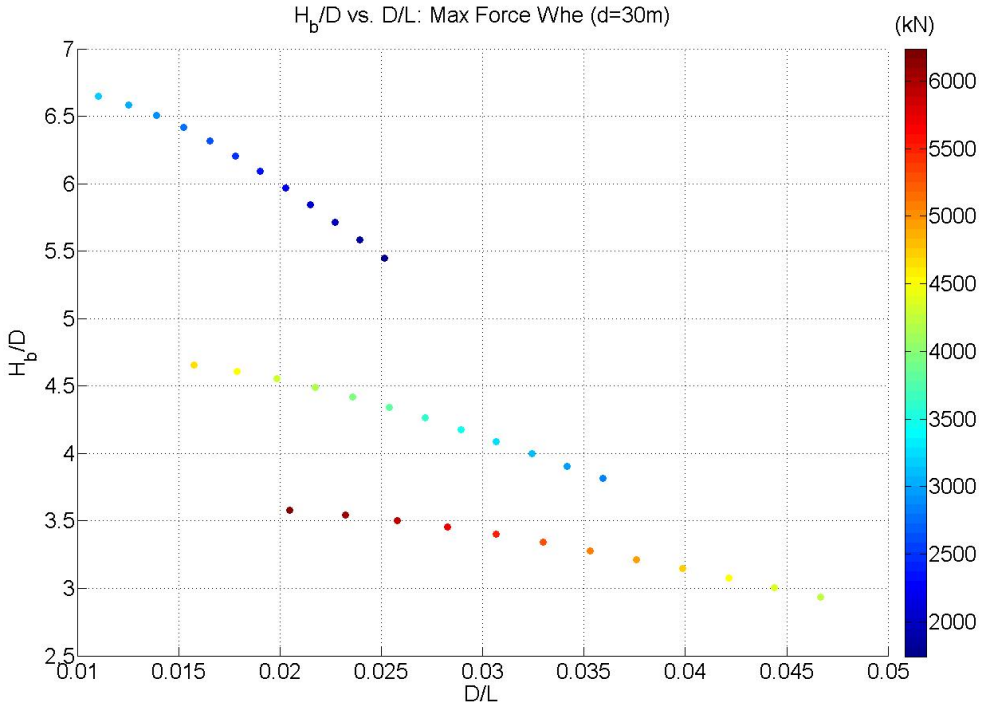

Figure 51 Dimensional Max Force Scatter Plot: Whe (d=30m)

These trends begin to shift when looking to the scatter plot for a depth of 15 meters. It still stands that larger diameters return larger max force values. But, starting with this water depth the shallower water waves return larger max force values. This is opposite of what is the case for shallower water depths. This transition is visible in the line of lowest H_b/D in Figure 50. This line corresponds to a diameter of 6.5 meters. For this case there is a clear transition of the maximum value from the right to the left in that the largest value for this particular line is located at middle values of the range of D/L values.

For a water depth of 30 meters the transition of the largest maximum force from intermediate to shallow water waves is complete. Figure 51 clearly shows that the largest max force now occurs for the shallow water design case. This is a complete reversal of what was the case for shallower design water depths. This overall shift in the location of the max force from intermediate water to shallow water for increasing water depths is present in all three of the linear wave methodologies. Consequently, a more in depth investigation of the components which make up the max force is necessary.

The ratio of force components that make up the max force value changes depending on the relative role the kinematic components play at the time of max forcing. Figure 52 presents a scatter plot of the ratio between the inertial force and the combined max force. The numerator is the value of the inertial force at the particular theta location of the maximum force. The denominator is the dimensional max force used in the previous figures. This ratio multiplied by 100 can be thought of as a percentage of the contribution of the inertial force to the total maximum force for a given design case. A

similar scatter plot for the contribution of the drag force was generated. As expected, it was a mirror image of the inertial contribution such that the addition of both plots equaled one. The figure makes use of the three water depths used in the preceding dimensional force discussion. Using these three water depths ensured that there was no overlap in the scatter points between depths.

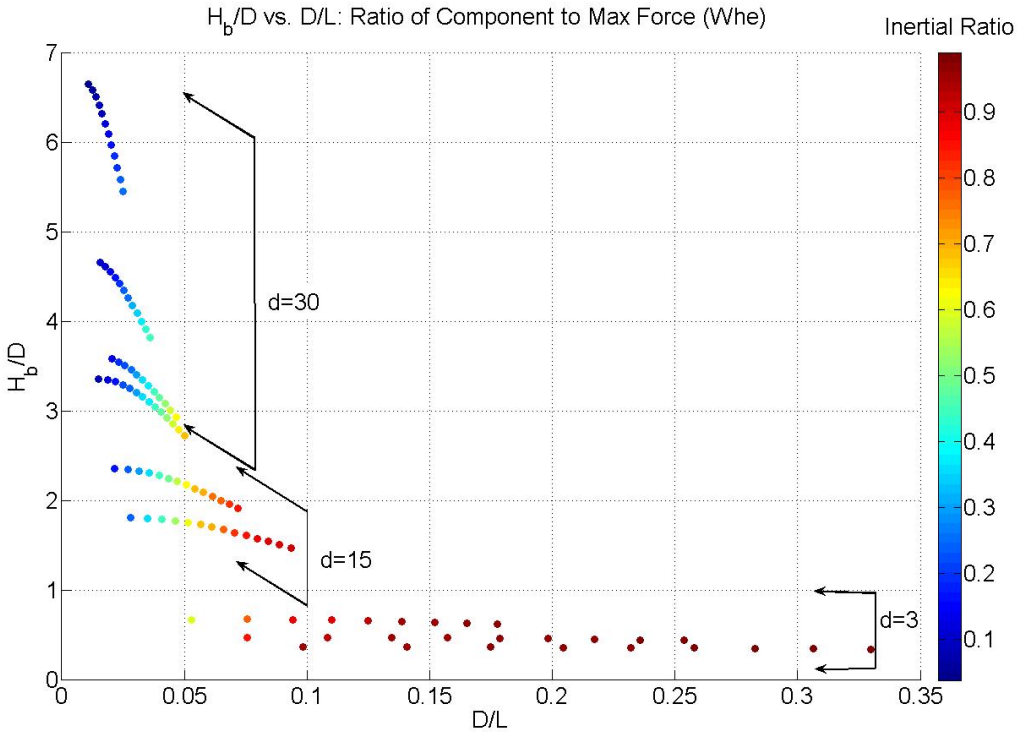

Figure 52 Max Force Component Ratio Scatter Plot: Whe

Figure 52 demonstrates that for the shallower water depths the inertial component dominates the total force contributions. For the range of design cases investigated, the shallow water depths relate to relatively small values of H_b/D and a large range of D/L values. As the water depth increases, the max force shifts away from

being dominated by inertial contributions to more drag dominated cases. The larger diameters of 6.5 and 4 meters for the 15 meter water depth case show the full range of both drag and inertial contributions. At the 15 meter design water depth the intermediate water waves are inertia dominated while the shallow water waves are drag dominated.

It is interesting to note that FNV theory returns larger max force ratios for more intermediate water waves as well. This result mirrors the inertia dominated cases investigated for the linear methods. But, unlike the linear methods this trend holds across all design depths. It is true even for the 30 meter case, which was shown to be entirely drag dominated by the linear methods. This fact, along with considerations of FNV applicability might be why FNV returns max force ratios less than 1 in these drag dominated areas. Note that the line of convergence occurs between inertia ratios of 0.6 to 0.7 for Wheeler in Figure 52. This result makes sense considering the formulation of FNV theory is based in diffraction analysis. Similar to simpler diffraction approaches, the higher order approach of FNV neglects the drag component of the force and assumes the inertial force dominates.

The previous discussion provides insight into the makeup of the max total force; but, it does not provide information on the relative size of the maximums for each force component. Figure 53 shows the scatter plot of the percent difference between the max drag and max inertia. The percent difference is calculated by first subtracting the max drag component from the max inertial component, then dividing by the average of the two values. It provides a sense of the general size of the components relative to each other. The inertia and drag components used in this comparison are not tied to a

particular theta as was the case in Figure 52. For a water depth of 3 meters the percent difference takes large positive values. This means that the inertial component is significantly larger than the drag component. The opposite is true for a water depth of 30 meters. Here the percent difference is large and negative. In this case the max drag components are significantly larger than the max inertial components.

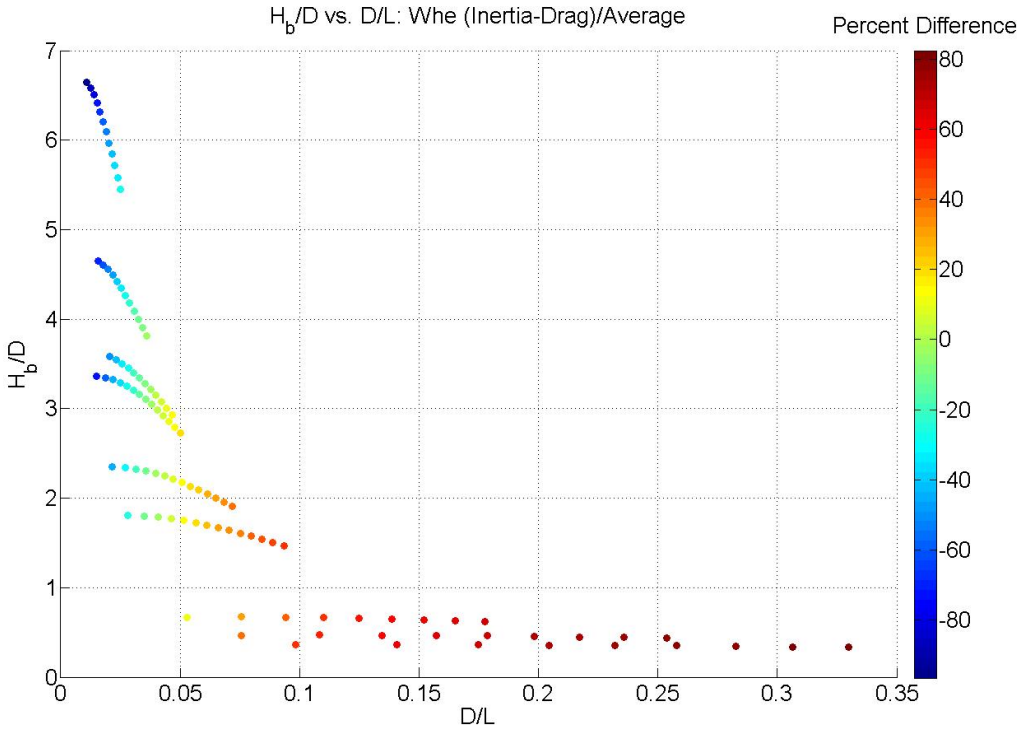

Figure 53 Max Component Percent Difference Scatter Plot: Whe (Drag/Inertia)

Looking at both Figure 52 and Figure 53 provides a number of different conclusions concerning the reason behind the shift in location of the max force from intermediate to shallow water waves for increasing water depths. It is clear that for areas where one particular component is significantly larger than the other, the contribution of

that component to the max force is larger as well. Also, when the maximums of both components are roughly the same, as established in Figure 53, it indicates a transition between the max force for a design depth being located in either shallow or intermediate water waves. In Figure 53, at a water depth of 15 meters and a diameter of 6.5 meters, the location of the zero percent difference is also the location of the transition in Figure 50.

4.7 Hydrodynamic Moment Comparison

The moments follow directly from the forces outlined in the previous section of results. Plots of the moment profiles will not be included. Force profile plots were included as a check of the program as much as for comparative purposes. Moments stemming from forces calculated with the Morison equation were determined using contributions from both the drag component and the inertial component. Consequently, there are different moment arms for both the drag component and inertial component of the moment. The majority of this section will make use of the scatter plot figures first presented in the force section. It is necessary to note that the moments in this section were taken about the seafloor.

Before moving directly to the scatter plots, an issue with the FNV moment equation must be discussed. For shallower water waves at breaking heights the equation returns completely unintelligible results. The moments starting out are negative, which makes no sense considering the FNV force is positive for theta values of zero. Examples of the types of profiles that come out of the FNV moment equation are presented here.

Figure 54 shows the results from shallower water waves and the reason why they are deemed incorrect. The problem is that the total moment starts out negative. Figure 55 shows the progression to deeper water waves and represents results that are more reasonable given the FNV forcing inputs. Comparing these two figures it is clear that the total force is negative at zero degrees as a result of the contributions of both the first harmonic and the third harmonic. The second and fourth harmonics do not play an immediate role at a theta of zero degrees because they are sine functions and will always be zero at this theta. It is not enough to say that the first harmonic must be positive. Since the third harmonic is always negative by definition, the combination of these two harmonics at the initial theta value must be greater than or equal to zero. Refer back to equations 2.29 through 2.33 for the equations relevant to this discussion.

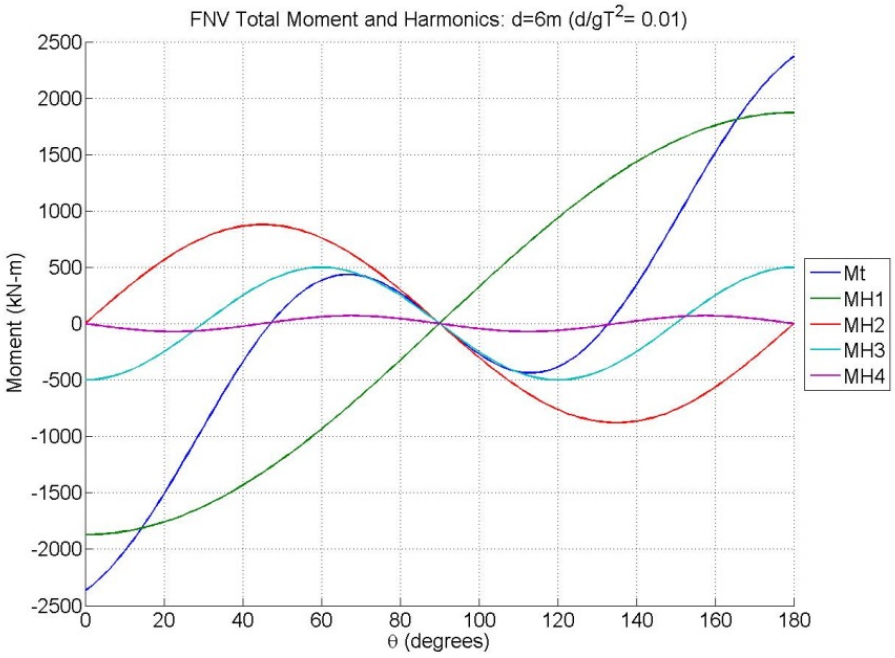

Figure 54 FNV Total Moment and Harmonics Profiles ($d/gT^2 = 0.01$)

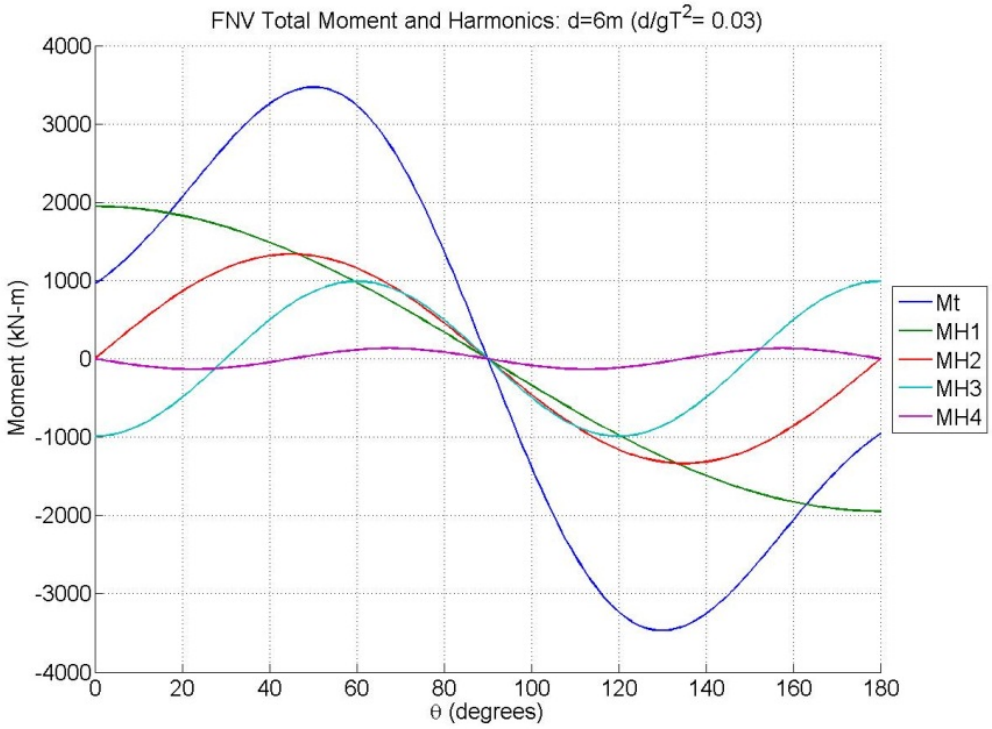

Figure 55 FNV Total Moment and Harmonics Profiles ($d/gT^2 = 0.03$)

Working out the inequality established in the previous paragraph provides a starting point for determining the limits of applicability to the FNV moment equation. The sum of the coefficients from the first and third harmonics must be greater than or equal to zero. It follows that equation 4.4 is true.

$$\left(2\pi\rho g a^2 A(d - \frac{1}{k} + e^{-kd}) + \frac{1}{2}\pi\rho g k a^2 A^3 + d\pi\rho g k^2 a^2 A^3\right) \geq \left(\frac{1}{2}\pi\rho g k a^2 A^3 + 2d\pi\rho g k^2 a^2 A^3\right) \tag{4.4}$$

This can be further simplified to the final result presented in equation 4.5.

$$A^2 \leq \frac{2\left(d - \frac{1}{k} + e^{-kd}\right)}{dk^2} \tag{4.5}$$

Equation 4.5 is not meant to be the strictest limitation on the applicable range of the FNV moment equation. It is rooted in a simple observation of the relationship between harmonics. It results from an even simpler requirement that the total moment at a theta value of zero must not be a negative value. It does provide the lower limit at which FNV results will begin to make sense.

The inequality does provide some interesting insights on the nature of the possible problems with the FNV moment equation. The inequality is basically stating that the size of the wave must be smaller than some combination of design parameters such as water depth and wave length (wave period). Therefore, it makes sense that shallower breaking waves would not satisfy even this simplest inequality. Remember that shallower breaking waves have larger wave heights than intermediate breaking waves.

Looking at the inequality another way connects this discussion with the original limitations made to the ratios of wavelength, cylinder diameter and wave amplitude. Equation 4.5 can be reorganized to make the connection to these parameters clear. This new way of approaching the problem is displayed in equation 4.6.

$$(kA)^2 \le \frac{2\left(d - \frac{1}{k} + e^{-kd}\right)}{d} \tag{4.6}$$

The 64 design cases are cycled through and the point at which the initial total moment consistently equaled zero was noted. The relevant information of this analysis is presented in Table 12. Note that the results presented are for the 3.5 meter diameter case. Analysis was performed on the other design diameters. There is not a row for a depth of

3 meters because it never achieved consistently positive moment results. Apart from different dimensional moment values, the exact same numbers are generated across all diameters. This is reasonable considering the moment would change.

Table 12 Point of First Acceptable FNV Moment

d (m)	dgt2	M_{HT} (kN)	kA	kA^2	$\frac{2\left(d-\frac{1}{k}+e^{-kd}\right)}{d}$
6	0.02	42	0.364	0.132	0.166
10	0.022	297	0.380	0.144	0.232
15	0.022	498	0.380	0.144	0.210
30	0.022	1315	0.380	0.144	0.187

There are several important conclusions which can be made from this. The fact that the same results were generated across all diameters leads one to reason that diameter does not play a role in determining if the moments will be positive. Also, the fact that the same range of values for kA shows up for each design depth is noteworthy. This clearly demonstrates that there is a constant lower limit to the FNV moment equation. A more accurate estimation of this lower limit could be achieved with greater refinement between d/gT^2 steps. That being said, the values of d/gT^2 at this lower limit are clearly in more intermediate waters. As mentioned in the previous paragraph, this translates into wave heights that are smaller, which fits with equation 4.5. The inequality used in this analysis proves to be a decent indicator of the point at which the non-dimensional parameter kA must reach for the FNV moment equation to provide reasonable results.

In order to continue on with the moment analysis for all approaches, a method of determining a moment that could be considered representative of FNV forces needs to be determined. Since Wheeler stretching provides the largest inertial forces of all the linear methods it was chosen as a reasonable moment arm substitute. The inertial component was chosen because, as described and shown previously, FNV theory only considers inertial effects. The moment arm for this process was determined by dividing the inertial moment component by the inertial force component. This procedure results in a moment arm about the seafloor. Since both the moment and force are functions of theta the resulting inertial moment is also a function of theta. This moment arm is then multiplied by the FNV force. The result is considered a modified FNV moment.

The analysis on the level of fit of these two methods was completed in an attempt to show that the modified FNV moment is a reasonable approach to consider. Figure 56 shows a comparison of moment profiles for a selected design case. This particular design case was chosen because it is an example of where the FNV moment is applicable. The plot compares this original FNV moment profile against the three other profiles. The three other profiles include FNV force with Wheeler inertial moment arm, FNV force with LWT inertial moment arm, and the normal Wheeler moment profile. It is clear that the Wheeler moment arm with FNV force results in moment profiles that most closely approximate the original FNV moment equation. Comparing LWT and Wheeler, it is clear that the crest stretching of Wheeler results in a better fit in this situation. The normal Wheeler moment profile was included to show that even though two of the

profiles share components of the same moment arm the effect of force is significant in determining moment profile.

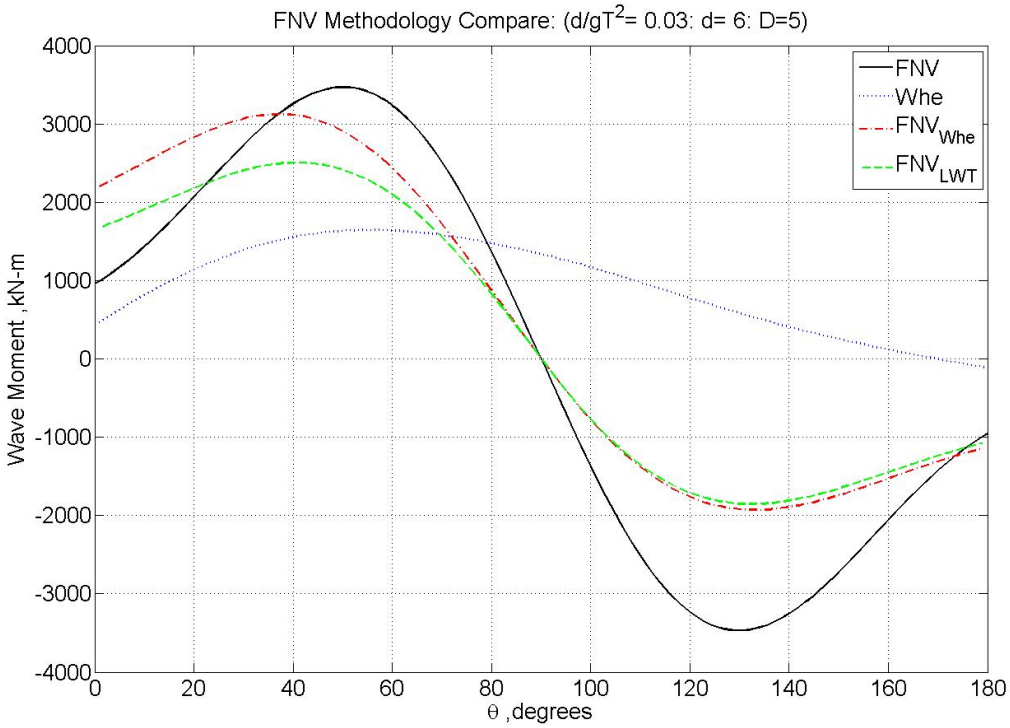

Figure 56 Modified FNV Moment Methodology: Moment Profiles

A comparison across the entire range of acceptable FNV moment cases follows. This comparison consists of a scatter plot of max moment ratios. The denominator used is the max moment of the original FNV moment equation. The numerator is the max moment from the modified FNV moment approach using the inertial moment arm from Wheeler stretching. The resulting scatter plot over all the design diameters is displayed in Figure 57. The limited number of points is a result of the partial number of acceptable original FNV moments. Out of the 64 design case points for each diameter, only 21 had

acceptable moment plots. A discussion of the trends across d/gT^2 and H_b/D is possible. But that is not the point of this figure. This figure is meant to show the relatively close fit that the modified FNV method provides across the range of design cases available for investigation. The ratios are very close to one which implies the values are very similar. Considering the issues encountered with the original FNV moment equation when applied to shallow water breaking waves, this modified approach provides a reasonable solution. From this point on, the term FNV moment will refer to the modified FNV moment with Wheeler moment arm.

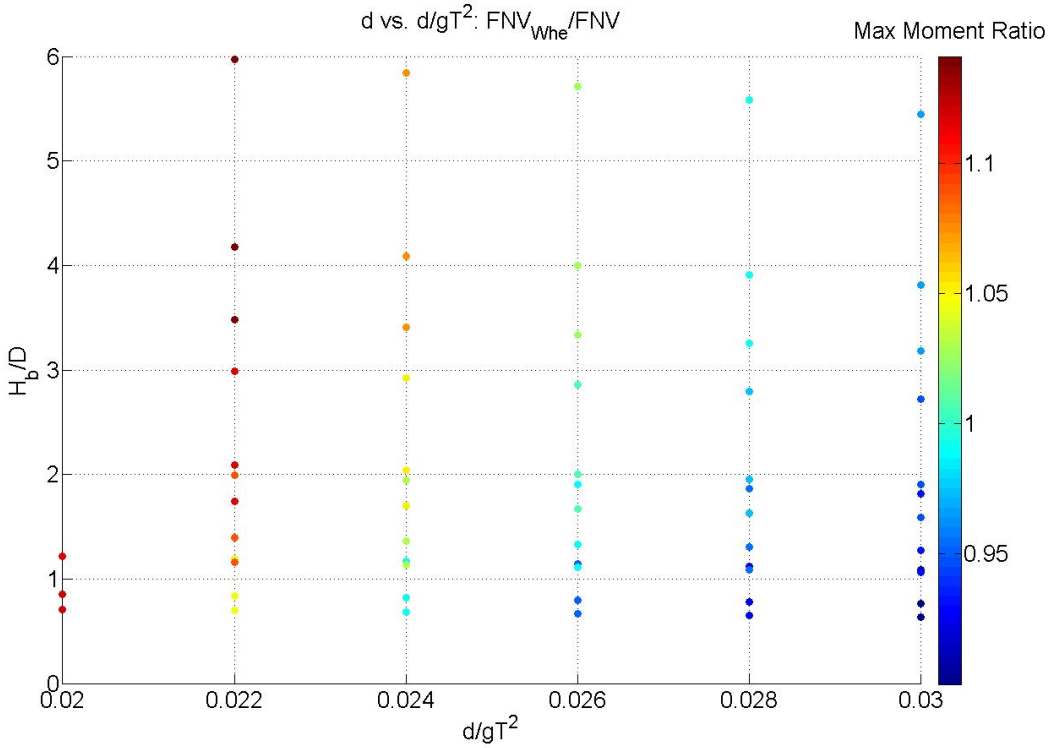

Figure 57 Max Moment Ratio Scatter Plot: FNV_{whe}/FNV

With this issue resolved, the full comparisons between methods over all the design cases are presented next. Wheeler is compared with LWT first. Figure 58 shows the max moment ratio using D/L on the x-axis. The figure is annotated as a reminder of where the water depths fall in this particular type of scatter plot. Previously, the max force was compared between these two methods using d/gT^2 on the x-axis (Figure 44). Similar to the forces, the same general trends are present in the max moment comparison. But, one important difference is that the max moment ratios are larger. This means that the effect of the moment arm for Wheeler is greater than for LWT. This result was mentioned in the previous discussion of the FNV moment. It is shown to be true here over the entire range of design cases considered. A more in depth analysis of the moment arms will be conducted later in this section.

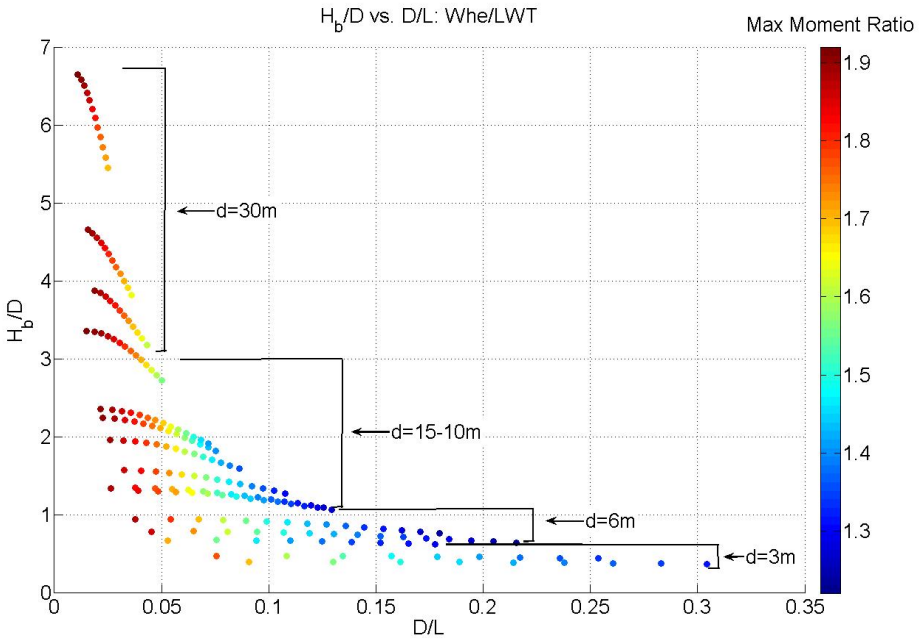

Figure 58 Max Moment Ratio Scatter Plot (D/L): Whe/LWT

Connections can also be made to the discussions of drag versus inertia dominated force types. For drag dominated design water depths, specifically 30 meters, the range of the max moment ratios is less than for more inertia dominated design cases. An example of an inertia dominated water depth is 6 meters. Remember that drag dominated cases have relatively smaller ranges of D/L at larger ratios of H_b/D. While there is less variability in max force ratios for drag dominated cases, the max moment ratios that are returned are larger than for the inertia dominated cases. In conclusion, the difference between the max Wheeler moments is consistently greater than LWT for drag dominated cases. As moments shift to more inertia based forces, the Wheeler method returns a wider range of max moment ratios. For these inertia based moments, the more intermediate water waves return smaller max force ratios than their shallow water counterparts. A design water depth of 3 meters provides a good example of this.

The comparison of Chakrabarti with LWT follows a similar discussion. Refer to Appendix Figure A1 for the max moment ratio scatter plot using D/L as the x-axis. Note that the max moment values have also significantly increased compared to the max force ratios between Chakrabarti and LWT present in Figure 45.

Comparing Wheeler stretching with Chakrabarti stretching for max moments is necessary. It was demonstrated that the max force ratio takes a range of consistently larger values. Refer back to Figure 46 to see this max force ratio range. Figure 59 shows the scatter plot with max moment ratio with Wheeler as the numerator and Chakrabarti as the denominator. Looking at just the range of max force values it is clear that the max moments are closer for Chakrabarti and Wheeler than the max forces are. This stands in

stark contrast to the previous two examples of Whe/LWT and Cha/LWT which returned max moment ratios significantly larger than max force ratios. Comparing Chakrabarti with Wheeler, this difference is particularly noticeable for the deeper depth design cases. In an attempt to explain this shift the effect of the moment arm was investigated.

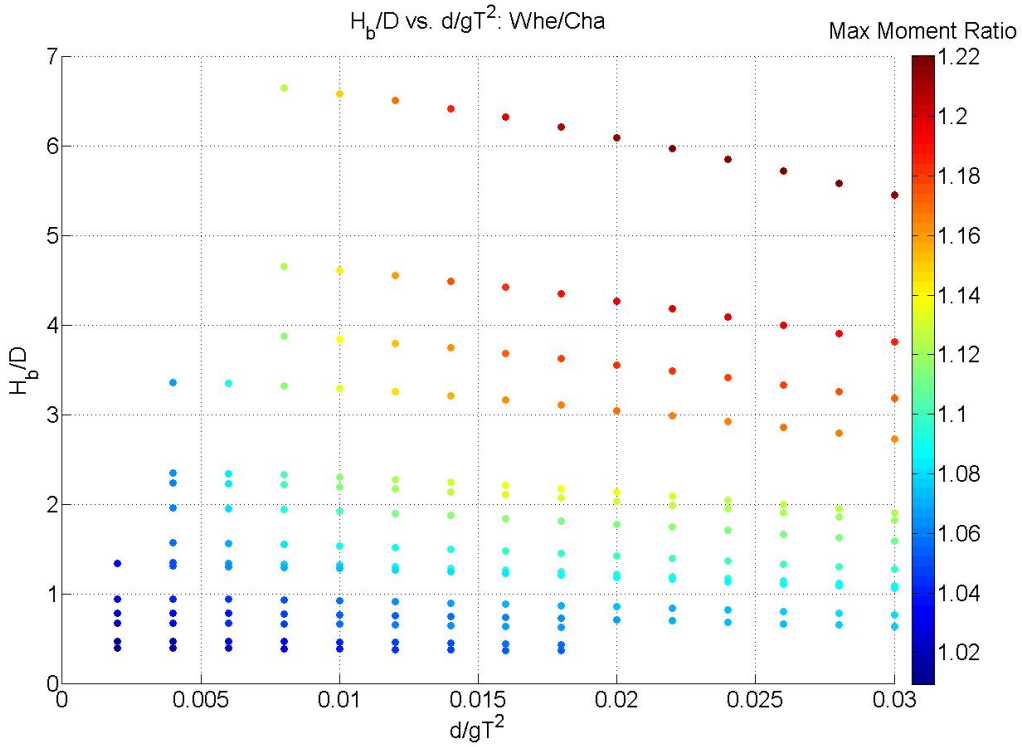

Figure 59 Max Moment Ratio Scatter Plot (D/L): Whe/Cha

The moment arm at the max moment was calculated using the force corresponding to the point of the max moment. The max moment and max force do not necessarily coincide. The specific procedure was outlined in the previous paragraphs concerning the calculation of the modified FNV moment. Refer to Appendix Figures A2 through A5 for scatter plots of the theta locations of the max forces and max moments

for both Chakrabarti and Wheeler methods. From these figures it is clear that for these methods the max force occurs later than the max moment. Although this lag is not constant, it is highest around the transition from drag dominated to inertia dominated waves. It can be as much as roughly 25 degrees for Chakrabarti and as high as 15 degrees for Wheeler.

The results from the moment arm analysis are also presented in scatter plot form. The moment arm results are non-dimensionalized using the water depth. Figure 60 and Figure 61 show the scatter plots of the moment arm/depth ratio for Wheeler and Chakrabarti respectively. The general trend for both clearly shows that the shallow water depth design cases have the smallest moment arms relative to their depths. Most noticeable in the design depth of 30 meters, there is an increase in the moment arm as waves become more intermediate. The smaller diameters exhibit an increase in the moment arm as well. While the general trends between the moment arms for Wheeler and Chakrabarti are the same, the relative magnitude of the arm for the maximum moment differs. The shallow water design cases return nearly the same values for both methods. But, Chakrabarti returns larger moment arms as the design depth is increased. This larger moment arm is the reason why Chakrabarti max moment values are more similar to Wheeler than the max force values.

The role of the moment arm is obviously important. It has been shown to vary depending on the theory. Refer to Appendix Figure A6 for a plot of the moment arm ratio scatter plot for LWT. The significantly smaller values for the LWT moment arm explain why the max moment increases so significantly compared to the max force

values in both Whe/LWT and Cha/LWT comparisons. The LWT moment arm has less of an effect than the stretched moment arms.

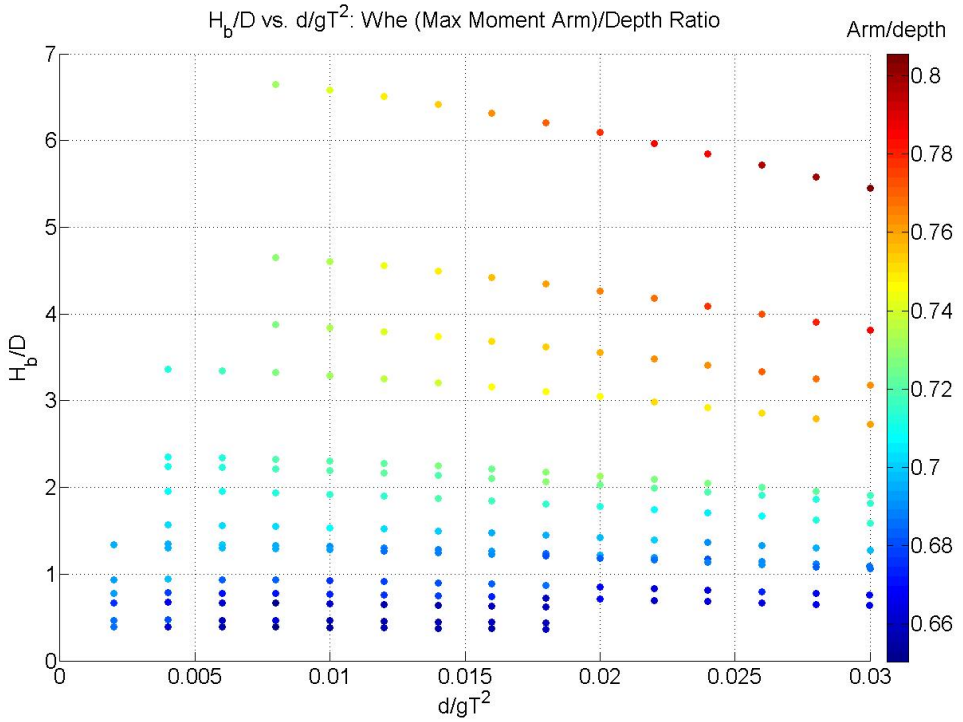

Figure 60 Moment Arm/Depth Ratio Scatter Plot: Whe

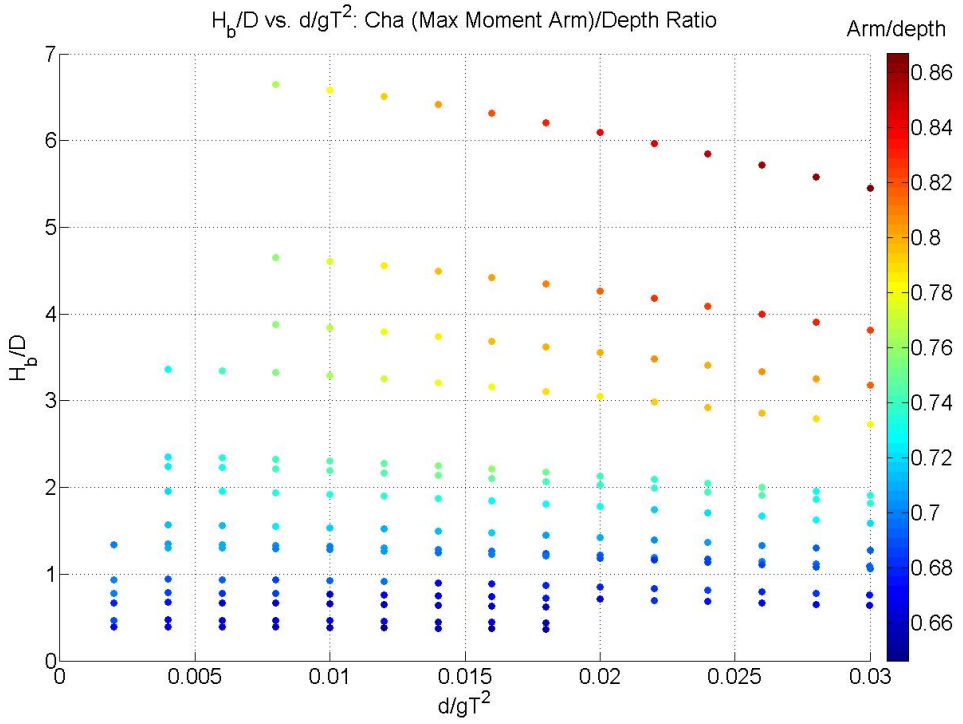

Figure 61 Moment Arm/Depth Ratio Scatter Plot: Cha

The comparison of the max FNV moment will follow. Connecting to the max force ratio comparisons between FNV and Wheeler in Figure 47, the max moment will use this same max moment ratio denominator. Figure 62 shows the max moment scatter plot for FNV and Wheeler. The general trends of max force are present here as well. After the point of convergence there is a considerable increase in the max moment ratio, especially at H_b/D values around 1. Except for a depth of 30 meters, all design cases on the line of convergence have larger max moment values than any of the linear methods. The max moment ratio in this comparison is modestly larger than the previous max force comparison at larger values of D/L. This implies that the moment arm for FNV theory is larger than the moment arm for Wheeler stretching in this range. Remember that the

moment arm for FNV theory is the inertial moment arm of Wheeler stretching. This means that the Wheeler inertial moment arm is greater than the combined Wheeler moment arm in this range of D/L. This result makes sense; the inertial Wheeler moment arm will be larger at larger values of D/L because for these types of waves the inertia force dominates. Consequently, the inertial Wheeler moment arm will return larger FNV moments for waves dominated by inertia forces.

Finally, a limited investigation of the max moments from stream function theory will be provided. Figure 63 shows the max moment ratio plot versus D/L for a water depth of 6 meters. The size of the max moment ratio for DSF is very significant. It shows that for this design depth, shallow water waves return significantly larger max moments than the simplest linear methods. Also the max moments are larger than even FNV theory at greater values of D/L. For max moments, DSF approaches the values of the other methods at more intermediate waters than was the case for max forces. So, not only are the DSF max moments larger, they stay larger for more values of D/L. That being said, FNV theory also appears to diverge less slowly than was the case for the max force example. Given the limitations of the FNV moment equation and the method used to calculate FNV moments here, the urge to reach far reaching conclusions should be checked. It is important to remember that the wavelength from DSF is different than LWT. The wavelength used in the max moment and max force plots of this type is from LWT. Since it is a comparison across methods, using a consistent wavelength is necessary.

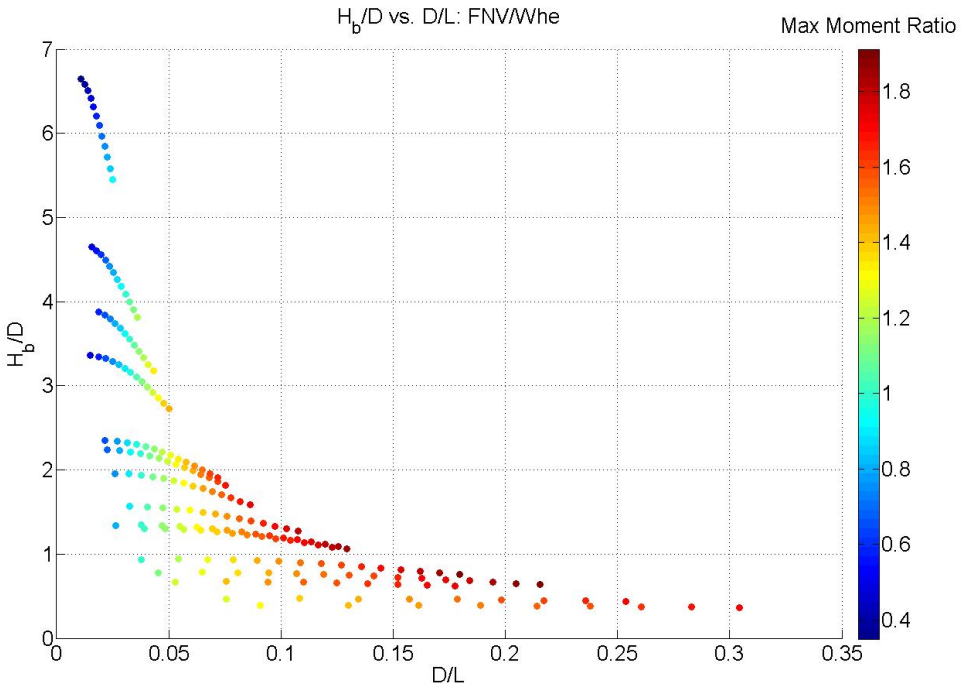

Figure 62 Max Moment Ratio Scatter Plot (D/L): FNV/Whe

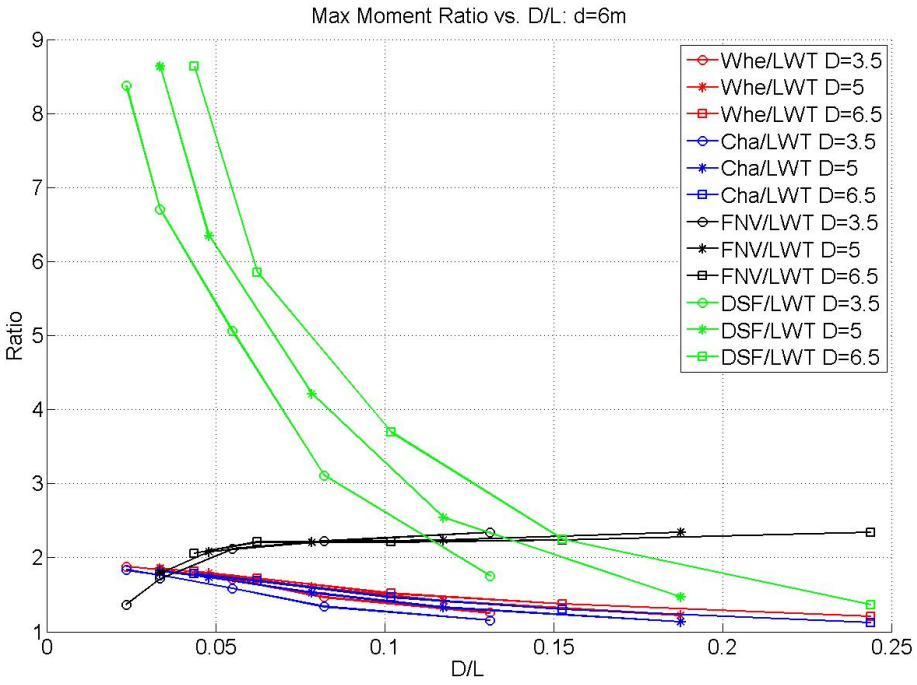

Figure 63 Max Moment Ratio vs D/L: (d=6m) All Methods

The nonlinear wave forms of DSF are the reason behind the significant increase in the max moment ratio. Not only are the kinematics concentrated near the free surface, but they also return larger moment arms for a design water depth of 6 meters. Figure 64 shows the scatter plot of the moment arm ratio from DSF. While a comparison across all the water depths is not possible with DSF, this limited comparison still provides significant results. It is clear that at max moment conditions DSF has significantly larger moment arms than any of the other methods. In fact, at certain values of d/gT^2 the forces are so concentrated above the mean water level the moment arm exceeds the water depth.

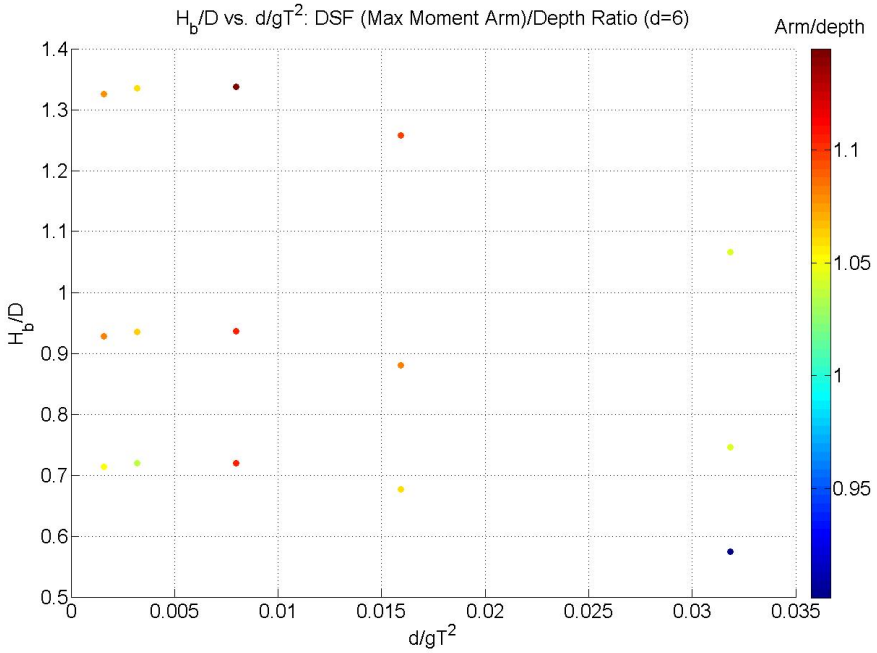

Figure 64 Moment Arm/Depth Ratio Scatter Plot: DSF (d=6m)

4.8 Plunging Impact Load Comparison

As a breaking wave transitions from spilling to plunging the additional impact load must be accounted for. The range of design cases susceptible to plunging type breaking are established earlier in the results section. Now, a comparison of the actual force values of these impact loads is necessary. Looking to section 2.4, equations 2.52 and 2.53 are used in this analysis. Note that these equations provide the time evolution of the force as well as the max value. These equations are complicated, but max values occur at time equal to zero. As a result, these equations essentially simplify to equation 2.51 with a slamming coefficient equal to 2π applied over a certain area.

For this analysis there are two main ways of calculating the values. The inputs of velocity V, and crest elevation η_b can be determined with either LWT or DSF. These two different approaches return very different impact forces as will be shown. Note that velocity in these equations uses wave celerity. This approach is used in both International Electrotechnical Commission's IEC 61400-3 and Germanischer Lloyd's "Guideline for the Certification of Offshore Wind Turbines". Wave celerity follows directly from the division of wavelength with wave period. While both approaches will use the same wave period, the wave length will vary depending on the wave theory. One input that will remain constant for both approaches will be the curling factor λ, This will maintain a constant value of 0.5, as established for plunging waves by Wienke and Oumeraci (2005).

The following analysis will look at the dimensional impact results from DSF before moving to comparisons between the two methods. The impact force profile for

DSF is displayed in Figure 65. The particular design case is not necessarily important. This profile is shown to illustrate a typical profile from the impact force formulation. Also, it serves as a general check of the program used to calculate these results. The profile starts off with a maximum force value at t=0. Also, the decay is formulated with two different stepwise functions. These two facts are evident in this profile. For this example the switch occurs around 40 milliseconds.

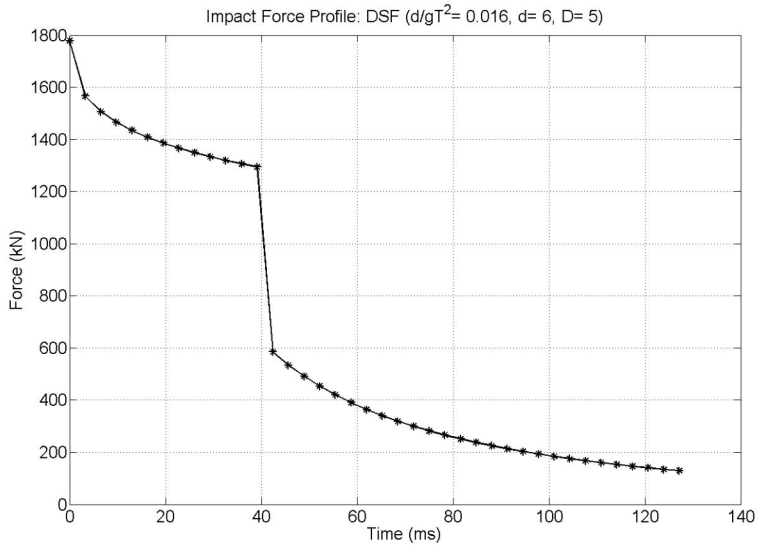

Figure 65 Impact Force Profile Example

A comparison of a selected range of dimensional impact values is next. Figure 66 shows the dimensional impact force scatter plot for a constant diameter of 5 meters across all design depths. It is clear that for a constant diameter the impact increases significantly for deeper design depths. Also evident in this figure, the impact force decreases as waves become more intermediate. Figure 67 shows the dimensional impact force scatter plot for a depth of 3 meters over all diameters. It is clear that larger

diameters return larger impact forces. The trend of decreasing impact values for more intermediate waves is evident for lower water depths as well.

A comparison of the length of the impact is also important. The length of the impact is necessary for a full understanding of the force and is particularly important when considering aspects of structural dynamics. Figure 68 shows the dimensional length of impact for a constant diameter of 5 meters across all design depths. The length of the impact is very short for all design depths. But, the deeper water depths have lengths of impact as much as 3 times larger than the shallowest of depths. Figure 69 shows the length of impact scatter plot for a depth of 3 meters over all diameters. The length of impact is longer for cylinders with larger diameters.

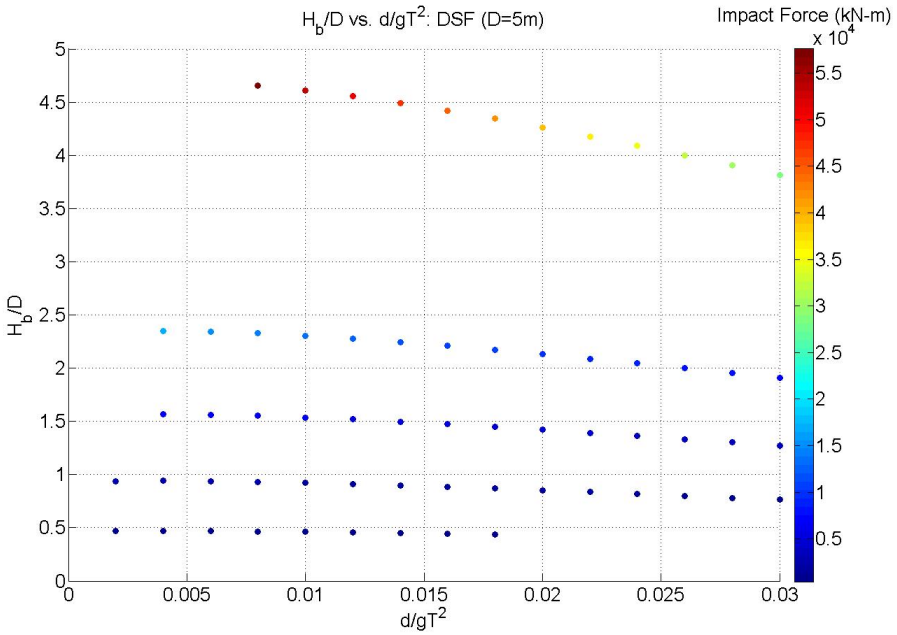

Figure 66 Dimensional Impact Force Scatter Plot: DSF (D=5m)

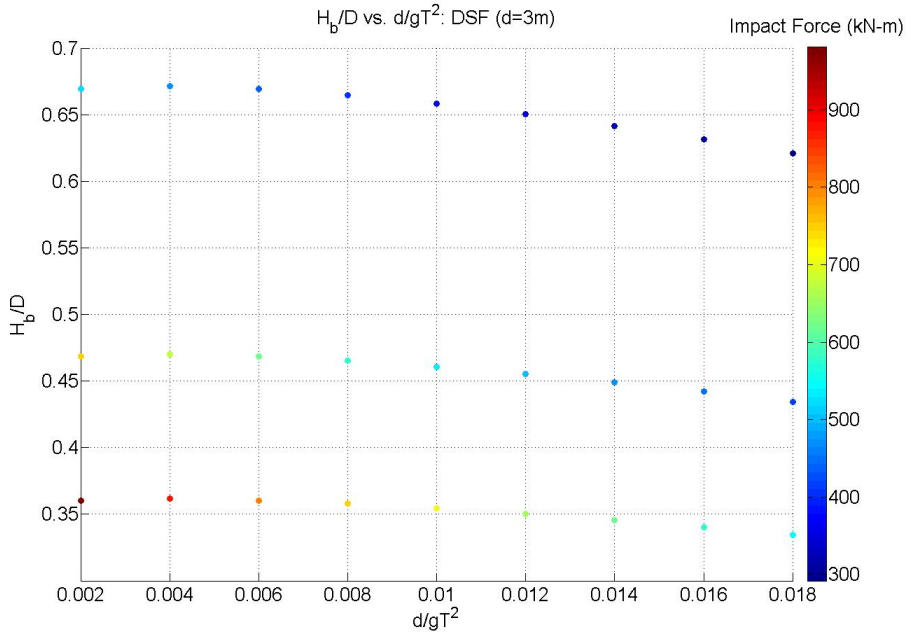

Figure 67 Dimensional Impact Force Scatter Plot: DSF (d=3m)

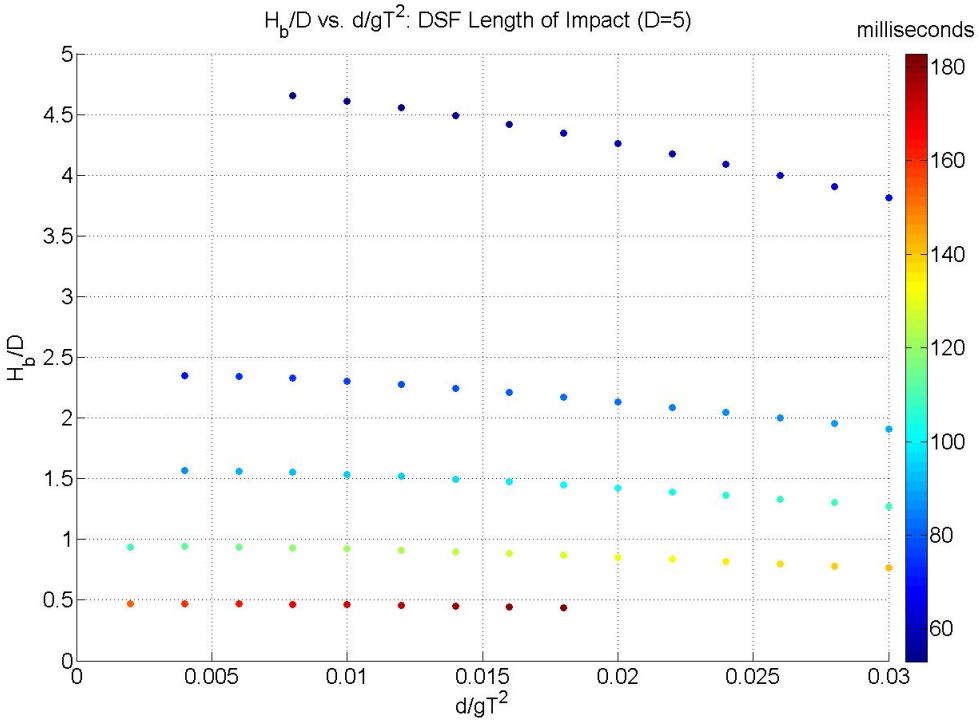

Figure 68 Dimensional Impact Length Scatter Plot: DSF (D=5m)

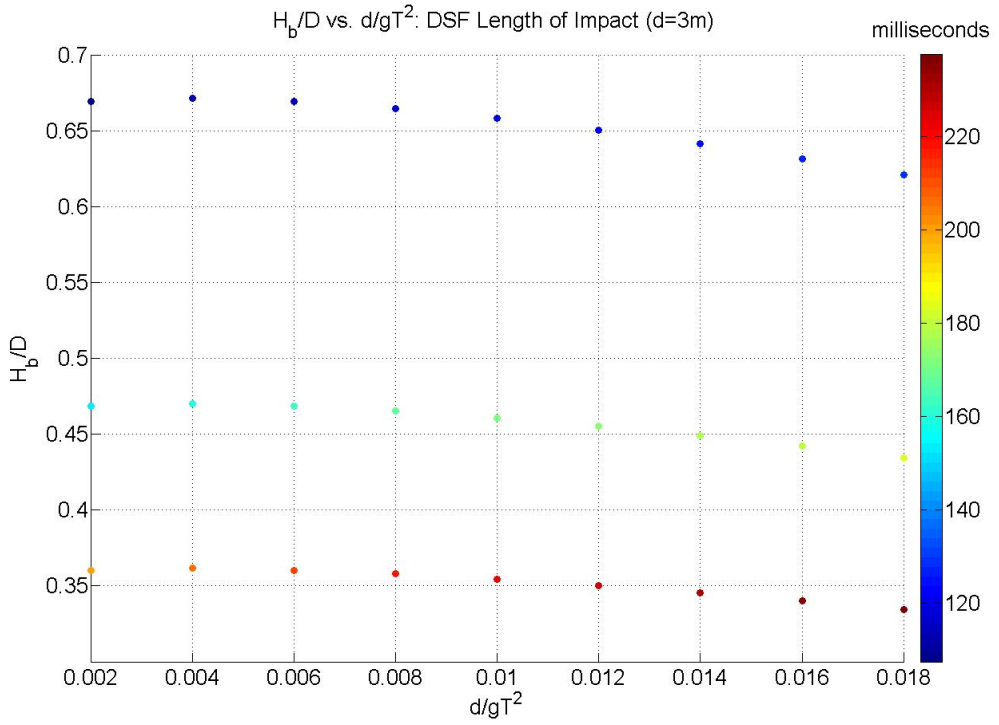

Figure 69 Dimensional Impact Length Scatter Plot: DSF (d=3m)

In comparing the two methods interesting differences and similarities arise. Figure 70 shows the impact force ratio between the two methods. DSF is in the numerator and LWT is in the denominator. Impact forces using DSF variables are at least twice as large as LWT impact forces. This difference increases as shallower water waves are considered. Another interesting outcome is that the factor for a particular value of d/gT^2 is constant across all diameters and water depths. Figure 71 shows similar results for the length of impact ratio where LWT is the numerator and DSF is the denominator. In this case the difference between the two methods is quite small. LWT returns longer impact lengths for shallow water waves than DSF. This difference

decreases slightly as waves become more intermediate. The constant ratio across all diameters and design depths is also present here.

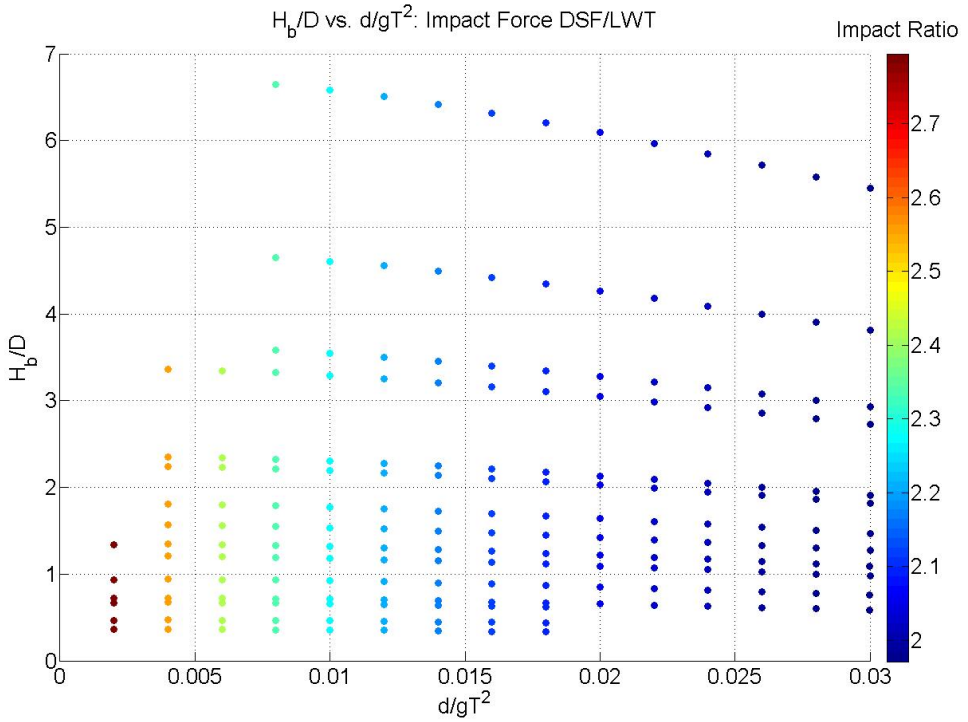

Figure 70 Impact Force Ratio Scatter Plot: LWT/DSF

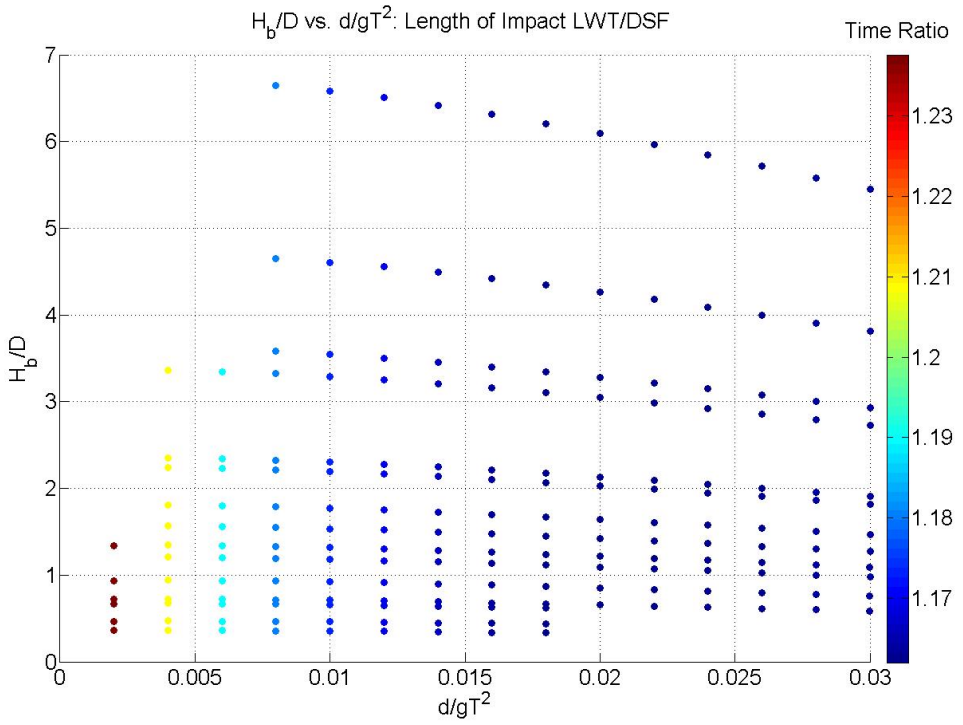

Figure 71 Length of Impact Ratio Scatter Plot: LWT/DSF

These results are not particularly surprising considering what the ratios are comparing. The impact ratio essentially compares the ratio of crest elevation and wavelength squared between the two methods. While the length of impact ratio compares the ratio of the inverse wavelengths. Equations 2.52, 2.53, and 2.54 will make this clear. The ratio of LWT to DSF wavelengths is included in Appendix Figure A7. The ratio of LWT to DSF crest elevations is included in Appendix Figure A8. For both these comparisons the constant ratios for a particular type of wave across all diameters and water depths is clear. This further explains the results of the impact method comparison.

The combination of impact forces with the regular hydrodynamic forces represents the combination of everything discussed thus far. The discussion will begin

with a comparison of force profiles and end with the full comparisons using scatter plots. The combined force profiles will make use of the DSF force profiles. Consequently, the limited design parameters for a water depth of 6 meters need to be used. Figure 72 shows the combined profiles for DSF examples for shallow and intermediate examples. A number of things are apparent in this figure. First, the difference between the impact force profiles is clear. Connecting with the previous discussion, the length of impact for shallower water waves is clearly smaller. Also, the impact force is larger for shallow water examples.

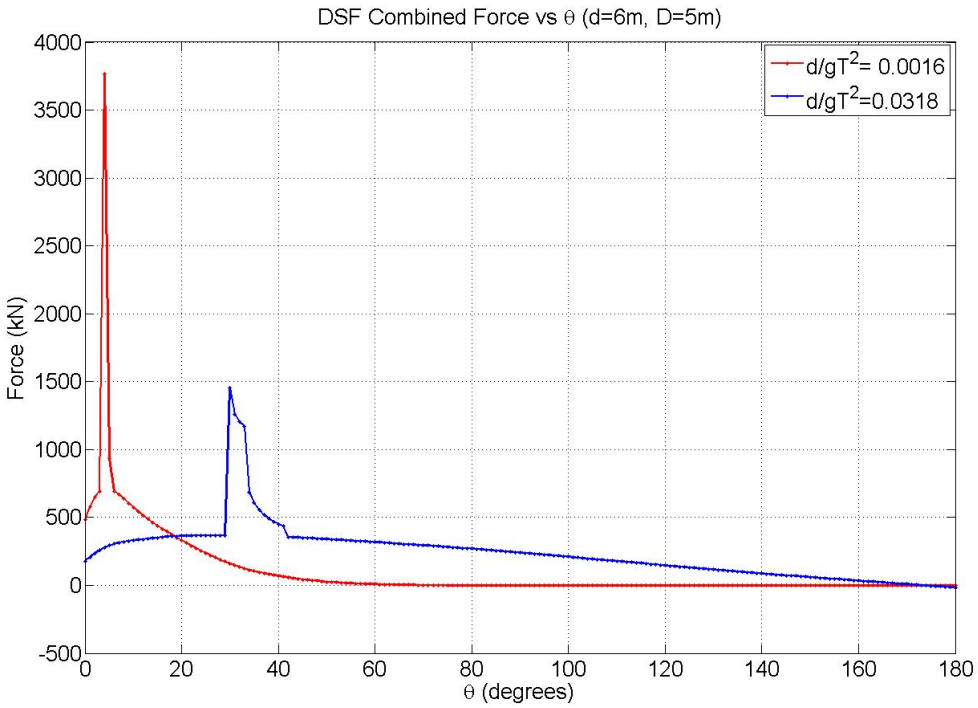

Figure 72 DSF Combined Force Profiles: Shallow and Intermediate Comparison

The locations of the impact forces are also at different values of theta. Very little guidance was given in the design standards for locating impact force theta location.

Wienke and Oumeraci (2005) claim that force of a breaking wave can be divided into a quasi-static force as well as a dynamic component. This is the approach taken from the beginning of the analysis. Given the uncertainty of locating the dynamic impact force, it is applied to the location of maximum quasi static force. This is the conservative solution in terms of max force calculation. The location of the impact forces in Figure 72 clearly coincides with the maximum DSF forces.

The combined force profiles plotted against other methods are also useful comparisons. Figure 73 shows the combined force profiles of a number of selected methods for shallow water. Figure 74 displays the combined force profiles of the same methods for intermediate water. For the shallow water example, a number of things stand out. The difference between the DSF impact force and the LWT impact force is largest for shallow water. Compare with Figure 70 in the initial impact analysis. A general sense of the scale of forces can be gained. Also, the max force location for each method is clearly visible in this comparison. Cross comparing with the intermediate example, a lot of the same general conclusions can be made. For intermediate water the max force and impact force of DSF are less extreme compared to the linear method of calculating these two distinct forces.

The full scatter plots will complete the combined force analysis. Figure 75 shows the full scatter plot of the ratio between the impact force and the regular max force for LWT. For the 30 meter depth design waves there is clearly a significant difference between these two forces. For low values of D/L and larger ratios of H_b/D the LWT impact force is significantly larger than the regular hydrodynamic wave force. For the

design cases investigated, a constant diameter with decreasing wavelength (increasing D/L) returns significantly lower ratios of impact to regular max wave force. Looking to the 3 meter water depth as an example, the shallowest water waves have larger values of LWT impact relative to the regular max force than intermediate waves at the same water depths with significantly larger values of D/L. This variability in the impact to force ratio is only present for design water depths with a large range of D/L values. For instance, the range in the impact of force ratio is not nearly as pronounced in the 30 meter example. The same trend is present in Figure 76 for the comparison of the DSF impact with the regular LWT force. As expected, the magnitudes of the ratios are much larger.

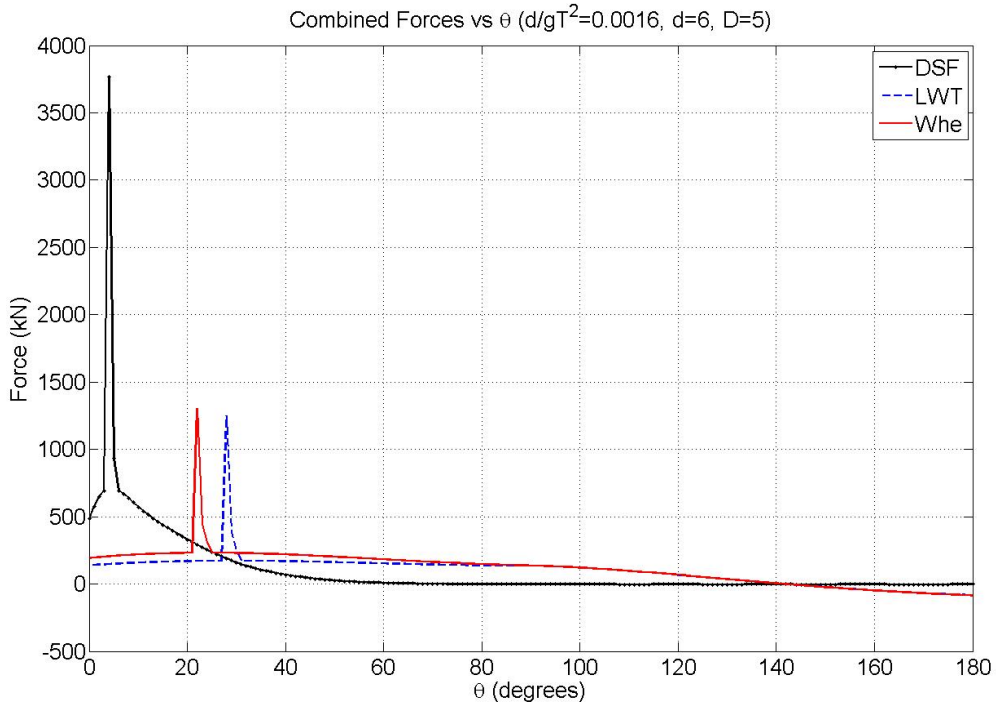

Figure 73 Combined Force Profiles: Selected Methods (Shallow Water)

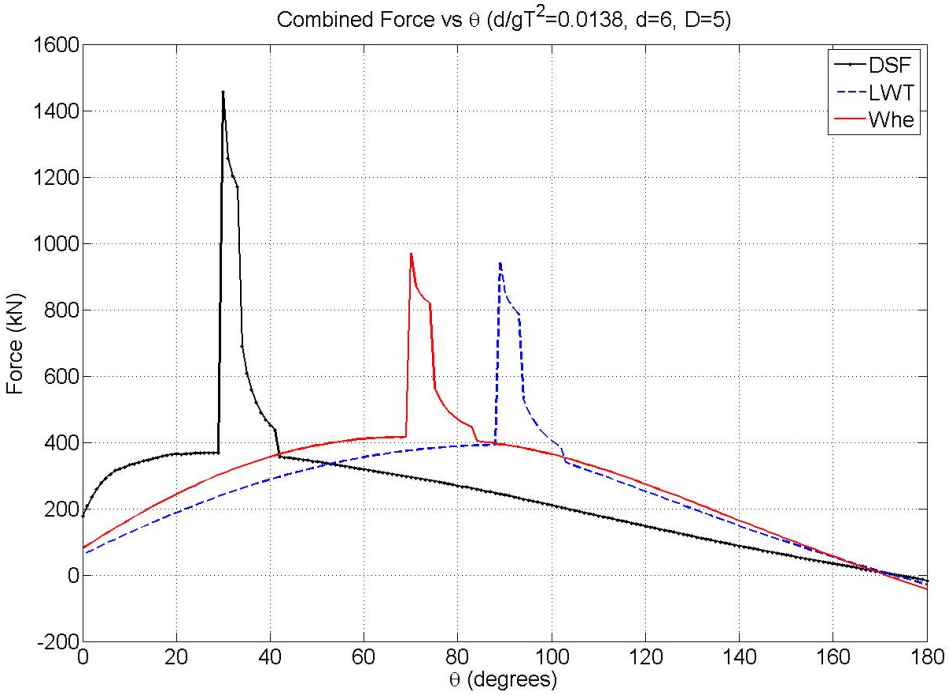

Figure 74 Combined Force Profiles: Selected Methods (Intermediate Water)

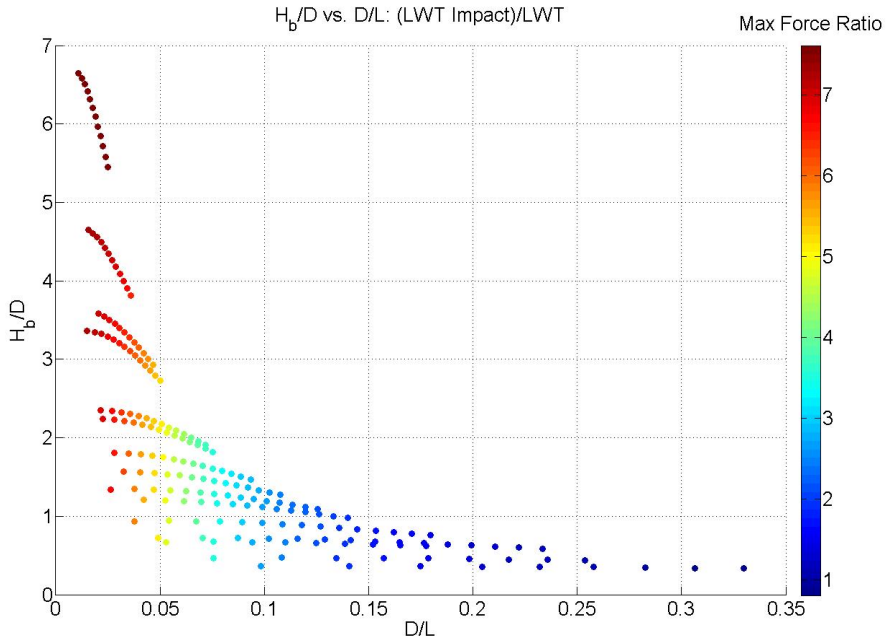

Figure 75 LWT Impact and LWT Max Force Ratio Scatter Plot: (D/L)

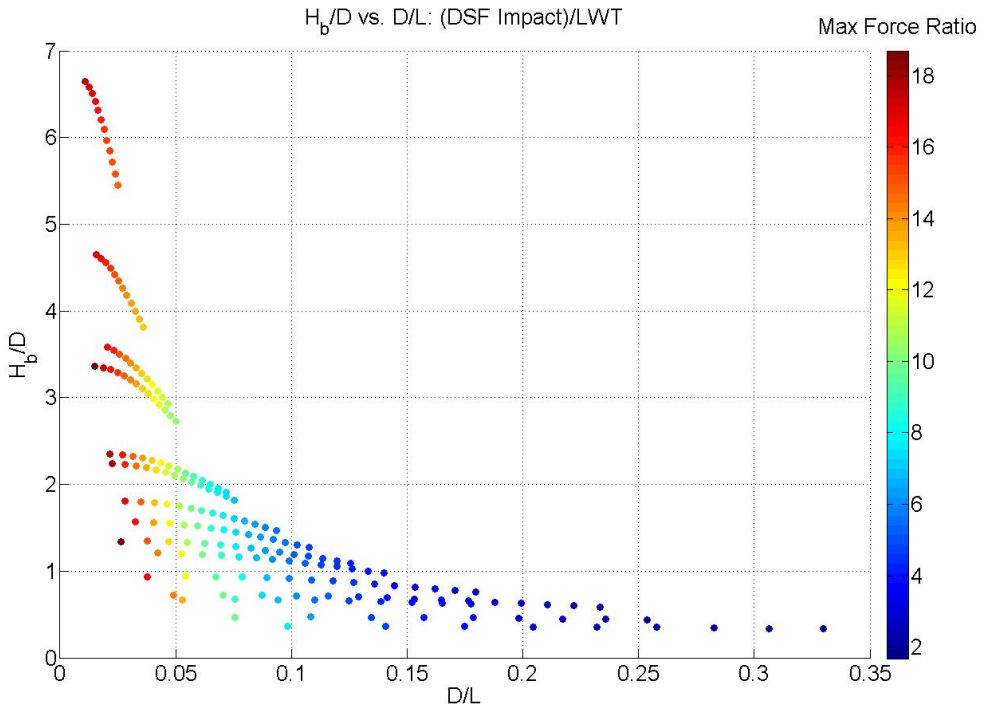

Figure 76 DSF Impact and LWT Max Force Ratio Scatter Plot: (D/L)

Comparing the DSF impact with a wave theory that returns larger max force values gives a better sense of the actual scale of the DSF impact forces. Figure 77 shows the DSF impact compared with the FNV max force values. Clearly noted on the figure, the water depths chosen are the ones that exist on the line of convergence. For the design cases that have converged, the range of DSF impact to FNV max force ratios is from about 7 to less than 2. This is very similar to the range in Figure 75 which compared LWT impact to LWT max forces. When considering comparisons between max impact forces and max hydrodynamic forces the choice of method for both is very important. The differences between methods in both cases provide the designer a wide range of possible force values and an even larger number of combinations.

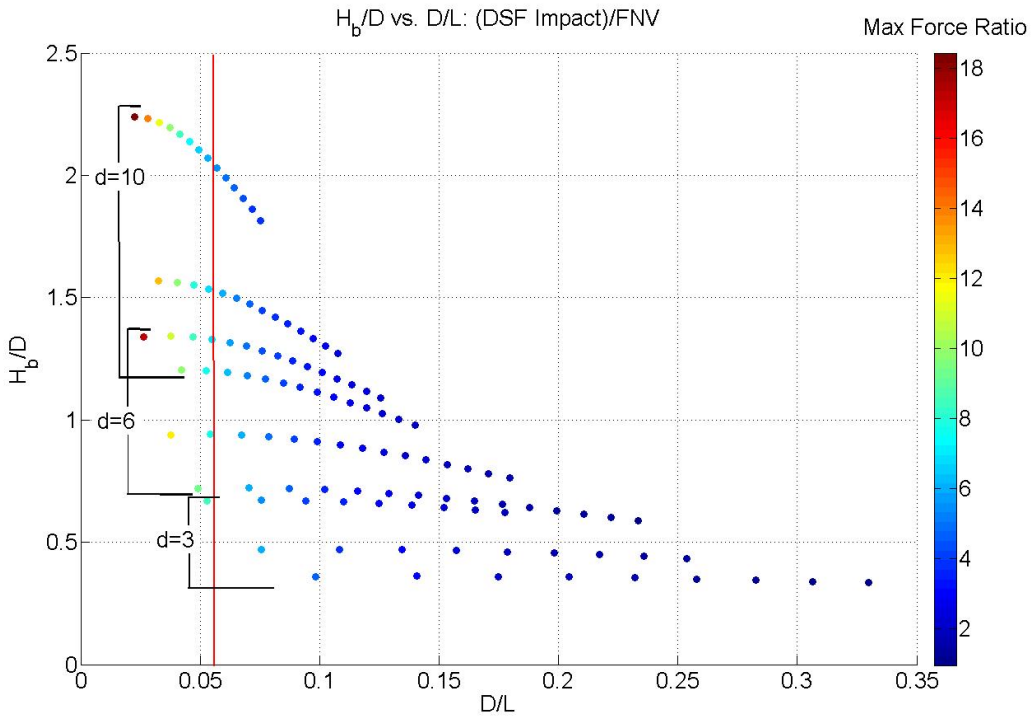

Figure 77 DSF Impact and FNV Max Force Ratio Scatter Plot: Selected (D/L)

A discussion of the moments that result from the impact force is also necessary. Given the strong concentration of this force in the crest it provides a very real chance to significantly increase the moment. In the introductory sections, a discussion of the location of the impact force used the results of Weinke and Oumeraci (2005) to show that the impact forces inside the area of contact can be conservatively modeled as uniformly distributed. Given the uncertainty in this calculation this approach was used. The total impact force uses the maximum crest wave height as an input so this was also used in the impact moment calculation. This again is a simplification since the impact force was located at the max force value. This does not necessarily coincide with the max crest elevation of the wave. In fact the location of the max force and impact force occur at much larger values of theta. The max moment and max force values from the

regular passing wave have been shown not to coincide for most methods. The addition of the impact moment to the moment at the location of the max force will shift the theta location of the max moment. The uncertain nature of the impact location makes the decision of where to locate the impact moment more difficult. In the face of this uncertainty a general discussion of the impact moment will suffice.

This discussion will include the use of DSF max moments so the limited design cases at the 6 meter depth will be used. Figure 78 shows the scatter plot of the impact moment to max moment ratio for DSF. It is important to remember that the three horizontal groupings result from the three different diameters chosen for investigation. From this limited example it is clear that smaller diameters result in larger differences between the DSF impact moment and DSF max moment. Also, shallower waters waves return larger moment ratios.

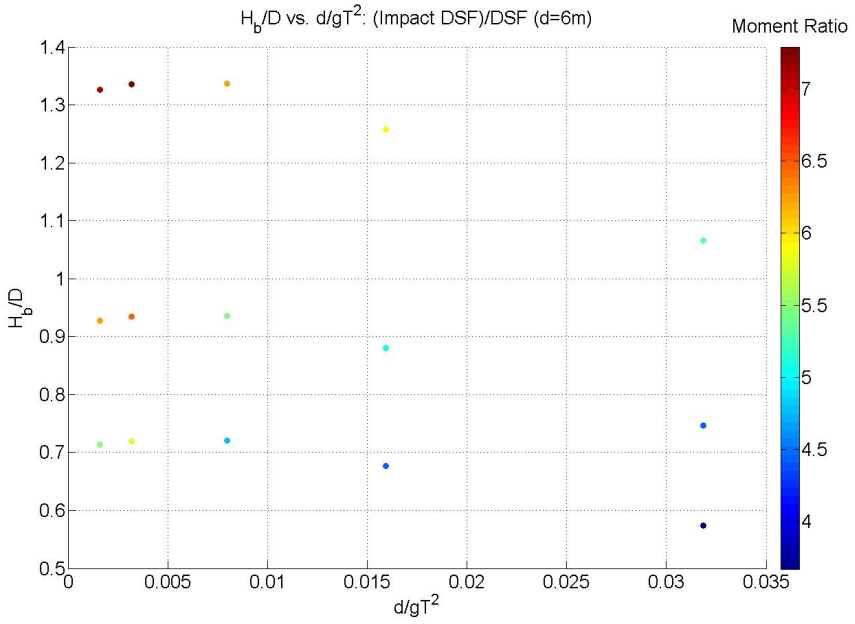

Figure 78 DSF Impact Max Moment Ratio: (d=6m)

Figure 79 shows the scatter plot of the moment ratio for the LWT example. The same general trends of increasing ratios for smaller diameters and larger ratios for shallower water waves are also present. But, the difference between the LWT impact moment and LWT max moment is significantly larger for the shallow water waves. It is interesting that the minimum values are around the same value in both Figure 78 and Figure 79 and occur for intermediate water waves on large diameters. The significant increases in the ratios for the LWT example are a result of a number of factors. The difference in the moment arms of both the impact and regular max moment is greater for LWT than DSF. Also, just the general magnitude of differences between the two methods plays a role. The max moments for DSF are significantly larger in shallow water than for intermediate water. While the difference between the moments for DSF is lessened in shallow water due to the effect DSF has in shallow water. This effect is not repeated for LWT for waves in shallow water. This is why the ratios in intermediate water are nearly the same for both DSF and LWT.

The full design case comparison of the difference between the two methods for determining impact moments is shown in Figure 80. The trends present in the discussion of the impact forces are also visible here. Shallow water waves have the largest difference between the two methods. Each value of d/gT^2 returns the same ratio of impact moments. A couple of things come into play in determining these trends. Obviously, the trend of the force plays a major role. The similarities between ratios of impact moments and the ratios of impact forces are not surprising. But, comparing to Figure 70 the moment ratio clearly increases. This increase is a result of calculating the

moment arm, which differs for each method. The nonlinear wave forms used by the DSF approach have significantly higher crests than the LWT wave profiles. Consequently, the moment arm for DSF is larger. This difference between the approaches is particularly significant for shallow water waves, which is why the difference between the impact moment ratios is larger than the impact force ratios in shallow water. Stated another way, the difference between the impact moment ratios and the impact force ratios is less for intermediate water waves. This is because the wave forms and moment arms of DSF are closer to LWT approximations.

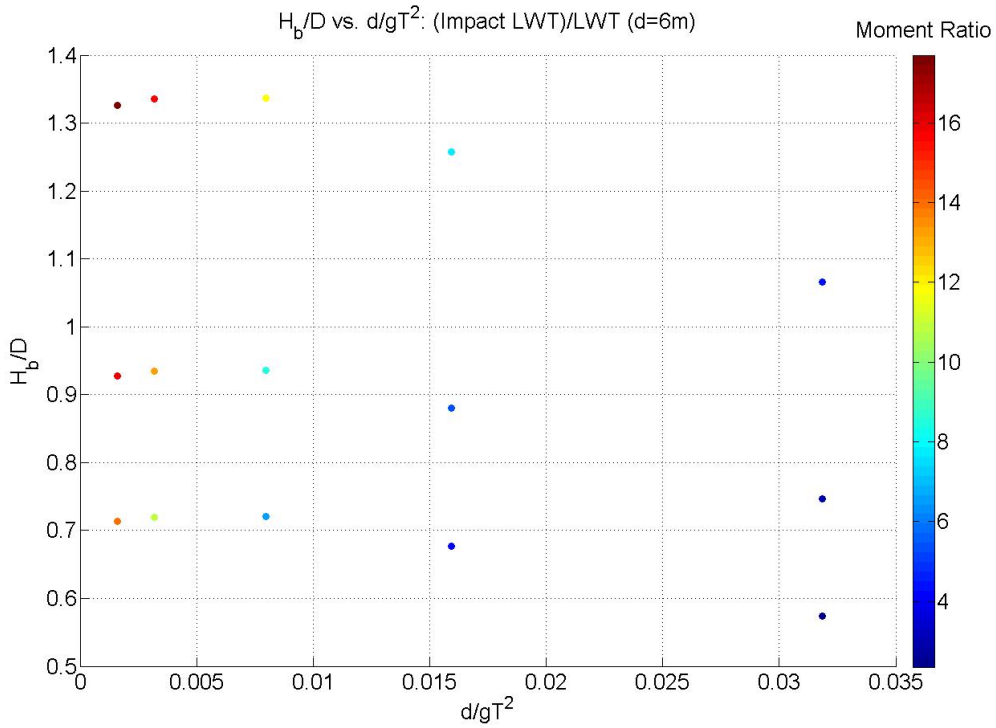

Figure 79 LWT Impact Max Moment Ratio: (d=6m)

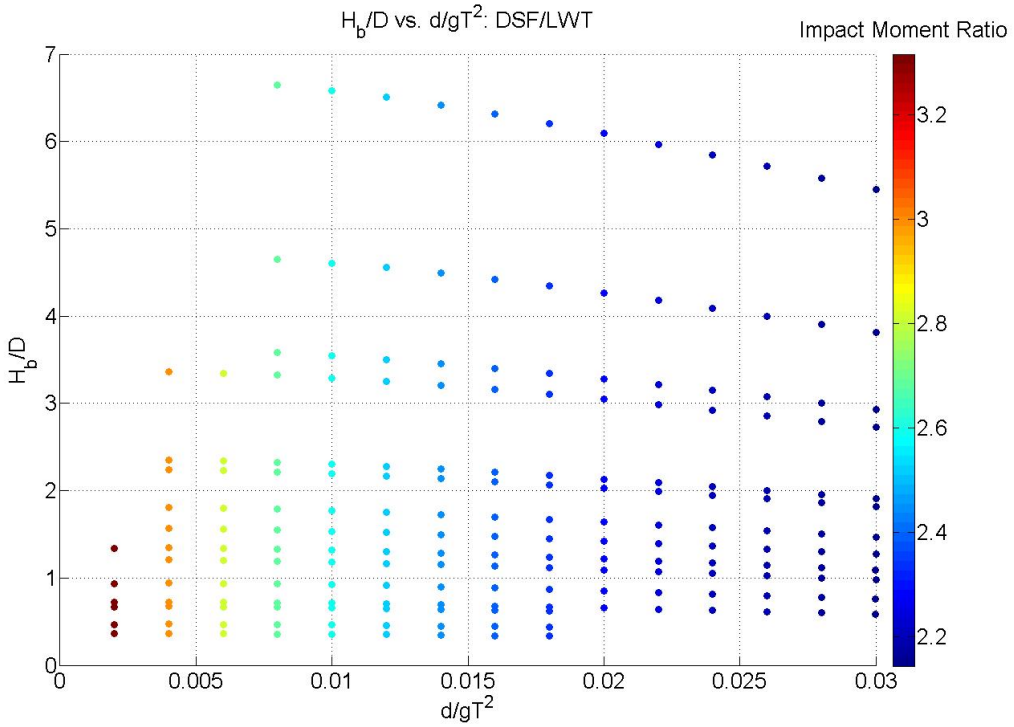

Figure 80 Impact Moment Ratio: DSF/LWT

4.9 Apparent Fixity Results

The results from the apparent fixity analysis extend the discussion of max moments. Increasing the moment arm will undoubtedly result in larger moments. Adding the effect was accomplished by first determining the moment arm. The moment data for the inertial case is known for every value of theta. These values were divided by the correlating force values. This results in a vector of moment arms for inertial forces. This value was then added to the value for apparent fixity (6D). This updated apparent fixity moment arm vector was then multiplied by the inertial forces. This same procedure was completed for the drag components. After this point the resulting total moment for apparent fixity was calculated the same way as before.

Figure 81 shows the max moment ratio comparing the apparent fixity moment with the regular max moment. Not surprisingly, the effect is greatest in shallow water depths. The effect of larger diameters on apparent fixity is also clear. The larger diameters return larger moments. This result seems trivial but the figure provides a sense of scale resulting from including this additional consideration. For wind turbines, having a 6.5 meter diameter substructure in 3 meters of water is not a realistic solution. But, this full comparison does illustrate the sensitivity of shallow water to increases in moment arm length.

Figure 82 shows a detail at 30 meters of the same type of scatter plot for the same comparison of LWT. Again, the same trends of larger ratios for larger diameters are present. Also, for this water depth there is a slight decrease in the ratios as more intermediate water waves are considered. But this effect is very slight. Figure 83 shows the full scale results for the ratio of apparent fixity using FNV theory and max moments from FNV theory. The same effect in shallow water is also present. Note that the scale of the ratio values differs as well. The effect of apparent fixity on LWT is greater than on FNV. This result makes sense. Since the forces and moment arms of LWT are smaller than FNV, applying an apparent fixity value equal for both will result in a greater effect for LWT.

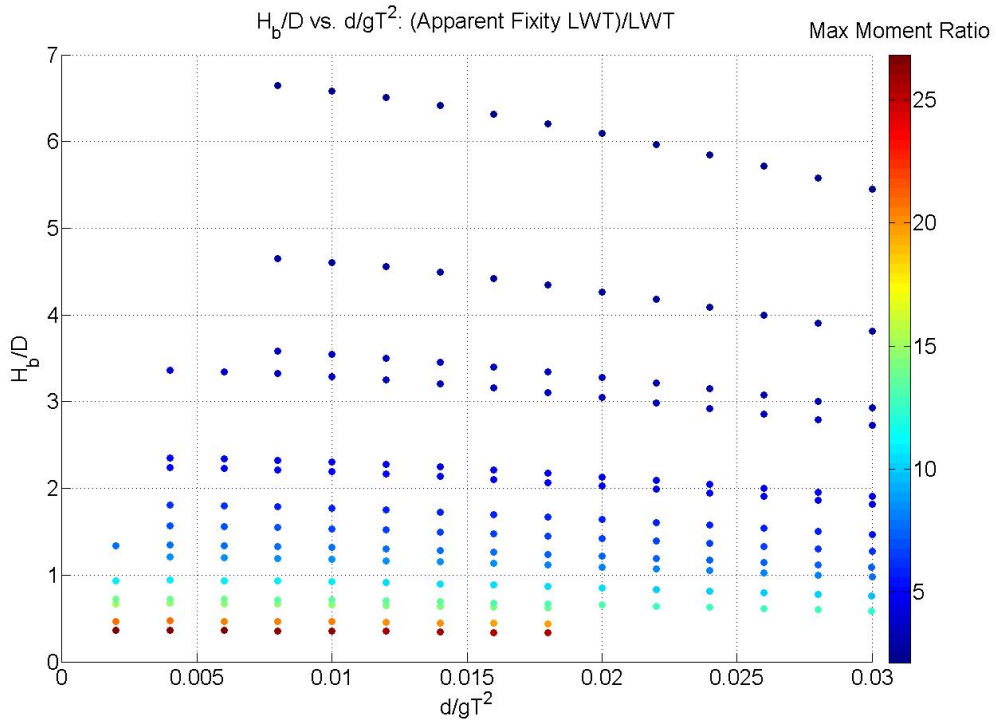

Figure 81 Apparent Fixity Ratio: LWT

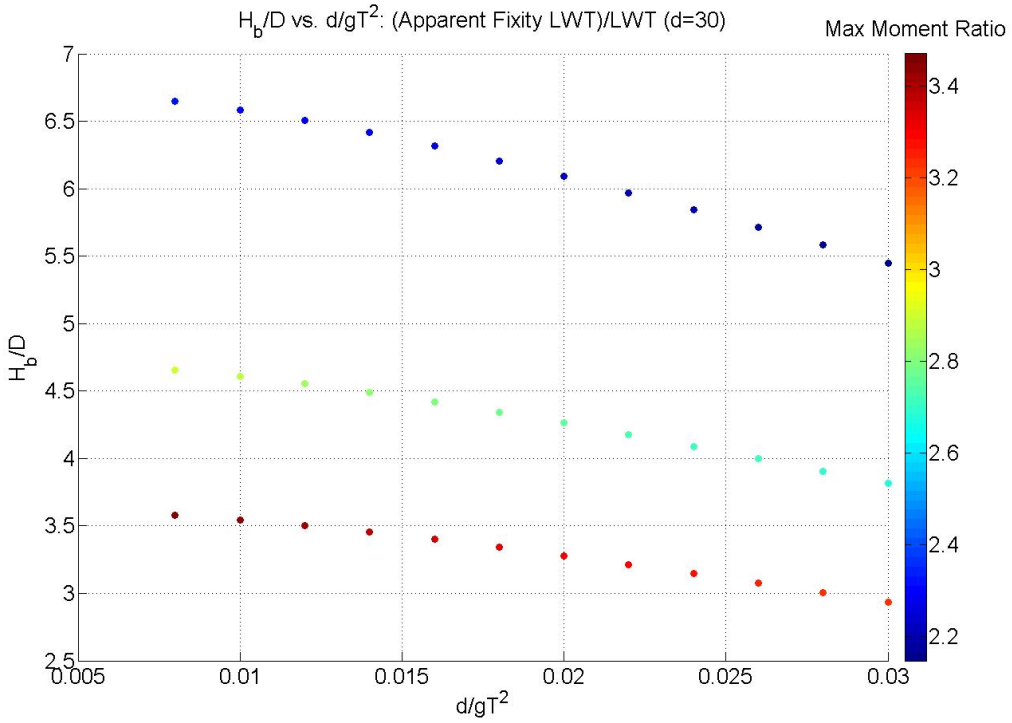

Figure 82 Apparent Fixity Ratio: LWT (d=30m)

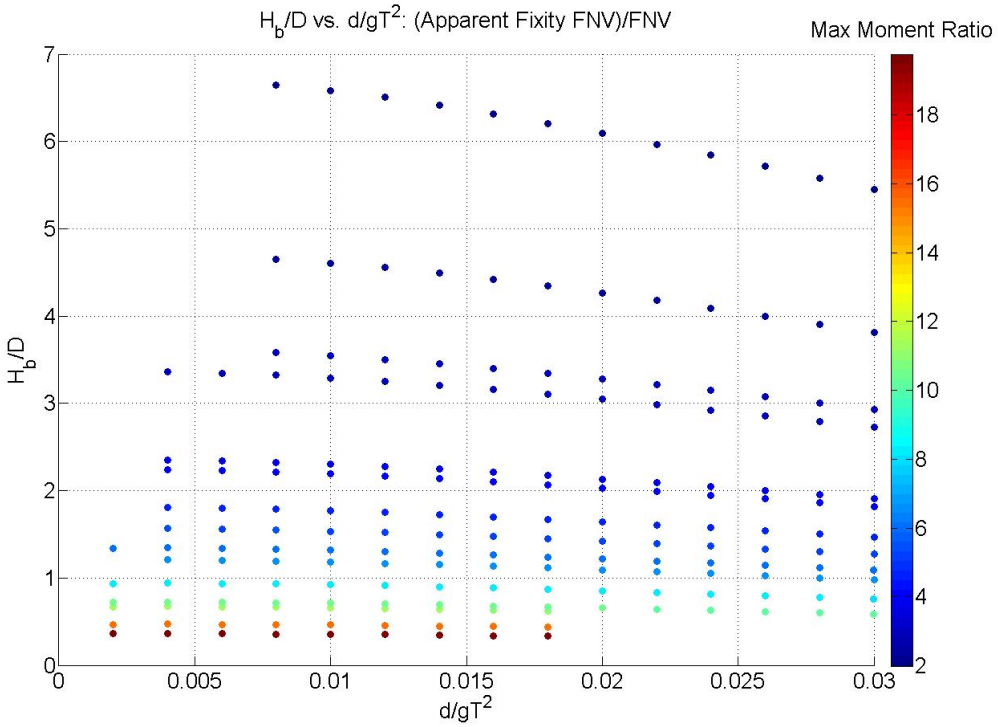

Figure 83 Apparent Fixity Ratio: FNV

5. SUMMARY AND CONCLUSIONS

There are a number of factors that are important to consider in the engineering design of breaking waves. The design wave, the site conditions, and the size of the structure all enter into the calculation of breaking wave loads. These essential inputs can be reduced to five basic design variables: breaking wave height (H_b), wave period (T), water depth (d), cylinder diameter (D), and bottom slope (S). Using realistic ranges for these variables a parametric study of breaking wave forces on monopile substructures were performed and the results presented.

Of particular interest was the investigation of the different methods available for determining breaking wave loads. Two different wave force theories were presented and compared for the selected design cases. The basic wave force formulations, ie. the Morison equation and FNV theory, were shown to be fundamentally different. While the design wave period, wave amplitude, and water depth are directly input into FNV theory with no specification of wave force transfer coefficients, these are required by the Morison wave force equation along with the wave kinematics. In order to investigate the sensitivity of the Morison wave force predictions to estimates of the wave kinematic estimates based upon linear wave theory, and the numerical Stream function wave theory was compared. Due to the importance of crest kinematics, linear wave theory required the introduction of kinematic stretching. Two commonly used first order methods were investigated, ie. Wheeler stretching and Chakrabarti stretching. The Dean's Stream function wave theory required no stretching as the wave theory provides a complete

kinematic description beneath the wave profile in the design wave. The contribution to the wave force from plunging wave breaking presents another critically important source of loading. The inclusion of the breaking wave impact force equations based upon linear or nonlinear wave kinematics models were contrasted.

In this research investigation several interesting trends were observed for the practical range of design variables selected. There are basic differences between shallow water and intermediate water waves. Shallow water waves were shown to have larger breaking wave heights, longer periods, and longer wavelengths. Typically, shallow water waves were also shown to have larger hydrodynamic and impact loads for certain ranges of water depths.

This study illustrated the critical nature of determining the breaking wave type, as not all breaking waves have impact forces. While the impact force differed in magnitude for the different water depths, it is clear that the presence of impact loads presents a significant source of additional loading. Shallow water waves were shown to be more prone to plunging and as a result more likely to have impact loads. Another interesting conclusion is that larger breaking wave heights result in waves theoretically less prone to plunging. This is important for the designer when comparing the choices available for breaking wave heights for a particular wave period. Smaller breaking wave heights will result in a conservative estimate of when to consider impact forces.

In the comparison of the max forces from the different wave force theories, important conclusions were drawn. The DSF/LWT ratio is significantly larger for shallow water waves. Similarly, the DSF force approaches other methods for more

intermediate water waves. This means that for shallow water waves the nonlinear aspect of DSF significantly affects the max force and moment values. But, for intermediate water waves the nonlinear aspect of DSF does not offer different results from the other linear methods. The Whe/LWT ratio also increases for shallow water waves. This shows that the stretching of kinematics has an effect for shallow water waves. Also, the Whe/LWT ratio increases for the deeper water depths investigated. So, the effect of stretching the kinematics on the max wave force is greatest for shallow water waves in deeper water depths. Unlike the other comparisons, the FNV/LWT ratio increases for more intermediate water waves. So, while other methods return max forces that approach LWT in intermediate water, FNV theory returns forces that increase when compared to LWT when more intermediate waves are considered.

The stretching techniques of LWT were also compared. It was shown that Wheeler stretching results in forces and moments consistently larger than Chakrabarti stretching. This trend changes when different water depths are considered. For the shallower water depths, Wheeler and Chakrabarti stretching are similar over the full range of shallow and intermediate waves. The difference between these two methods is relatively small for the shallow water depths. As deeper water depths are considered the difference between the methods increases. And at these deeper water depths the difference is greatest for more intermediate water waves.

The presence of impact loads is established by differentiating between spilling and plunging breaking waves. Relative to the max forces of the hydrodynamic loads, the impact force is largest for shallow water waves at deeper water depths. This is

interesting considering that shallow water waves are also more prone to plunging type breaking. Comparing the two different methods for determining the impact forces and moments also returns significant results. The use of nonlinear wave celerity and crest elevations results in impact forces which are larger when compared to impact loads calculated with linear quantities. The nonlinear impact forces and moments are also larger for shallower water waves as a result of the increase in the nonlinear quantities of wave celerity, crest elevation, and moment arm.

The investigations into apparent fixity presented cases that significantly increase breaking wave moments. The max moments considering apparent fixity are largest for shallower water depths with larger diameters. This is not particularly surprising considering the formulation of apparent fixity used in the analysis. Furthermore, the effect of the diameter on the max moment when considering apparent fixity is more important for a given water depth than the increase of the force associated with shallower water waves. In summation, the effect of apparent fixity significantly increases the max moments of breaking wave loads. The magnitude of this effect is largely dependent on the water depth and cylinder diameter.

One last general conclusion about the entire analysis process concerns the presentation of results. The trends present in the different comparisons were not readily apparent in a number of presentation options considered. The final method of utilizing the scatter plots for the presentation of results allowed for conclusions to be drawn across the full range of design variables investigated. Information concerning the nature of the design wave and cylinder diameter is apparent across the full range of design

variables. Moreover, additional layers of information can be applied to the scatter points which show important trends in results as diverse as max force ratios, dimensional moments, and the time length of impact forces. Furthermore, the choice of axes in these scatter plots fundamentally changes how information is conveyed. Some axes make trends present in shallow and intermediate water waves readily apparent. Other axes are more useful when comparing the applicability of the different wave force methods. The choice of axes in this analysis in no way represents all the options available. This analysis presents a good example of the possibilities for comparison this approach provides.

REFERENCES

Battjes, J.A., 1974. Surf Similarity, 14th International Conference on Coastal Engineering. ASCE, Copenhagen, Denmark, pp. 1050-1061.

Burton, T., 2011. Wind energy handbook, 2nd ed. Wiley, New York.

Chakrabarti, S.K., 1987. Hydrodynamics of offshore structures. Computational Mechanics.Springer Verlag, New York.

Chakrabarti, S.K., 2005. Handbook of offshore engineering. Elsevier, London.

De Vries, W.E., Krolis, V.D., 2007. Effects of Deep Water on Monopile Support Structures for Offshore Wind Tubines, European Wind Energy Conference. European Wind Energy Conference, Milan, Italy.

Dean, R.G., 1965. Stream Function Representation of Nonlinear Ocean Waves. Journal of Geophysical Research 70 (18), 4561-4572.

Dean, R.G., Dalrymple, R.A., 1991. Water wave mechanics for engineers and scientists. World Scientific, Teaneck, NJ.

Dean, R.G., University of Florida. Coastal and Oceanographic Engineering Laboratory, 1974. Evaluation and development of water wave theories for engineering application. U.S. Coastal Engineering Research Center, Fort Belvoir, Va.

The European Wind Energy Association (EWEA), 2011. Wind in our Sails: The coming of Europe's offshore wind energy industry.

The European Wind Energy Association (EWEA), 2012. The European offshore wind industry key 2011 trends and statistics.

Faltinsen, O.M., Newman, J.N., Vinje, T., 1995. Nonlinear-Wave Loads on a Slender Vertical Cylinder. Journal of Fluid Mechanics 289, 179-198.

Goda, Y., Haranaka, S., Kitahata, M., 1966. Study on impulsive breaking wave forces on piles, Report Port and Harbour Technical Research Institute 6 (5), pp. 1-30 (in Japanese).

Hallam, M.G., Heaf, N.J., Wootton, L.R., Atkins Research and Development., 1978. Dynamics of marine structures: methods of calculating the dynamic response of fixed structures subject to wave and current action, 2d ed. CIRIA Underwater Engineering Group, London.

International Electrotechnical Commission, 2009. Wind turbines- Part 3: Design requirements for offshore wind turbines (IEC 61400-3:2009), Geneva, Switzerland.

Kaiser, M.J., Snyder, B.F., 2012. Offshore wind energy cost modeling : installation and decommissioning. Springer, New York.

Klepsvik, J., 1995. Nonlinear Wave Loads on Offshore Structures. M.S. Thesis. Massachusetts Institute of Technology, Department of Ocean Engineering.

Lemos, C.M., 1992. Wave breaking : a numerical study. Springer-Verlag, New York.

LORC, List of Offshore Wind Farms. http://www.lorc.dk/offshore-wind-farms-map/list.

Miche, R., 1951. Le Pourvoir Reflechissant des Ouvrages Maritime Exposes a L'action de La Houle. Annale Ponts et Chaussees, 121 Annee, 285-319.

Morison, J.R., Obrien, M.P., Johnson, J.W., Schaaf, S.A., 1950. The Force Exerted by Surface Waves on Piles. Transactions of the American Institute of Mining and Metallurgical Engineers 189, 149-154.

Musial, W.D., Ram, B., National Renewable Energy Laboratory (U.S.), Energetics Inc., 2010. Large-scale offshore wind power in the United States assessment of opportunities and barriers, Nrel/Tp 500-40745. National Renewable Energy Laboratory, Golden, CO, p. 221.

National Research Council (U.S.) Committee on Offshore Wind Energy Turbine Structural and Operating Safety, 2011. Structural integrity of offshore wind turbines: oversight of design, fabrication, and installation. Transportation Research Board, Washington, D.C.

Offshore Wind Cost Reduction: Pathways Study, 2012. The Crown Estate, London.

Sarpkaya, T., Isaacson, M., 1981. Mechanics of wave forces on offshore structures. Van Nostrand Reinhold Co., New York.

Tempel, J.V.d., 2006. Design of Support Structures for Offshore Wind Turbines. Delft University of Technology, p. 209.

United States Army Corps of Engineers, Coastal Engineering Research Center (U.S.), 1984. Shore protection manual, 4th ed. Dept. of the Army, Waterways Experiment Station, Corps of Engineer. Vicksburg, MS.

Weggel, J.R., 1972. Maximum Breaker Height. Journal of the Waterways, Harbors and Coastal Engineering Division, ASCE, 98 (No. WW4).

Wienke, J., Oumeraci, H., 2005. Breaking wave impact force on a vertical and inclined slender pile - theoretical and large-scale model investigations. Coastal Engineering 52 (5), 435-462.

APPENDIX A

ADDITIONAL FIGURES

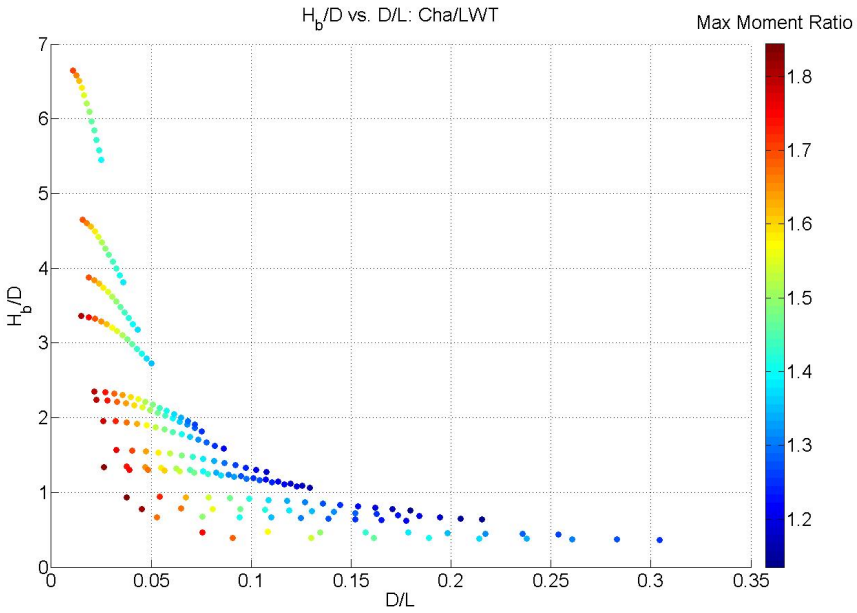

Figure A1 Max Moment Ratio Scatter Plot (D/L): Cha/LWT

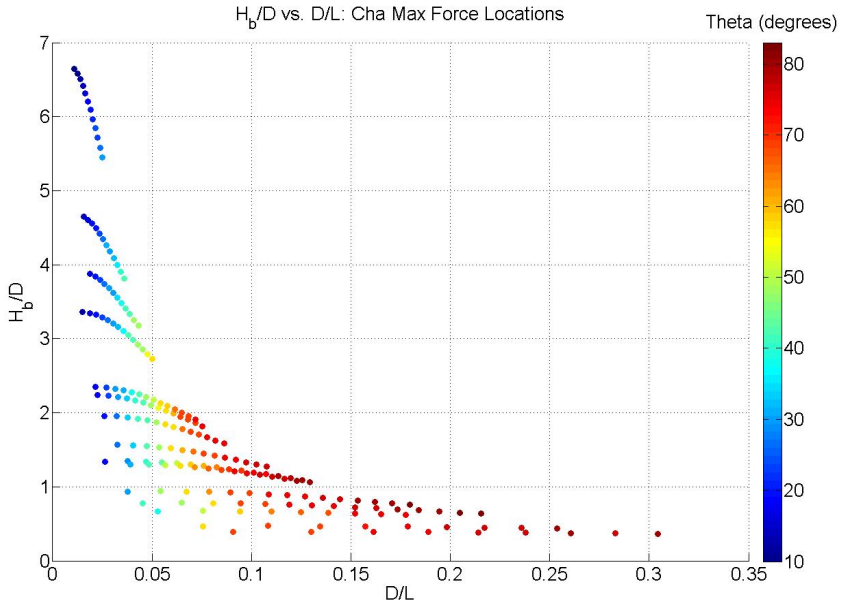

Figure A2 Max Force Location: Chakrabarti

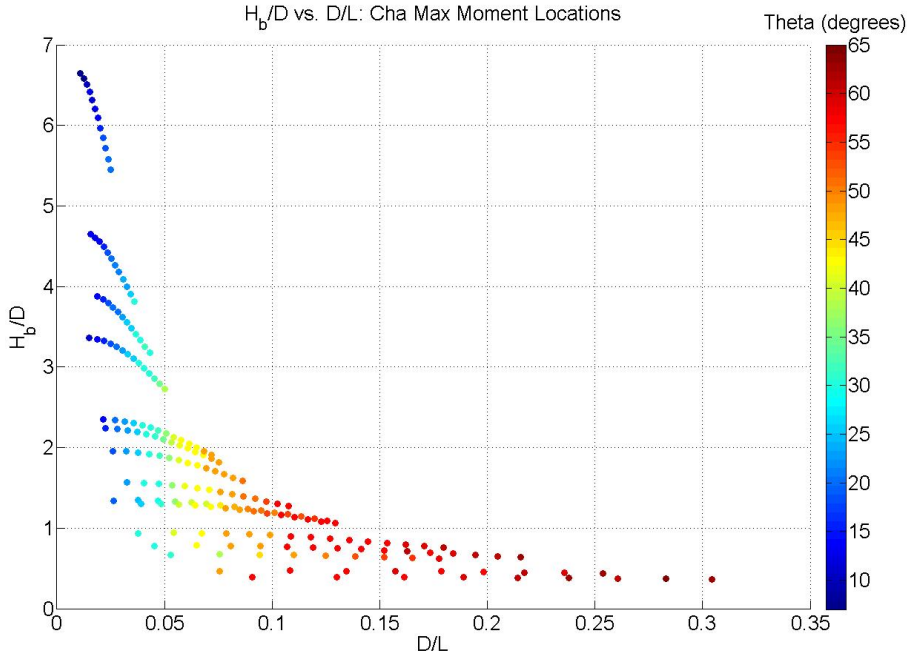

Figure A3 Max Moment Location: Chakrabarti

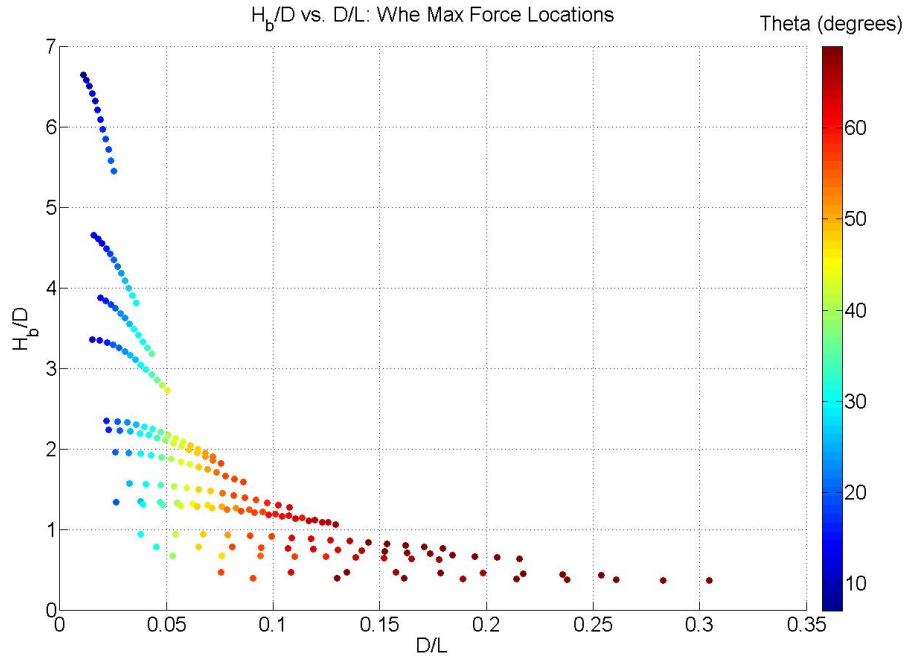

Figure A4 Max Force Location: Wheeler

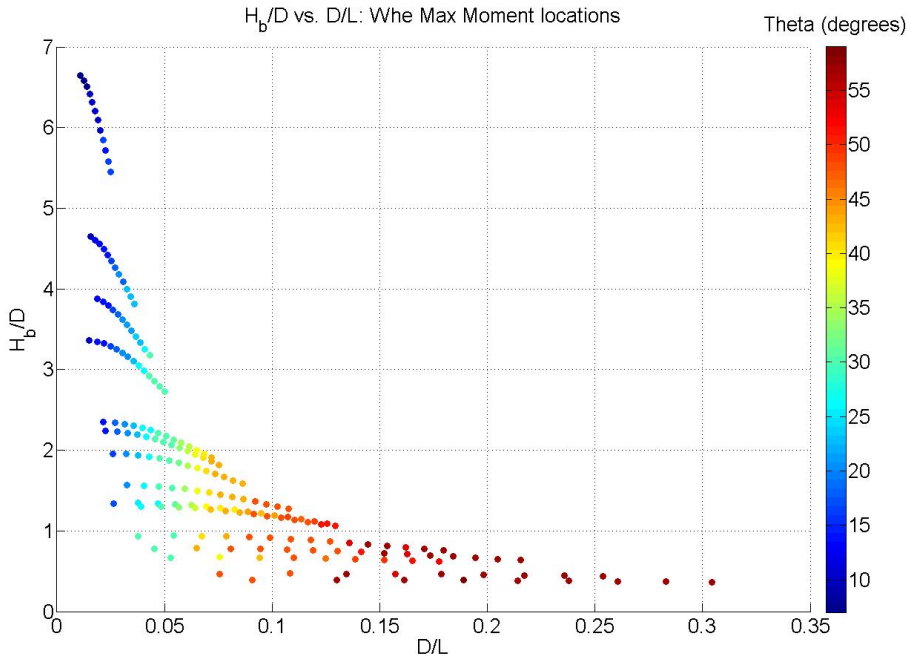

Figure A5 Max Moment Location: Wheeler

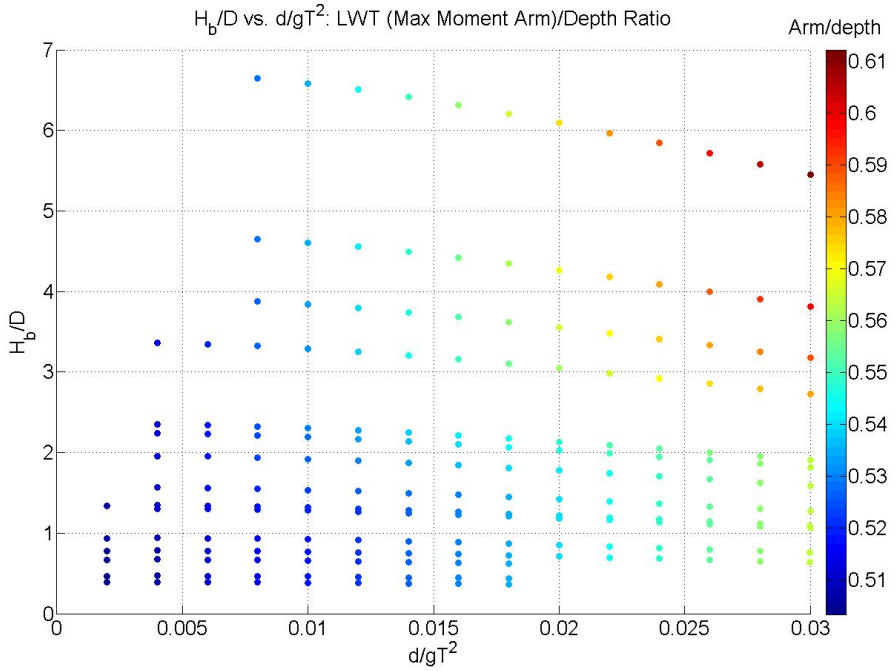

Figure A6 Moment Arm/Depth Ratio Scatter Plot: LWT

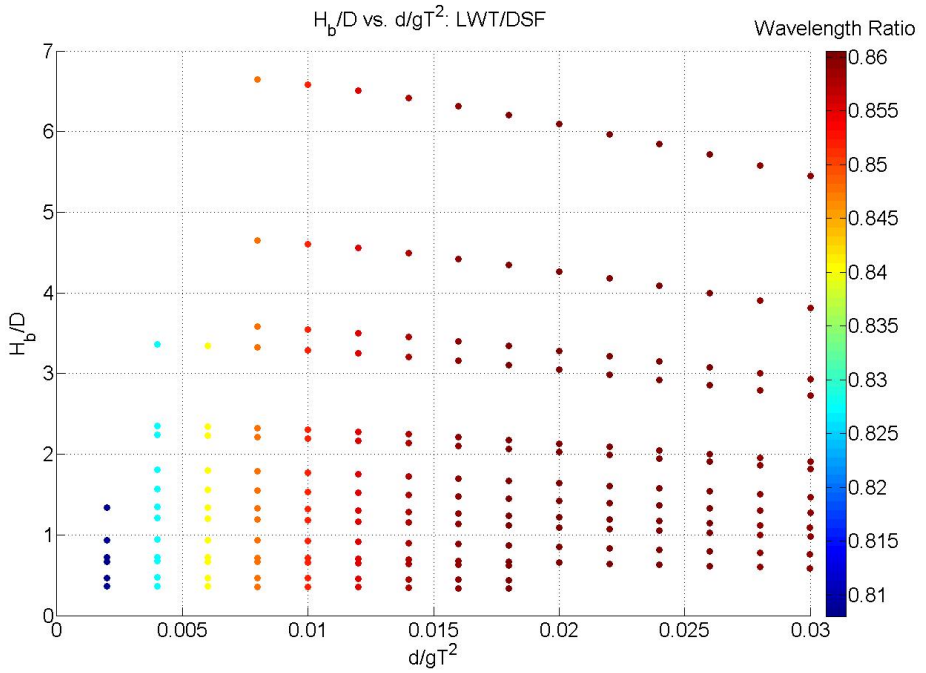

Figure A7 Wavelength Ratio Scatter Plot: LWT/DSF

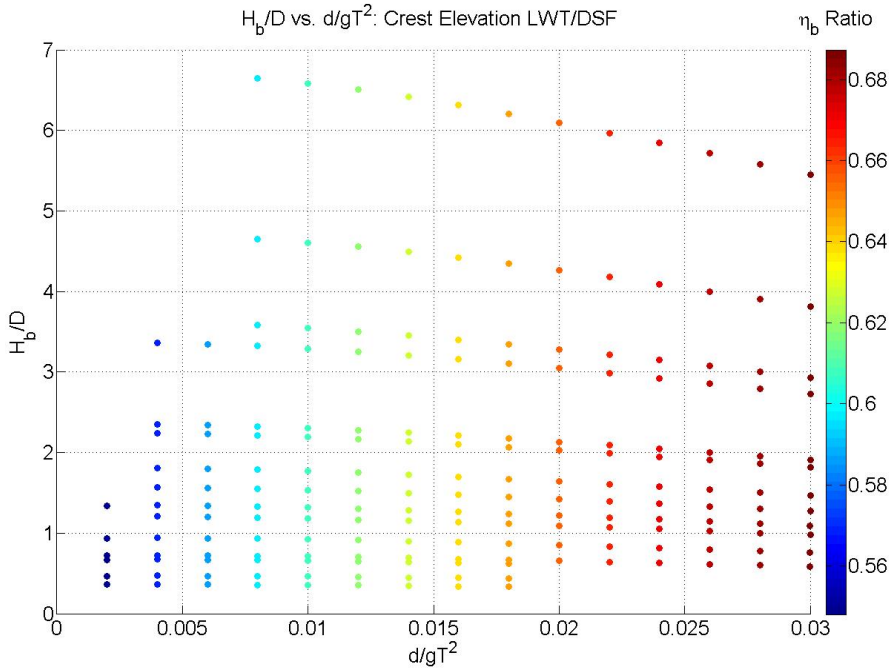

Figure A8 Crest Elevation Ratio Scatter Plot: LWT/DSF